

Micromachining of thin films and surfaces of metals and polymers using excimer laser

A Thesis Submitted

in Partial Fulfillment of the Requirements

for the Degree of

Doctor of Philosophy

by

Syed Nadeem Akhtar



to the

**DEPARTMENT OF MECHANICAL ENGINEERING
INDIAN INSTITUTE OF TECHNOLOGY KANPUR, KANPUR**

MARCH, 2015

Statement

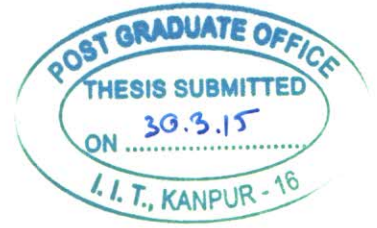
I, hereby, declare that the matter reported in this thesis, titled “**Micromachining of thin films and surfaces of metals and polymers using excimer laser,**” is the result of the research carried out by me in the Department of Mechanical Engineering, at Indian Institute of Technology Kanpur, Kanpur, India, under the supervision of Dr. J. Ramkumar and Prof. S. Anantha Ramakrishna.

In keeping with the general practice of reporting scientific observations, due acknowledgement has been made, wherever the work described is based on the findings of other investigators.

IIT Kanpur
March, 2015

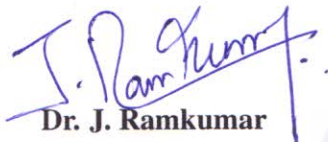


Nadeem
Syed Nadeem Akhtar
Research scholar
Roll no. : 10205066



Certificate

This is to certify that the work under the thesis titled “**Micromachining of thin films and surfaces of metals and polymers using excimer laser**” by **Syed Nadeem Akhtar** is an original work carried out under our supervision and this work has not been submitted elsewhere for the award of a degree.


Dr. J. Ramkumar

Associate Professor
Department of Mechanical Engineering
Indian Institute of Technology Kanpur
Kanpur-208016, India


Dr. S. Anantha Ramakrishna

Professor
Department of Physics
Indian Institute of Technology Kanpur
Kanpur-208016, India

Synopsis

Name of the student : Syed Nadeem Akhtar
Roll No. : 10205066
Department : Mechanical Engineering
Thesis title : Micromachining of thin films and surfaces of metals and polymers using excimer laser
Name of the thesis supervisors : Dr. J. Ramkumar
Dr. S. Anantha Ramakrishna
Month and year of submission : March, 2015

Laser machining at the micrometer domain has extensive applications in device fabrication technologies, where it can be used to machine, for example, channels and reservoirs in polymeric materials for use in micro-fluidic devices, or to machine circuit elements on metal films for fabrication of miniaturized integrated circuits.

This work concerns with experimental and numerical studies on micropatterning of thin films and surfaces of metals and polymers, using excimer laser machining via mask projection techniques. Various features such as channels and holes have been machined on the surface of bulk polymers and metals. The ablation rates of these materials have been determined at various length scales with varying incident laser intensity, which is further used to machine continuous complicated structures for device applications. The machining is also simulated numerically, initially considering mainly the thermal aspects of the material removal process. The modeled results show that the ablation in metals is predominantly pyrolytic (thermal) whereas that in polymers is photolytic (photo-decomposition followed by ejection of fragments). To model the photolytic ablation in polymers, a numerical model is adapted to incorporate effects such as plasma plume absorption, reflection and scattering losses. The modeled results show good agreement with experimental observations.

Chapter 1 presents an introduction to lasers, laser machining and prominent mechanisms of laser ablation. Principle of excimer laser generation and the basic parameters of lasers that play a significant role in the ablation process are mentioned. The effects of wavelength of radiation and the pulsed nature in the machining processes are brought to the fore. The characteristics of the laser-material interaction are described by considering the mechanisms and time-scale of photon absorption in matter. The chapter reviews the issue of the relative dominance of the two mechanisms of laser ablation - pyrolytic and photolytic - in metals and polymers. It is brought out that both mechanisms are active in case of polymers, albeit to different degrees, determined by the properties of radiation and the material. A detailed review of the nature of ablation, plasma plume formation and its interaction with the incoming radiation and concepts of ablation rate and threshold is provided.

The chapter draws to a close with brief references to the works carried out by researchers relating to laser micromachining of metals, polymers and metal films. Although machining metals has long been a forte of continuous and microsecond pulsed lasers, the literature discussed here includes use of nanosecond UV lasers for machining metals. The effect of ambient atmosphere (assist gases) on machining with long pulse lasers has been reviewed. Concerning polymers, fabrication of micro features by researchers has been discussed. The features comprise high aspect ratio holes and channels with varying cross sections, besides others. Measurements of ablation rates and thresholds have been reviewed. The effect of ambient atmosphere has been mentioned with reference to machining of polymers too. Machining of thin metal films has been reviewed in detail, with emphasis on the mechanism of ablation. The ablation mechanism in this case is contrasted with that in the case of surface machining of bulk metals. The properties of the coating material are involved to further the understanding of this mechanism. The review of thin film machining is followed by a brief discussion of the novel technique, employed in the course of the thesis, of machining metal films after coating those with a sacrificial layer of a polymer. In the thesis, investigations on

the applications of excimer laser as a tool that can substitute other conventional techniques of, for example, patterning metal films and fabricating micro lens arrays, have been performed. The chapter concludes with a brief review of the applicability of micro-lens arrays and their fabrication techniques.

Chapter 2 provides information regarding the experimental setups used and procedures employed for conducting the experiments. The excimer laser machine is described in detail with its specifications. The modes of operation of the machine are briefly described. The laser micromachining setup is explained, with emphasis on beam shaping and homogenization. The mask projection technique is explained in detail, along with a discussion on basic optics. The techniques of mask manufacture utilized in this work are briefly described. Characterization techniques comprising microscopy, three dimensional profilometry and image acquisition and processing techniques are described. The chapter ends by detailing the procedures adopted for machining metal surfaces, polymers and metal thin films, mentioning, along the way, the input parameters used. The sources of errors and their treatment are discussed in the last section.

Chapter 3 provides discussions on micromachining of metal surfaces under the influence of ambient gas. A thermal ablation model (pyrolytic) is built to predict the depths of ablation during laser micromachining of stainless steel. The two-dimensional model considers the laser beam as a surface heat source, based on the fact that the optical skin depth in case of metals is of the order of tens of nanometers. The thermal conductivity is considered to vary with temperature. Analysis of micro-channels and holes, with characteristic dimensions of 100 μm , machined on steel under varying machining conditions, is provided. The shape of the channels and holes, the profile of the bottom surface and the formation of ridges on the edges are discussed in detail. The features are analyzed by studying their scanning electron micrographs and three dimensional optical profiles. The depths of ablation obtained from experiments and from numerical simulations are compared. The variation of ablation

efficiency of pulses with variations in pulse energy is discussed. A brief analysis of the surface roughness of the bottom of the channels is provided. The machined holes are studied on similar lines, while highlighting the reasons for difference in the depths of ablation in the latter case.

Chapter 4 provides results and discussion on micromachining of polymers. 100 μm , wide channels are machined on Kapton (polyimide), PMMA and boPET. The experiments are carried out under three different atmospheres. A dynamic photolytic ablation model is presented that considers the effects of plasma shielding. The model relies on inherent material properties to predict the depth of ablation. The simulated ablation curves are obtained for fluences ranging from 0.1 to 6 J/cm^2 . The experimental ablation curves are found to be much lower than the simulated curves when plasma shielding is not considered. Good agreement between the two are observed upon considering plasma shielding. By fitting the simulated curves to the experimental ones, ablation threshold and plasma shielding parameters are obtained for the polymers. An anomalous behavior of Kapton has been discussed based on the observation that the depth of ablation at the highest fluence considered (5 J/cm^2) was lower than that observed at the lower value of fluence. This has been explained based on swelling of Kapton upon irradiation. The concept of incubation pulses has been introduced in the case of PMMA, and it has been argued as to why incubation pulses are not required in the cases of Kapton and boPET. Higher depths of ablation observed in the case of PMMA are compared to those in the cases of Kapton and boPET, and the observation is discussed while considering the optical properties of the materials. Although the ablation behavior of boPET is similar to that of Kapton, it does not show the anomalous behavior of Kapton at high fluence. It is understood that boPET, unlike Kapton, does not release significant amount of gases, if any, upon irradiation with excimer laser.

Laser machining can be used to fabricate integrated circuits by ablation of metallic films. It is then imperative to understand how the microfeature quality, and most importantly the

microfeature edge quality, responds to changes in machining parameters. A comprehensive study on laser micromachining of thin metals films is presented in Chapter 5. $100\ \mu\text{m}$ wide straight and oblique channels have been machined on $200\ \text{nm}$ thick films of aluminum and chromium, deposited on borosilicate glass. The features are machined on the films using a square shaped binary mask, that generates a $100\ \mu\text{m} \times 100\ \mu\text{m}$ wide square spot on the workpiece. The micromachining is carried out under varying machining parameters determined by a design of experiments, and the machined features are characterized for their edge quality, including dimensional accuracy. Metal films have been observed to ablate at fluences much lower than the ablation threshold, and often before the onset of melting. The dependences of edge roughness, channel width and boundary integrity on the machining parameters have been studied. Better feature quality has been observed while machining chromium compared to aluminum, an observation primarily attributed to the strong adhesion of chromium films to the glass substrate.

A novel method is developed that allows fine machining of features even in films of metals that have low adherence to glass. Widely used techniques for patterning metal films are discussed, and the advantages of using the technique of laser machining metal films post polymer coating are drawn out. The microfeatures obtained upon laser machining metal films with and without polymer coating is compared for the feature quality, and a detailed discussion on the action of polymer coating is presented. The feature quality obtained after machining polymer coated metal films shows considerable improvement. The observations for oblique channels, machined with a square laser spot, are contrary to those for straight channels. However, polymer coated metal films have been observed to undergo a close to ideal ablation, little affected by fluence.

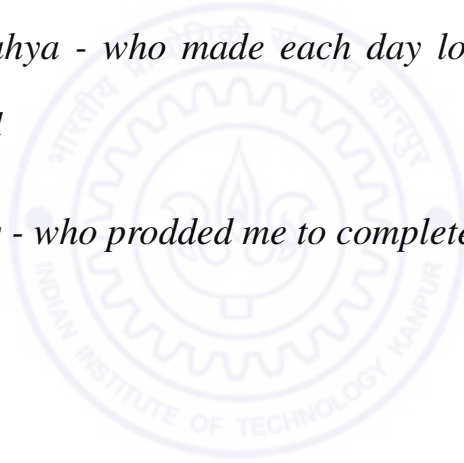
Chapter 6 presents discussions on fabrication of micro lens arrays and test patterns of miniaturized circuits. Arrays of microlenses with $160\ \mu\text{m}$ diameter have been fabricated on PMMA. The binary mask has been fabricated in-house in two steps, and has a varying

opening across its cross section. The ablation rate of PMMA is measured and ideal profiles of ablation have been calculated corresponding to the design of the binary mask. These profiles are compared to the experimental profiles of the lenses and good agreement between the two have been observed. The chapter concludes with a discussion on the development of accessories to aid in excimer laser micromachining using the mask projection technique.



This thesis is dedicated to

- *My parents - who bore to let me stay away from them during the time when they needed me,*
- *My wife - who stood by me and is a source of constant support,*
- *My son, Yahya - who made each day look bright, even if it actually wasn't, and*
- *My siblings - who prodded me to complete my work at the earliest.*



Acknowledgments

I begin with extreme gratitude to the Almighty God, for having given me the ability to read and learn, and the opportunity to study from some of the best teachers. Teachers leave an indelible mark on the persona of the scholar, and such has been in my case too. The commitment, interest and care, with which my supervisors guided me, have enabled me to sustain the spirit of enquiry through the last few years. This thesis is a fruit of that enquiry, and I express my gratitude to my supervisors, Dr. J. Ramkumar and Dr. S. Anantha Ramakrishna.

My parents have wanted me to be with them throughout. It has been over twelve years, that I have not had the opportunity to stay with them. Yet, the readiness with which they accepted my stay, away from them, and the moral support and kind wishes they sent to me, allowed me to have the state of mind necessary to concentrate on the path ahead. I thank my mother and father, for this and for everything else they have done for me, since I was born.

I had looked for support from my wife of three years, when I started working on my doctoral thesis. She surpassed all expectations of support, and relieved me of my responsibilities towards my family, including my children, so that I may devote my time and efforts, whole heartedly, towards the doctoral thesis. The fact, that she herself is working on her doctoral thesis, did not deter her from giving priority to me, and my work. I am putting the final touches to my dissertation, while she still toils on her dissertation. Merely thanking her here will not do justice to her sacrifices.

Research in any field of science or art requires sustained efforts. There are often occasions when success eludes us, and when mental and physical fatigue tires us. It was at those moments that the sight of my son brightened up the days for me. It has been an unparalleled joy, meeting him at the end of the day, everyday. Such moments reinvigorated the mind and the body, and allowed me to strive, regardless of the disappointments.

My stay in the Indian Institute of Technology Kanpur, which is also my alma mater, has been made beautiful and enjoyable by my friends. I thank them, in no particular order, for being with and around me, through the last few years. Thank you Dr. Kanmani Subbu, for playing the role of the elder brother. Thank you Dr. Satish Chinchankar, for the useful discussions on the many facets of life. Thank you Dr. Govind Dayal, for aiding my initiation into the field of laser micromachining. Thank you Mr. Javed Asghar, for passing on to me some of your liveliness and energy. Thank you Mr. C. B. Singh, for the fun moments. Thank you Mr. Deepak Sachan, for being around and for also being a long time friend. Thank you Mrs. Priyanka Sachan, for teaching me fine English, for the complimentary SEMs, and for the company we shared over many dinners. Thank you Ms. Ranjana Kumari, for the time and efforts you put into characterizing many of the features fabricated by me. Thank you Mr. Shashank Sharma, for your help with the numerical simulations, and for the many experiments that we conducted together. Thank you Mr. Kartar Singh, for being a true friend, for being at my beck and call, and for the hundred odd dinners that I had at your expense. Thank you Mr. Yashwant Kumar, for your timely smiles and untimely laughs. I specially thank my schoolmate, Mr. Shabab Alam, for hosting me, no-holds-barred, during one of my trips abroad. We all need a friend like you, Shabab.

Thank you Dr. Ashutosh Sharma, Dr. Utpal Das and Dr. R. Vijaya, for allowing me access to the characterization equipments in your labs. Thank you Mr. Phoolchand, Mr. Shailendra, Mr. Arun and Mr. Sushil Yadav, for your kind helps, time and again. I specially thank Mr. Mohammad Mohsin, for being my local guardian in the campus. Thank you Dr. Abdullah bin Abu Bakar, Dr. Saiful Islam, Mr. Mohammad Shariq and Mr. Amit Mujal, for the nice times our families had together. There are many more persons who helped me, in many more ways, and whose names elude me at this moment of time. To all those, gratitude.

Syed Nadeem Akhtar

Contents

Statement	iii
Certificate	v
Synopsis	vii
Acknowledgments	xv
Contents	xvii
List of Figures	xxiii
List of Tables	xxix
List of Abbreviations	xxxi
1 Introduction to lasers and laser micromachining	1
1.1 Introduction	1
1.2 Parameters of laser radiation	4
1.3 Key terminologies in laser-material interaction	4

1.4	Mechanism of laser ablation of metals	8
1.5	Mechanism of laser ablation of polymers	11
1.5.1	Nature of ablation	12
1.5.2	Plume interaction during the laser pulse	14
1.5.3	Ablation rate and threshold	14
1.6	Survey of laser micromachining of metals	17
1.7	Survey of laser micromachining of polymers	19
1.8	Survey of laser micromachining of metal films	21
1.9	Summary	25
1.10	Objective of the thesis	25
2	Experimental setup, procedures and characterization techniques	27
2.1	The excimer laser machine	28
2.1.1	Modes of fixing the energy of the laser pulses	29
2.1.2	Modes of triggering pulses from the laser machine	29
2.2	Laser micromachining setup	30
2.3	Mask projection technique	31
2.4	Methods of mask manufacture	34
2.4.1	Conventional micromachining of metal sheet	35
2.4.2	Micromachining of polymer and metal sheets	35
2.4.3	Physical vapor deposition	35
2.5	Characterization techniques and procedures	35
2.5.1	Microscopy techniques	35

2.5.2	Profilometry techniques	36
2.5.3	Image acquisition, measurement and processing	38
2.6	Experimental procedures	39
2.6.1	Procedure for metal machining	39
2.6.2	Procedure for polymer machining	40
2.6.3	Procedure for metal thin film machining	42
2.6.4	Procedure for machining micro lens arrays	45
2.7	Sources of error in the experiments	46
3	Excimer laser micromachining of metals and influence of ambient gas	49
3.1	Numerical simulations of laser ablation of metals	50
3.1.1	A static thermal ablation model	50
3.1.2	A dynamic thermal ablation model	53
3.1.3	A dynamic thermal ablation model with fluid flow	54
3.2	Results and discussion	57
3.2.1	Simulations of ablation models	57
3.2.2	Analysis of 100 μm wide channels in SS	60
3.2.3	Analysis of 100 μm diameter holes in SS	74
3.3	Conclusions	78
4	Excimer laser micromachining of polymers, influence of plasma plume absorption and ambient gas	81
4.1	A static thermal ablation model	82
4.2	A dynamic photo-ablation model	83

4.3	Results and discussion	85
4.3.1	Ablation rates	87
4.3.2	Ablative machining of Kapton	89
4.3.3	Ablative machining of PMMA	93
4.3.4	Ablative machining of boPET	96
4.3.5	Discussion on ablation efficiency	97
4.4	Conclusions	99
5	Microfeature edge quality enhancement of metal films by coating with a sacrificial polymer layer	103
5.1	Film heating model and numerical simulations	104
5.2	Results and discussion for straight channels	106
5.2.1	Direct machining of metal film	107
5.2.2	Machining of polymer coated metal films	113
5.3	Results and discussion for oblique channels	120
5.3.1	An ideal oblique microchannel	120
5.3.2	Aluminum film machining (without and with polymer coating) . . .	121
5.3.3	Chromium film machining (without and with polymer coating) . . .	126
5.4	Conclusions	129
6	Fabrication of novel setups and structures	133
6.1	Microlens arrays and their fabrication	134
6.1.1	Fabrication and analysis of masks	135
6.1.2	Analysis of the microlens profiles	137

6.2	Development of a bistable multivibrator	143
6.2.1	Description of the setups and communication protocol	143
6.2.2	Trigger pulse analysis	145
6.2.3	T flip flop	146
6.2.4	Signal conditioning	148
6.2.5	The leading edge triggered bistable multivibrator	149
6.2.6	A working example of the automatic switching of the excimer laser machine	149
6.3	Fabrication of sample circuits for use as MHMICs	152
6.3.1	Fabrication of interdigitated electrodes	153
6.3.2	Fabrication of connecting pads	155
7	Conclusions and scope for future work	157
	References	161
	Appendices	177
	Publications	189



List of Figures

1.1	The schematic of laser generation from excimer gas	3
1.2	The cross sectional micrograph of an ablated crater in PP	13
1.3	Ablation graph of boPET during machining by KrF excimer laser	15
2.1	Schematic diagram of the experimental setup for laser machining	31
2.2	Schematic of a mask projection	32
2.3	Schematic diagrams of a simple optical system	33
2.4	Schematic of a mask projection system	33
2.5	Optical imaging techniques	36
2.6	Optical profilometry images	37
2.7	Examples of images obtained during image processing	38
2.8	The photograph of the mask used for machining channels and holes	40
2.9	The scanning electron micrograph of a set of features machined on SS	41
2.10	Examples of 100 μm wide channels machined on 200 nm aluminum film	43
2.11	The binary mask, machined in acrylic, used in this study	43

3.1	The geometrical domain of the model, with incident radiation and boundary conditions	50
3.2	Temperature dependent properties of the material used in the dynamic thermal ablation model	55
3.3	A schematic diagram of the computational domain	56
3.4	Temperature plots of the domain at various times	58
3.5	Density plots of the domain at various times	59
3.6	Simulation results from a preliminary dynamic thermal ablation model with fluid flow	60
3.7	Simulation results from the dynamic thermal ablation model with fluid flow	61
3.8	Typical results for micro channels machined in stainless steel	62
3.9	The scanning electron micrographs of 100 μm wide channels machined in SS	63
3.10	The 3D and cross-sectional profiles of 100 μm wide channels machined in SS	64
3.11	Comparison of experimental and simulated results from micromachining SS	66
3.12	Surface roughness of channels in SS	69
3.13	The ablation depths of 100 μm wide channels machined in SS	70
3.14	The ablation rates of 100 μm wide channels machined in SS	72
3.15	The plots of widths of 100 μm channels and holes machined in SS as functions of the number of pulses	73
3.16	The scanning electron micrographs of 100 μm dia holes machined in SS	74
3.17	The 3D and cross-sectional profiles of 100 μm diameter holes machined in SS	75
3.18	The ablation depths of 100 μm diameter holes machined in SS as functions of the number of pulses	76
3.19	The ablation rates of 100 μm diameter holes machined in SS as functions of the number of pulses	77

4.1	Typical results for micro channels machined in PMMA	85
4.2	Comparison of experimental and simulated results from micromachining PMMA	86
4.3	Ablation curves for Kapton, PMMA and boPET	88
4.4	Depth plots for Kapton at 3 and 5 J/cm ² (channel width 100μm)	89
4.5	Depth plot for Kapton machined in air (channel width 100μm)	91
4.6	Depth plots for Kapton under helium and oxygen atmospheres	92
4.7	Schematic of swelling observed in Kapton	92
4.8	Number of (incubation) pulses required to initiate ablation in PMMA as a function of fluence, calculated from the dynamic photo-ablation model	93
4.9	Depth plots for PMMA at 3 and 5 J/cm ² (channel width 100μm)	94
4.10	Depth plots for PMMA for 100 and 10μm wide channels machined in normal atmosphere	95
4.11	Depth plot for boPET at 3 J/cm ² (channel width 100μm)	96
4.12	Depth plots for boPET for 100 and 10μm wide channels machined in normal atmosphere	97
4.13	Depth plots vs. total energy deposited	98
5.1	Temperature evolution profiles of metal films	107
5.2	Variations of edge roughness and channel width with fluence	110
5.3	Aluminum film ablation	111
5.4	Chromium film ablation	112
5.5	Optical micrographs of machined channels	113
5.6	PVA coated aluminum film ablation	116

5.7	PVA coated aluminum film ablation	118
5.8	Examples of boundary integrity of channels	118
5.9	Micrographs showing machined channels and effect of pitch	119
5.10	3D surface plot of boundary integrity vs. spot overlap and pitch	119
5.11	Schematic diagrams of oblique microchannels	121
5.12	Plots showing variations of edge roughness and channel width (of 100 μm oblique channels in aluminum)	122
5.13	Contribution of various factors to edge roughness and channel width of oblique channels	123
5.14	Optical micrographs of some 100 μm wide oblique channels	125
5.15	Plot showing variation of edge roughness and channel width (of 100 μm oblique channels on chromium)	127
5.16	Contribution of various factors to edge roughness and channel width of oblique channels	128
5.17	Optical micrographs of some 100 μm wide oblique channels machined in chromium	129
6.1	A schematic flowchart for deciding the mask shape for a desired profile . . .	136
6.2	The optical photographs of the masks used to machine the micro lens arrays	136
6.3	The optical micrographs of the cross-sections of the micro lenses	138
6.4	Ablation rates of PMMA with 248 nm pulsed excimer laser	139
6.5	Schematic of the procedure to calculate the feature size	139
6.6	Theoretical profiles of lenses machined at different scanning speeds	140
6.7	Experimental and theoretical profiles of micro lenses	141
6.8	3D optical profilographs of 5 \times 5 array of micro lenses	142

6.9	A schematic diagram of the laser micromachining setup	144
6.10	TTL protocol	145
6.11	The trigger pulse	146
6.12	T flip flop	147
6.13	The circuit diagram of T flip flop	147
6.14	Stable pulse from the comparator	148
6.15	The circuit diagram of the complete edge triggered bistable multivibrator	149
6.16	Toggling of output from LOW to HIGH	150
6.17	Toggling of output from HIGH to LOW	150
7.1	The mask holder with slots to mount upto 10 masks	185
7.2	The mask plates, ten in number, that hold the masks in the slots.	186
7.3	The bottom support on which the motor rests	187
7.4	The back support for the motor	187
7.5	The base plate, on which the two supports are mounted	188



List of Tables

1.1	Excimer laser specifications	5
1.2	Properties of some common polymers	7
1.3	Bond energies in eV	12
2.1	Specifications of the excimer laser machine COMPex Pro 205	28
2.2	Levels of input parameters varied during micromachining metals	39
2.3	Levels of input parameters varied during micromachining polymers	42
2.4	Levels of input parameters varied during machining straight channels	44
2.5	Levels of input parameters varied during machining tilted channels	44
2.6	Levels of input parameters varied during machining the micro lens array	45
3.1	Material properties used in the thermal ablation model	51
3.2	Material properties used in the dynamic thermal ablation model	54
3.3	Thermal properties of gases	65
4.1	Material properties used in the thermal ablation model	82
4.2	Ablation threshold parameters for various polymers	88

5.1	Thermal and optical properties used in the thermal ablation model	105
5.2	Times taken for rise in the temperature of films	108
5.3	Maximum temperatures reached in the metal films	108
6.1	Voltage domain and time domain parameters of the various pulses	146
6.2	Comparison of the times required to fabricate two 250 μm long channels . .	151



List of Abbreviations

boPET	bi-axially oriented poly(ethylene terephthalate)
CCD	Charge coupled device
FESEM	Field emission scanning electron microscope
HAZ	Heat affected zone
LIGA	Lithographie, Galvanoformung, Abformung
MEMS	Microelectromechanical systems
MHMIC	Miniaturized hybric microwave integrated circuit
PBTMSS	poly(3-butenyltrimethylsilane sulfone)
PC	Polycarbonate
PI	Polyimide
PMMA	Poly(methyl methacrylate)
PP	Polypropylene
PVA	Poly(vinyl alcohol)
RMS	Root mean square
SEM	Scanning electron microscope/microscopy/micrograph
UV	Ultraviolet

Chapter 1

Introduction to lasers and laser micromachining

Nanosecond ultraviolet (UV) lasers (excimer lasers) are being widely used with polymeric and ceramic materials for a variety of micromachining and microlithographic applications. It allows fine removal of material, mostly in a non-thermal manner, and hence, is a tool of choice for micromachining applications. The study of mechanisms leading to excimer laser ablation of materials has long been a subject of interest for researchers. The need for such studies arises for contact-less and accurate machining control and less undesirable effects generated from the heat based material removal processes. The use of nanosecond UV lasers inhibits the heat-effected alterations in the microstructure and mechanical properties of the material (little heat affected zone). This chapter reviews the properties and applications of excimer lasers and the mechanisms observed and proposed by researchers for nanosecond UV laser micromachining of metals and polymers.

1.1 Introduction

Laser machining has gained popularity because of its applicability with all kinds of materials with little constraint on material properties. Machining depth control at the lengthscale of

ten nanometers is possible with ultraviolet and ultrafast lasers. Lasers have a high energy directionality which allows directional machining, contrary to what is offered by other wet processing techniques.

Laser is an almost monochromatic and collimated electromagnetic radiation that is finding use in clean room fabrication and machine shops, apart from use in diagnostic and spectroscopic techniques. Excimer laser was invented by Basov et al. (1970) in 1970, when they passed a high energy electron beam through liquid Xenon, ten years after the invention of the first laser by Theodore Maiman in 1960. The first commercial excimer laser was developed by Lambda Physik in 1977 [Basting et al. (2002)]. Since then, excimer laser technology has rapidly developed, overtaking the developments in many other laser technologies. This has led to their widespread use in microfabrication and microtreatment industries.

Excimer lasers are a type of gas lasers that operate mainly in the ultraviolet range of wavelength. The word excimer derives from excited dimer, and is generated from a mixture of two gases, generally a rare gas and a halogen gas. The laser is generated when a high intensity discharge ionizes the mixture, which relaxes to form excited molecules of the two gases. The oppositely charged ions combine to form a dimer (or a complex) in an excited state, as the dimer has an unstable ground state. Thus a population inversion is readily achieved resulting in a high gain system. The excited dimers are de-excited through stimulated emission, resulting in a build-up of radiation in the cavity to give rise to laser radiation. This process is schematically shown in Fig. 1.1. The high current discharge can be maintained only for a short duration in the high gain system, resulting in short laser pulses that last for tens of nanoseconds.

The excimer lasers offer many advantages that have led to their deployment in various industries. The UV wavelength is strongly absorbed by biological tissues, such as the eyes, bones and teeth. This has furthered the use of excimer lasers in many ophthalmic, dental and dermatological surgical applications [Blum et al. (1988); Linsker et al. (1984)]. The energy contained in the UV radiation is enough to chemically alter, or generally break, the chemical bonds in polymers and ceramics. This, coupled with the strong absorption of the UV radiation by the same materials, grants the ability to selectively ablate very thin layers of

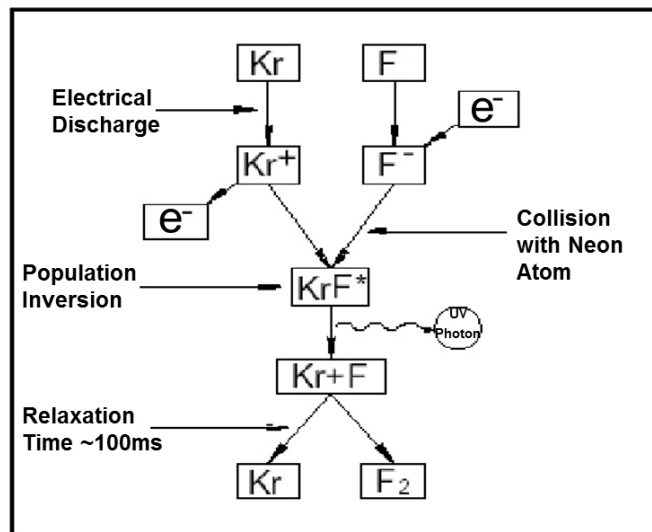


Figure 1.1: The schematic of laser generation from excimer gas [from www.resonetics.com]

materials. The excimer lasers have, hence, become the popular tool of choice for micromachining such materials [Srinivasan and Mayne-Banton (1982); Klotzbach et al. (2011)]. The UV wavelength allows the lasers to be focussed to micrometer sized spots, thereby allowing their use in microlithographic applications [Jain et al. (1982); Polasko et al. (1984)]. This has played a critical role in the use of excimer lasers in the development of microelectronic devices. Surface cleaning and adjustment of micro-assemblies are some non-conventional uses of excimer lasers [Meijer (2004)].

The wide presence of excimer lasers encouraged their use in understanding of the laser material interaction. Researchers had begun to investigate the mechanism of laser ablation in the early 1960s with tools like high speed photography. Ready (1965), for example, had put in efforts to study, both experimentally and analytically, the laser ablation using classical heat transfer and thermodynamic principles. The observations started out with basic measurements of depth of ablation and understanding its correspondence with analytically calculated data. Since then, the study of laser ablation mechanisms with various materials has progressed to the extent that advanced techniques like time-resolved spectroscopy and molecular dynamics simulations are able to observe and predict the escape velocity of

ablated fragments, their composition and time duration of ablation [Dijkkamp et al. (1987); Srinivasan et al. (1986, 1995)].

This chapter reviews the observations and findings relating to the mechanism of ablation of metals and polymers when irradiated by high fluence nanosecond UV lasers, such as excimer lasers. The chapter first introduces the basic parameters of lasers that play a significant role in the ablation process. Definition of key terminologies related to the process and properties of materials are then discussed. This is followed by a discussion on mechanisms active during the excimer laser ablation of metals and polymers, and the various pathways and products as a result of this ablation.

1.2 Parameters of laser radiation

Laser radiation is characterized by certain key parameters. Concerning lasers used in machining of materials, the relevant parameters are the wavelength of radiation, the nature of radiation (continuous or pulsed), the duration of the pulse and the quality of the beam. Wavelength (λ) determines the energy carried by individual photons in the laser beam and hence the kind of physical and chemical interactions these photons will have with the material. Large wavelength lasers, like CO₂ ($\lambda = 10.6\mu m$) lasers, mainly cause ablation by a thermal process because the photons do not carry enough energy to cause any other effect. Short wavelength lasers, like F₂ lasers ($\lambda = 157nm$), mainly cause ablation by a photolytic process wherein the photons are directly involved in breaking the chemical bonds within the material. A description of the various types of excimer lasers, their wavelengths and photon energies is given in Table 1.1.

1.3 Key terminologies in laser-material interaction

When a laser radiation is incident on a material most of the photons get absorbed by the electrons present in the outermost shell of the atoms in the upper layers of the material (called

Table 1.1: Excimer laser specifications [Meijer (2004)]

Laser	Wavelength (<i>nm</i>)	Photon energy (<i>eV</i>)
XeF	351	3.53
XeCl	308	4.03
KrF	248	5.00
KrCl	222	5.50
ArF	193	6.42
F ₂	157	7.43

the skin layer). The thickness of the skin layer, also called the optical penetration depth (δ), is $2/\alpha$, where α is the absorption coefficient of the material for the particular wavelength. A higher absorption coefficient implies smaller skin depth, which means that the incident radiation is absorbed in a thinner region under the surface being irradiated, leading to higher surface temperatures [Bulgakova and Bulgakov (2001)]. The optical penetration depth for polymers is about 200 nm, and that for a metal is of the order of 10 nm.

The pathways for photon absorption and subsequent scattering of its energy into different modes is well explained by the Jablonski diagram for the material under discussion. The Jablonski diagram is named after the Polish scientist Alexander Jablonski, and it illustrates, vertically, the various energy states of a molecule, and the types of transitions (radiative and non-radiative) between those states. While a radiative transition (to a lower energy state) leads to an emission of a photon, non-radiative transitions comprise vibrational relaxation, internal conversion and inter-system crossing.

When photons are incident on the surface of a material, they couple with electrons, specially in the valence band of the molecule. The electrons, as a result, get excited from their

ground state to an excited state. The time it takes for the photons to get absorbed is called the photon absorption time (t_a), and is of the order of 1 fs. It should be noted that not all electrons transition to the same excited state. The electron transition happens to both the electronic and vibrational excited states, depending on the Boltzmann distribution of the electrons in the ground state.

One of the most common ways of electron relaxation is through vibrational relaxation. The energy of the excited electron is transferred to a vibrational mode of the molecule, as its kinetic energy. This manifests itself in terms of rise in temperature of the material. During the relaxation between vibrational levels, the electronic energy levels do not change, unless the vibrational states overlap strongly with the electronic energy states, in which case the process is called internal conversion. The time it takes for the excited electrons to relax is called the electron relaxation time (or electron cooling time, t_e) and ranges from 10 fs to 10 ps. Vibrational relaxation and internal conversion are almost always present as relaxation pathways, but are mostly not the final transitions.

Another mode of energy dissipation is via radiative transition (photon emission) of the electrons from a higher electronic state to a lower electronic state. This process is called fluorescence and occurs in the time range of 1 ns to 100 ns after the start of the irradiation. Inter-system crossing sometimes leads to fluorescence or phosphorescence.

After about 1 ps of irradiation, the electrons relax and pass on the energy to the lattice in the form of heat. This heat diffuses into the material at the rate determined by the thermal diffusivity (k) and thermal conductivity (κ) of the material [Choudhary (2012); Meijer (2004); Meijer et al. (2002)]. The depth through which the heat diffuses into the material in a certain time ' t ' is called the thermal diffusion depth (d) and is given by

$$d = \sqrt{4kt}. \quad (1.1)$$

The pulse duration is a property of the laser radiation. However, the pulses are classified as short or ultrashort based on whether the optical penetration depth is more or less than the thermal diffusion depth (in time ' t_e '), respectively. Generally speaking, pulses with duration less than 1 ps are called ultrashort pulses.

Table 1.2: Properties of polycarbonate (PC), polypropylene (PP), polyimide (PI), poly(methyl methacrylate) (PMMA) and bi-axially oriented poly(ethylene terephthalate) (boPET) [from Meijer (2004); Brown and Marco (1958); Jensen (2004); Morikawa and Hashimoto (2009); Tsutsumi and Kiyotsukuri (1988); Tokunaga et al. (2010)]. The linear absorption coefficient (α), thermal diffusivity (k), optical skin depth (δ) and thermal diffusion depth (d) are mentioned.

Polymer	α (μm^{-1}) at 248 nm	k (m^2/s)	δ (μm)	d (μm)
PC	1	0.144×10^{-6}	2.0	0.1
PP	-	0.096×10^{-6}	-	0.1
PI	22	0.122×10^{-6}	0.1	0.1
PMMA	0.0063	0.115×10^{-6}	317.5	0.1
boPET	16	0.110×10^{-6}	0.13	0.1

An often used term in laser machining is ‘fluence’. Fluence is defined as the irradiated energy per pulse per unit area of the material, and its units are J/cm^2 . Ablation is noticeable only above a certain value of fluence (depending on the material) and this value is called the threshold fluence (F_{th}). Researchers have, over time, realized that instead of fluence (that makes no reference to the time in which the energy is delivered), intensity better describes the effect of radiation [Jensen (2004); Srinivasan et al. (1995)]. Intensity, then, is defined as average power per pulse per unit area and its units are W/cm^2 . Several parameters affect the mechanism and extent of laser ablation in polymers, and some of those are mentioned in Table 1.2 for some common polymers.

1.4 Mechanism of laser ablation of metals

A comprehensive understanding of laser-matter interaction in metals and energy dissipation pathways for different time and length scales is yet to be developed. After an incident photon has been absorbed, the hot electrons cool down through a series of scattering modes [Von Allmen and Blatter (1995)]. When the incident radiation is below the threshold for dielectric breakdown (and plasma formation, $\sim 10^{13}$ W/cm² [Lorazo et al. (2003)]), the material is pushed into a metastable state due to sudden heating. At low fluences, and for pulses with durations greater than 100 ns, vaporization has been stated to be observed [Kelly and Miotello (1999)]. The recoil pressure due to the expanding vapor is responsible for the melt ejection (material removal) in this case. The action of recoil pressure leaves behind a surface with poor quality. It is important to note that melting, and redistribution of melt towards the boundaries of the irradiated region has been observed even in femtosecond laser irradiation of metals [Zhigilei et al. (2009)].

The discussion of laser ablation mechanisms in metals requires an understanding of some thermodynamic concepts and processes, like the binode, thermodynamic critical point, spallation and phase explosion. The binode (or the binodal curve) is the region where two phases coexist in a thermodynamically stable manner. The binode originates from the triple point (for pure materials) and ends at the critical point (T_c). The thermodynamic critical point is the extremum of the binode. It represents the maximum pressure and temperature at which two phases can coexist. A slight decrease in pressure or increase in temperature causes the phases to merge into each other and the phase boundaries to disappear. If the system is allowed to cool (relax) from the critical point, it follows the binode.

Spallation is the transition of a material into a solid-gas phase due to strong pressure tensile waves [Perez and Lewis (2003)]. Sudden heating of a material, by a laser pulse of high fluence and short duration causes stress confinement, leading to generation of compressive stresses. Also called photomechanical ablation [Zhigilei et al. (2009)], spallation is caused by the release of compressive stresses. Spallation causes the material to fracture and break into fragments of solids or liquid droplets. For spallation to occur, both the laser pulse

duration and the electron cooling time have to be shorter than the characteristic time for thermal expansion. Under such conditions, the material gets heated by the laser pulse almost isochorically, thereby causing stress confinement.

Phase explosion, also known as explosive boiling, occurs when the rate of homogeneous nucleation of bubbles is very large due to superheating, and when the surface temperature exceeds 90% of the critical temperature (T_c) [Xu (2002)]. As a consequence, the material is turned from a superheated liquid into a mixture of liquid droplets and vapor, being explosively ejected from the surface. The onset of phase explosion is marked by the observation of liquid droplets in the ejected material, and a sudden increase in ablation rate. Researchers had observed liquid droplets in the plasma plume of some metals [Kelly and Miotello (1999); Bulgakova and Bulgakov (2001)]. Following the rapid expansion, the material relaxes towards the binode.

Lorazo et al. (2003) and Miotello and Kelly (1995) performed molecular dynamics studies of systems under irradiation with pulses of durations from femtoseconds to picoseconds. For irradiation with ultrashort pulses (pulse duration ≤ 1 ps), and specially close to the threshold energy, the heating is so rapid that the material gets superheated near-isochorically [Lorazo et al. (2003)]. It takes about 1 ps for the laser energy to be transferred to the atoms/ions. Thermal expansion cannot take place at this timescale, and hence, a highly pressurized and superheated liquid is formed. Subsequently, the pressure is released through expansion, beginning from the surface(s). At high energies, the release of pressure by expansion causes fragmentation of the liquid [Perez and Lewis (2003)]. At lower energies, the expanding material reaches a metastable state (spinodal) after the onset of adiabatic cooling and approaches the liquid-gas regime. Homogeneous nucleation of bubbles takes place around this time, and separation of liquid and gas phases begins, also called phase explosion. When phase explosion happens under conditions when compressive stresses have been generated, the material is ejected with higher velocities and is more fragmented [Zhigilei et al. (2009)].

Coulomb explosion is also observed in metals during irradiation with ultrashort pulses, and is also called cold ablation. The incident radiation couples with the valence electrons

in the metal and excites them. The excited electrons gather large kinetic energy and leave behind the positively charged ions. The closely packed ions repel each other and the metal explodes out, forming a plasma. Coulomb explosion is inhibited when the mobility of the conduction band electrons is very high.

For irradiation with nanosecond and picosecond pulses, thermal diffusion and expansion cannot be neglected. The initial non-homogeneous (and sometime metastable) state evolves beyond or along the binodal, albeit close to it, in a non-isochoric manner. It comprises a highly pressurized superheated liquid too. The homogeneous bubble nucleation in this superheated liquid initiates phase separation, which occurs during heating itself. The subsequent cooling is non adiabatic. Fragmentation of liquid under short pulse ablation has often been suggested as the primary mechanism of ablation [Perez and Lewis (2002)].

The heat diffusion occurs at the time scale of 10 ps. When the thermal expansion occurs at the time scale equal to or greater than this, the material cools along the binodal and phase explosion is not observed, as is generally the case in nanosecond laser irradiation. An upper limit of the pulse duration, equal to 10 ps, has been suggested by Lorazo et al. (2003) for observing phase explosion.

On the contrary, some researchers [e.g. Xu (2002); Song and Xu (1998); Bulgakova and Bulgakov (2001); Lu et al. (2002); Zhigilei et al. (2009)] have talked about the presence of phase explosion as an ablation mechanism under high fluence nanosecond laser ablation. This is argued for by the fact that the estimated time lag for nucleation ranges from 1 ns to 10 ns, which is less than a typical nanosecond pulse. For shorter pulse durations, like femtosecond pulses, this argument is unable to explain the reason for phase explosion. Nickel has been reported to undergo a transition from surface evaporation to phase explosion at the laser fluence of 5.2 J/cm^2 , at the surface pressure of 600 bar. It should be noted that this pressure is lower than the equilibrium surface pressure for Ni at the time of phase explosion, and the Clausius-Clayperon equation is not valid in nanosecond pulsed laser evaporation. It will be appropriate to conclude that for nanosecond and shorter pulses, phase explosion occurs whenever the material reaches the thermodynamic critical temperature [Bulgakova and Bulgakov (2001)] and sufficient critical vapor nuclei are formed.

1.5 Mechanism of laser ablation of polymers

For ablation of polymers by a nanosecond UV laser, the ablation process is a combination of thermal (pyrolytic) and photo (photolytic) ablation [Dyer (2003); Srinivasan et al. (1986); Dijkkamp et al. (1987); Feng et al. (2000)]. Since the pulse duration here is much larger than that of ultrashort pulses, non-linear processes like multi-photon absorption do not occur [Srinivasan et al. (1986)]. Pyrolytic ablation starts with absorption of the incident photons and electronic or phononic excitation of the material. It however proceeds via random distribution of this energy amongst the various degrees of freedom of the constituents (molecules) which in turn leads to heating of the material. The heated material ablates via both melt/vaporization and thermal degradation (bond-scission leading to fragmentation) routes. Avalanche breakdown and plasma creation due to inverse Bremsstrahlung also play a role. Both these processes happen in the ground state of the constituents [Dyer (2003)]. This is significantly observed for higher wavelength (low energy photons) and longer pulse lasers ($t_p \geq 1\mu s$). The two basic reasons for pyrolytic ablation are that, firstly, the energy from the low energy photons is transferred to the electrons and then to the lattice in the form of heat energy. The photons do not carry enough energy to cause any other effect, e.g. breaking the covalent bonds in the material. Secondly, the duration of irradiation (t_p) is significantly larger than the electron relaxation time (t_e) and the energy from the photons begins to travel into the material during the irradiation, leading to heating of the vicinity of the area being irradiated. Pyrolytic ablation often leads to a heat affected zone (HAZ) around the irradiated area, thermal degradation and evidence of melt flow. These effects, however, are generally not significantly observed in case of ablation of polymers with nanosecond lasers.

Photolytic ablation is a photo-chemical process that involves bond breaking and formation with the aid of incident photons. Polymers are composed of elements (like C, O, H, N, F, Cl etc.) joined together by covalent bonds. The incident photons, if sufficiently energetic, can modify the bond structure within the material leading to bond-scission or cross-linking effects. The intensity of radiation is so high in nanosecond UV lasers that the number of bonds that are broken are several orders of magnitude higher than those that are formed.

Table 1.3: Bond energies in eV [from Meijer (2004)]

Si-Si, Cl-Cl	1.8 - 3.0
C-N, C-C	3.0 - 3.5
C-O, C-H	4.5 - 4.9
C=C, C=O	7.0 - 8.0

This, however, requires that the incident photons carry sufficient energy to break the covalent bonds. Typical bond energies of some common covalent bonds are given in Table 1.3 that may be compared to the energy of photons as mentioned in Table 1.1. Upon comparison it can be inferred that UV lasers ablate primarily through photolytic ablation owing to the high energy of the photons, although this will be further explained in the following section. The incoming photons break the covalent bonds in the long polymer chains resulting in generation of several smaller chains present within the same volume [Jensen (2004); Meijer (2004)]. This fragmentation or decomposition of the polymer happens when the reactants are in electronically excited state [Dyer (2003)]. When the number of chains in a unit volume exceed a certain value, which means that when the bond density in that volume decreases below a critical value, the smaller chains explode out in the form of vapor and small particles. This explosion leads to expelling of the material and ablation.

1.5.1 Nature of ablation

Pure photolytic ablation, also called cold ablation, is unlikely with nanosecond lasers. Several researchers have observed signatures of both pyrolytic and photolytic ablation in polymers. Dijkkamp et al. (1987) observed through time resolved reflectivity measurements that the ablation of poly-methylmethacrylate (PMMA) and poly(3-butenyltrimethylsilane sulfone) (PBTMSS) was entirely due to pyrolytic ablation with KrF excimer laser. Feng et al.

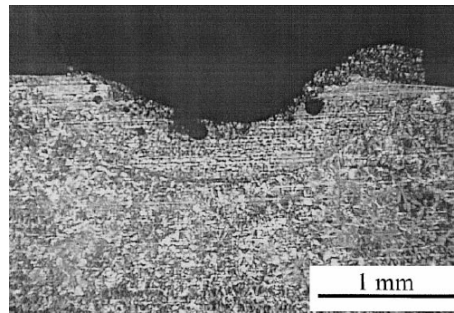


Figure 1.2: The cross sectional micrograph of an ablated crater in PP showing the rim formation [from Feng et al. (2000)]

(2000) studied the ablation of polypropylene (PP) with KrF excimer laser. They observed that even with fluence near the ablation threshold of the polymer, ablation was observable on the surface. Although the ablation was due to expelling of fragments generated after polymer chain scissions, the scission was caused not directly by the photons but by the heating of the polymer surface by the radiation. A rim of solidified polymer was observed around the ablated crater suggesting that polymer had melted and flown out of the surface and then resolidified around the crater (see Fig. 1.2). The observation that the rim increased in size with increase in fluence and the number of pulses suggests accumulation of heat with higher fluence and number of pulses. Dyer (2003) observes that polymers that are thermally robust (like polyimides) have been confirmed to ablate by extensive fragmentation, indicating that photolytic ablation resulting in covalent bond scission was the active mechanism.

Relative importance of the two ablation mechanisms have also been studied by researchers. Feng et al. (2000) found that photoablation dominates at very low or very high fluence. For the fluence range generally used in ablation pyrolytic ablation was found to be dominant. However, since laser ablation employs irradiation with several pulses, a cumulative effect of both processes is always observed. Jensen (2004) suggested that the relative dominance can be checked by comparing the values of the optical and the thermal penetration depths of a material for a particular wavelength and pulse duration.

1.5.2 Plume interaction during the laser pulse

Pulses of KrF excimer laser, for example, last for few tens of nanoseconds. Immediately after a pulse hits the material, a high temperature plasma plume is formed that contains gaseous components, small fragments and radicals. This plume is continuously fed by the fragments being expelled out from the material surface during the pulse. Since the plume is developed almost immediately after the pulse hits the material, a significant portion of the pulse strikes the plume while on its way to the material surface. The plasma plume (i.e. the species present in the plume) are known to significantly absorb and reflect the incoming radiation and letting only a small portion of it through. Then the effective absorption coefficient of the material is considerably reduced and leads to a lower extent of ablation (etch rate). Some consequences of the plasma plume absorption are the saturation of the ablation rate with fluence and temporal shift of the surface temperature maximum from the laser pulse maximum [Bulgakova and Bulgakov (2001)]. For a highly absorbing plume with large electron density, low fluence results in efficient ablation of the material surface and vice versa. Using a high fluence, in this case, leads to heating of the plume and hence to undesirable thermal effects [Dyer (2003)].

1.5.3 Ablation rate and threshold

Ablation rate is one of the most studied parameters in laser machining of polymers. The ablation rate is also called the etch rate and is defined as the depth (ablated) per pulse of laser. It is either measured in nanometer, or in micrometer, and is an average quantity. It has been always observed that the threshold fluence must be exceeded in order for ablation to set in. This is required across the entire band of wavelengths. For sub-100 ns pulse duration lasers, the fluence threshold is independent of the pulse duration. This, however, is not true for longer duration pulses [Dyer (2003)]. It is still a matter of investigation and debate as to whether a true ablation threshold exists for a material. The etch depth and ablation rate have been measured for biaxially-oriented polyethylene terephthalate (boPET) when irradiated with KrF excimer laser [Akhtar et al. (2013a)]. The measurements are shown in Fig.

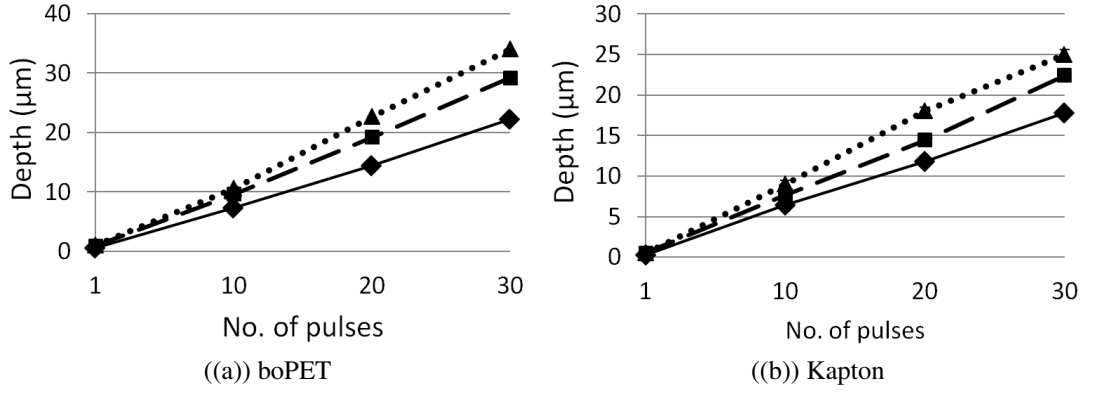


Figure 1.3: Ablation depths plotted as functions of the number of pulses for various fluences during micromachining of 100 μm wide channels in boPET and Kapton by excimer laser [from Akhtar et al. (2013a)]. The \blacklozenge , \blacksquare and \blacktriangle indicate machining at the fluences of 3, 4 and 5 J/cm^2 , respectively.

1.3, where the ablation rate was seen to increase with fluence and was constant upto a certain number of pulses for the same fluence. Etching of polymers have been observed in the vicinity (lower) of ablation thresholds. In their study of ablation of polyimide using excimer lasers, Küper et al. (1993) found smooth curves for etch rate versus fluence, suggesting the absence of any kind of ablation threshold. A sharp threshold has, however, been observed with ArF (193 nm) laser while machining polyimide. A clearer description of polymer behavior at high temperatures or energy densities is difficult at this time due to the absence of experimental data regarding this process.

In the domain of photolytic ablation, if a minimum of ' n ' bonds per unit volume of the material need to be broken to initiate ablation, the threshold fluence, F_{th} , can be expressed as

$$F_{th} = nh\nu/\eta\alpha(1 - R), \quad (1.2)$$

where η is the quantum efficiency of bond-scission, $h\nu$ is the photon energy and R is the surface reflectivity. The quantum efficiency of bond scission increases with decrease in wavelength. Hence η for ArF laser is more than that for KrF laser. The η for KrF, however, can be increased by increasing the temperature so that the photochemical processes are accelerated [Srinivasan et al. (1986)].

In the domain of pyrolytic ablation,

$$F_{th} = C_v(T_{th} - T_s)/\alpha(1 - R), \quad (1.3)$$

where C_v is the volumetric specific heat capacity of the material, T_{th} is the minimum temperature required to be reached to initiate thermal degradation of the material and T_s is the surface temperature of the material [Dyer (2003)].

The intensity of radiation at a depth y into the material ($I(y)$) follows the Beer's law of attenuation,

$$I(y) = I(0)e^{-\alpha y}, \quad (1.4)$$

where $I(0)$ is the intensity at the surface.

The etch rate (depth per pulse, d) shows a logarithmic dependence on the fluence and follows the relation $d = \alpha^{-1} \ln(F/F_{th})$, where α is experimentally determined. The etch depth varies linearly with the log of fluence for values of fluence ranging between F_{th} and a certain upper limit. For a constant fluence, the etch depth varies linearly with the number of pulses. Decrease of etch rate at high fluence is due to secondary absorption of incoming photons by the expelled products (present in the plume) and distribution of the irradiation over the walls of the ablated crater. Also, low energy pulses do not break enough number of C-C bonds and hence lead to small etch depths. Moderate energy pulses are able to break enough number of C-C bonds that leads to efficient ablation and comparatively greater etch depth. High energy pulses break a large number of C-C bonds but over the same polymer mass (albeit into smaller polycarbon fragments that explode out) leading to almost the same etch depth. Hence beyond a particular pulse energy (fluence), the efficiency of photolytic ablation levels off [Dayal et al. (2013a)].

1.6 Survey of laser micromachining of metals

Machining metals has long been a forte of lasers. Nd:YAG and CO₂ lasers, for example, are widely used in drilling, cutting, welding, cladding, alloying of metals [Meijer (2004)]. Naeem et al. (2008), for example, explored the effects of pulsed Nd:YAG laser parameters on drilling about 500 μm diameter holes in turbine blades made of a nickel super alloy, and observed that higher pulse width and higher power laser pulses produced quicker drilling. Taper and hole roundness and formation of recast layer were also studied. Byskov-Nielsen (2010) performed studies on nanosecond (infra-red) laser micromachining of holes on steel. A better surface quality was reported from micromachining at low repetition rates.

From the application point of view, it is the quality of the final product of laser micromachining (for example, a drilled hole or a channel) that matters. Hence the characterization of the final product is essential. In order to do so, several factors like repeatability, taper, circularity, spatter formation, grain structure modification, residual stresses etc, need to be acknowledged and assessed. Such investigations have been carried out by researchers earlier. The most studied geometry is a hole feature on metals and polymers, where parameters like the mean hole diameter, depth, inlet cone and exit cone angles, surface debris, temperature variations, effects of assist gas, characteristics of spatter formation, melt ejection and particle size distribution have been studied [Yilbas and Yilbas (1987); Yilbas (1987); Han (1999); Low et al. (2000); Ng and Li (2001); Ghoreishi et al. (2002); Han et al. (2004); Voisey et al. (2003)].

Use of assist gases while machining metals has been an area of interest. The assist gases are used to either catalytically enhance the material ablation rate, or to prevent spatter formation and resolidification at the edges. Brannon (1989) report about the differences in surface quality obtained during excimer laser micromachining of single and polycrystalline copper, in the presence of chlorine gas. Robinson and Jackson (2006) used various kinds of assist gases while machining aluminum with a femtosecond laser. Recast material has been observed with machining under air, argon and oxygen, whereas, machining under helium generated a much cleaner surface. The guidelines, to achieve good surface quality, were

mentioned to be machining at high workpiece scanning speeds and with many pulses. Yeo et al. (1994) report on the use of air, oxygen and some inert gases as assist gases while microdrilling holes in super alloys. Generally, the assist gases assist in ejection of the melt, shielding of the machine optics from the ablation products. On the contrary, it has been reported that the assist gas tends to decrease the speed of material ejection [Rodden et al. (2001)]. Reactive gases, like oxygen, tend to enhance the ablation rate by oxidation of the material, thereby raising the local temperature and enhancing the rate of vaporization. Oxygen is generally used as an assist gas with alloys of nickel, molybdenum, chromium and iron. Aluminum alloys are machined in air, whereas ceramics are preferred to be machined under nitrogen atmosphere. Inert gases are used with titanium alloys [Ratchanikorn (2011)]. The material specificity of the effect of ambient atmosphere has been reported by Mendes and Vilar (2003). Arnold (1994) performed excimer laser micromachining of various metals and reported no effect of the various ambient atmospheres used. Mendes and Vilar (2003) performed excimer laser micromachining of alumina ceramics, and observed considerable dependence of the ablation rates on the ambient atmospheres used. The highest ablation rate was observed for machining under helium, an observation attributed to the high thermal conductivity and ionization potential and low molecular mass of helium.

Many authors have described the temporal evolution of the temperature field during laser material interaction as one of the most significant factors in achieving a desired quality of machining. Numerical simulation studies from simple one-dimensional models for evaporation [Ready (1971)] to complex three-dimensional heat transfer models that consider the laser intensity distribution (Gaussian vs homogeneous) [Lim and Yoo (2011)], melt dynamics, surface evaporation, recoil pressure and pulse-plume interaction [Mazumder and Steen (1980); Shen et al. (2001); Von Allmen (1976); Anisimov and Khokhlov (1995); Semak et al. (1997)] have been carried out. Techniques such as the element birth-and-death method [Conrad et al. (2008)] and element switching [Karbasi (2008)] are some of the ways employed in finite element methods to simulate material removal with temperature being the key parameter in determining the geometry of the feature. These have been used in problems relating to thermal deformation and laser engraving. The element birth-and-death method

involves activation-and-deactivation of an element by changing one or more of its properties in a manner that it either significantly interferes or does not interfere with the physics of the simulation. The element switching method is similar to the former and involves changing an element from one material to another by changing one or more of its properties.

1.7 Survey of laser micromachining of polymers

The excimer laser has become a workhorse for machining of unconventional materials like ceramics and polymers and is used for a variety of material modification, feature generation and texturing purposes at the micro- and nanometric length scales [Kawamura et al. (2010); Meijer et al. (2002)]. Excimer laser micromachining with mask projection is a fast, one-step technique that works well with all kinds of materials down to very small feature size. The minimum feature size attainable can almost literally be the diffraction-limited spot size of the laser beam. The short laser pulse (20ns in this case with KrF excimer laser) thus minimizes the thermal effects of ablation, mainly the heat affected zone (HAZ) [Dubey and Yadava (2008); Meijer (2004)]. The large photon energy ($\sim 5eV$) associated with these lasers can dissociate most of the bonds within and between the molecules. Thus excimer lasers generate sharp features when used with ceramics and polymers through cold (or photolytic) ablation.

Polymers have been one of the widely used work pieces for laser micromachining. Fabrication of Lab-on-a-chip devices [Manz et al. (1990)], radio-frequency identification (RFID) tags, ink jet nozzles [Ricciardi et al. (1998)] etc, require machining of channels, vias or holes in polymers at some stage of production. Fabrication of high-aspect ratio holes in various polymers [Lazare and Tokarev (2004)] and channels of varying cross-sections by workpiece and mask dragging [Rizvi (1999)] have been demonstrated on polymers. With demands for better quality of machined features (clean ablation, clean surfaces etc) and faster processing times, researchers have focused on studying if the ambient atmosphere can help achieve cleaner ablation, faster etching and lesser spatter. There are several studies on machining depth and ablation rate in different polymers using CO₂ and excimer lasers [Dubey and Yadava (2008); Lazare and Tokarev (2004); Jensen (2004)] and aspect ratio for very deep holes

[Lazare et al. (1999)]. However, all such studies have been conducted under normal atmosphere. Although laser machining under controlled atmospheres has been studied for metals and alloys using Nd:YAG lasers [Robinson and Jackson (2006); Low et al. (2000)], and for ceramics and semi-conductors using excimer lasers [Heydel et al. (1993); Mendes and Vilar (2003)], we could not find a similar study conducted for polymers, especially with excimer lasers.

The abundance of quantitative and qualitative data notwithstanding, the underlying mechanism(s) of polymer ablation (photolytic ablation) continues to attract investigators from around the world. The most widely used analytical/quantitative models of photolytic ablation use Beer's law as their basis for absorption of light. This gives a logarithmic dependence of the ablated depth per pulse on the fluence, which is valid for a very narrow fluence range [Sutcliffe and Srinivasan (1986)]. Use of higher fluence leads to several allied mechanisms that operate simultaneously, e.g. strong plasma plume absorption of incoming laser pulse, entrapment of ejected fragments by the plasma plume and release of gases from the irradiated bulk leading to swelling of the polymer. These models do not consider intra-pulse dynamics of ablation and the time duration of the laser pulse. Several findings, however, suggest that ablation sets in within the time span of the laser pulse [Sutcliffe and Srinivasan (1986)], and the mechanism of ablation, as well as the feature quality, are widely different for long and short pulses [Meijer et al. (2002)].

Chapter 4 discusses the excimer laser micromachining, at different length scales, of features on three different types of polymers, under three different atmospheres, and under varying machining conditions. The machined depth, effect of ambient atmosphere and feature size effect have been studied. The ambient gas had no effect on the ablation rate indicating an almost photolytic origin of ablation. A theoretical model including plasma plume absorption accurately predicts the ablation rate.

1.8 Survey of laser micromachining of metal films

There is an increasing requirement for rapid and large scale micro patterning of metallic thin films for manufacturing of MEMS devices, electronic circuit boards, miniaturized microwave circuits, and photonic devices. In particular, there have been tremendous developments during the past decade in the fields of metamaterials [Ramakrishna and Grzegorzcyk (2009)] and plasmonics [Maier (2007); Nagpal et al. (2009)] where exceptional electromagnetic/optical properties can be obtained by suitably structuring the surfaces of thin films of metals like gold, silver and aluminum. They have a variety of applications such as frequency selective surfaces [Weiner (2009)], diffractive micro-optics [Herzig (1997)], perfect absorbers of radiation [Watts et al. (2012)], materials with extraordinary properties such as negative refractive index [Ramakrishna and Grzegorzcyk (2009)], sub-wavelength imaging [Ramakrishna and Grzegorzcyk (2009)], photovoltaic technologies, beam shaping and laser applications.

Laser machining [Dhote et al. (1995)] of thin metal films have long been an area of research due to its use in device fabrication technologies. Hybrid multilayer polymer-porous metal oxide photovoltaic devices [Ravirajan et al. (2005)], terahertz pulse shaping devices [Agrawal et al. (2005)], polarization-insensitive metamaterial absorbers [Landy et al. (2009)] and left handed materials [Shelby et al. (2001)], are some of the devices that require patterning of thin metal films. We expect to demonstrate excimer laser micromachining as a better (simpler and quicker) alternative to various other techniques currently being used to fabricate the above mentioned devices. Direct machining of metal films finds wide use in manufacture of binary masks. Excimer laser machining of metal films have been well studied by Andrew et al. wherein several advantages of using these lasers were drawn out [Andrew et al. (1983)]. We also note that excimer lasers have been preferred for micromachining of polymers [Lazare and Tokarev (2004); Rizvi (1999); Lazare et al. (1999); Tokarev et al. (2000); Saxena et al. (2009)] due to the large photon energy and the consequent photolytic ablation process. The low reflectivity of metals in the UV wavelength range allowing for high laser-material coupling, low wavelength allowing for sub-micron resolution, short pulse duration

allowing minimal heat affected zone and high beam energy and cross-sectional uniformity allowing for large area patterning make the excimer lasers an ideal choice for metal film micromachining.

Until 1980s, fabrication of integrated circuits traditionally involved photo-lithographic techniques. These techniques, besides having other disadvantages, had limitations relating to the throughput rate and quality of etch. Researchers had been exploring ways to directly machine metal-film coated substrates that would outdo the use of etchants. Lasers were found to be highly efficient in direct machining of metal films. Some of the earliest works in laser machining of thin metal films have been reported in 1960s. Cohen et al. (1968) have demonstrated the machining of gold, nichrome and tantalum films on silica, quartz and glazed alumina substrates using YAG lasers to produce integrated circuit elements (resistors and capacitors). Koo and Zaleckas (1978) were one of the first groups to patent the use of laser beam to explosively remove thin films from insulating substrates. Shibasaki et al. (1980) successfully demonstrated and patented a thin-film microcircuit board fabricated by evaporation of thin metallic film by high intensity light. Geller et al. (1982) had demonstrated the trimming of thick-film resistors using lasers.

In recent times, Kuhnke et al. (2006, 2005) had machined microchannels on Aluminum films deposited on carbon and observed that higher spot overlap reduce the spatter density inside the machined channels. Guo et al. (2009) have devised a novel method of fabricating gray scale masks by machining thin films of tin. Although a lot of researchers employ lasers to machine and pattern thin films, a systematic study of the machining parameters and their effects on the quality of fabricated features is required to be carried out. This work is an effort to understand how laser machining can be optimally used to fabricate microfeatures with good quality.

The structural difference between metal films and bulk metals manifests itself in the completely different modes of ablation in these two materials. Whereas ablation threshold, melt/vaporization and recoil pressure dictate bulk metal ablation to a large extent, these are not found to play a considerable role in thin film machining. In fact, thin film ablation has been observed to start well below the bulk ablation threshold and the fusion temperature

of the material [Andrew et al. (1983)]. A detailed investigation of ablation of thin film of tungsten revealed that at low fluences, the film ablated in solid pieces flying directly away from the substrate [Toth et al. (1995)]. Moderate fluences caused in-flight fragmentation of the ejected solid pieces, whereas high fluences caused ejection of molten and vaporized material, in addition to highly fragmented solid pieces. The thin-film ablation threshold has been reported to increase linearly with the thickness of the metal film upto its thermal diffusion length, beyond which it becomes independent of the film thickness, and becomes equal to the bulk ablation threshold [Matthias et al. (1994)]. Beyond a certain thickness of the metal film, substrate damage is observed before the film is ruptured [Zaleckas and Koo (1977)].

The adhesion characteristics of the metal films to glass substrates, determined by the oxygen-affinity of the metal and the thickness of the oxide layer formed at the metal-glass interface, are also important. Thicker oxide films lead to greater adhesion strength with the adhesion increasing in time after deposition of the metal film due to diffusion of oxygen into the film and thickening of the oxide layer Benjamin and Weaver (1961). Benjamin and Weaver Benjamin and Weaver (1961) investigated the adhesion strength of several metals on glass, using a loaded needle with smooth tip across the top of the film. The adhesion strength was measured in terms of the load required to scratch the film. Chromium films demonstrated an initial adhesion of 100–150 g, which soon rose to greater than 500 g. The rise was attributed to the growing of oxide film at the interface, driven by the diffusion of oxygen atoms through the chromium film over time. The cracks observed on the film allowed in the diffusion of oxygen. Aluminum films, on the other hand, demonstrated initial adhesion strength of 7 g, which rose over time and settled at around 70 g. The weaker adhesion of aluminum, as compared to chromium, despite its greater affinity for oxygen, was attributed to the inability of the metal oxide layer to grow at the interface. The inability of oxygen atoms to penetrate the protective oxide coating on the top of the aluminum film, and the continuous structure of the metal film, starved the interface of oxygen.

It is understood from these observations that the metal film, instead of getting ablated, gets pushed out from the interface due to an ejection force. The origin of this force could be

the rapidly expanding metal at the interface or the gaseous inclusions being expelled from the glass substrate at higher temperatures [Zaleckas and Koo (1977); Veiko et al. (1992); Andrew et al. (1983)]. The metal film in the irradiated region, while being ejected out, carries away with itself non-irradiated portions from around it, thereby tearing the metal film and distorting the shape of the pattern being machined. Such an effect becomes more pronounced as the lengthscale of machining is reduced. At the lengthscale of a single micrometer, it is not even possible, with the existing techniques, to directly micromachine features using a laser. It has also been reported that films melted by the laser beam tend to splash out, and hence peel the surrounding film in the process [Miyamoto and Hayashi (1995)]. The thermo-mechanical nature of thin-film ablation would allow a sharp ablation boundary if the surrounding non-irradiated regions of the metal film could be mechanically protected and clamped.

In the work reported in this thesis, excimer laser has been used to machine microfeatures at lengthscales ranging from 100 micrometers to a single micrometer on thin aluminum, chromium and gold films coated on borosilicate glass. The choice has been made to have metals with low and high fusion temperatures, as well as with strong and weak adhesion to glass. The films have been machined directly as well as after applying a thin coating of polymer [polyvinyl alcohol (PVA), a water soluble polymer] on top of the metal film. It should be noted that sacrificial polymer coatings have been earlier used to prevent spatter during laser machining [Low et al. (2001)]. The microfeatures are characterized by their edge roughness, lateral overcut (channel width) and boundary integrity as a function of the process parameters like laser fluence, spot overlap and distance between channels (pitch). The polymer coated metal films are machined to a high degree of finesse showing sharp machined features down to the single micrometer level, an achievement not otherwise possible by direct laser micromachining. The thin film ablation, as well as the enhanced micromachining using the polymer-coated metal films, are understood by studying a thermal model that predicts the temperature distribution in the film and the substrate during a single pulse laser irradiation, which lasts a few nanoseconds.

In this work, we have demonstrated that excimer laser micromachining of a thin metal

film can be made precise by coating the metal film with a sacrificial thin film of polymer, whereby the polymer film protects the metal film from tearing during the ablation process. Thus, it is a superior (simpler and quicker) alternative to various other techniques currently being used to fabricate the above mentioned devices. We demonstrate the ability to machine microfeatures (straight channels) at lengthscales ranging from 100 micrometers to a single micrometer on thin aluminum, chromium and gold films coated on borosilicate glass.

1.9 Summary

The mechanisms of nanosecond UV laser ablation of metals and polymers, and reviews of laser micromachining have been discussed in this chapter. The pulse duration and the material properties dictate the kind of interaction that takes place between the laser and the material. Ablation in metals is pyrolytic while that in polymers is almost always a combination of pyrolytic and photolytic ablation. Evidence of occurrence of both these processes have been found by researchers. Higher wavelength and long-pulse lasers ablate mainly by pyrolytic process. Photoablation was found to dominate at very low fluence (when the fluence is not enough to cause significant heating of the material) and very high fluence (thermally accelerated photo decomposition and inverse Bremsstrahlung). The plasma plume formed during the ablation absorbs a significant part of the incoming radiation and may also lead to thermal effects. Ablation threshold needs to be overcome in order for ablation to set in. Existence of a true ablation threshold, however, is still a matter of debate. The ablation depth is found to vary linearly with the log of fluence. The ablation rate is found to decrease at higher fluence because of secondary absorption of incoming photons by the plasma plume.

1.10 Objective of the thesis

The objective of the work carried out as part of this thesis is to develop an understanding of the excimer laser micromachining of metals and polymers, in terms of the ablation rates and feature quality, and is directed towards the use of this technique to directly pattern metal and

polymer surfaces, along with metal films. The algorithms to accurately position the workpiece at the image plane of the mask, to scan the workpiece, and to interface the switching of the laser with the movements of the workpiece, need to be developed. With the learnings on the excimer laser micromachining of metals and polymers, direct patterning of metal and polymer surfaces needs to be demonstrated.



Chapter 2

Experimental setup, procedures and characterization techniques

A description of the setups and procedures used to carry out the various fabrications and characterization studies is presented in this chapter. The excimer laser machine is described in terms of its setup and operational parameters. The modes of operation of the laser and of obtaining the laser pulses are described. A brief introduction of the laser micromachining setup follows, that includes the micro-positioning stage. The mask projection technique used for micromachining is discussed in detail, followed by brief discussions of the methods of mask manufacture. The characterization techniques and procedures used for characterizing the micro features are briefly introduced. Detailed descriptions of the procedures used to micromachine metals, polymers, metal films and micro-lens arrays follow. The chapter concludes with a discussion on the sources of error in the experiments.

2.1 The excimer laser machine

The excimer laser machine used is COMPex Pro 205 from Coherent GmbH, Germany. This KrF excimer laser machine delivers laser at 248 nm wavelength. The specifications of the machine are mentioned in Table 2.1. The laser tube in the machine contains preionization pins, electrodes, a gas circulation fan, an electrostatic dust filter and heat exchanger coils. The laser is generated from the excimer gas after a high voltage discharge between the electrodes, that lasts for about 50 ns. The peak power of the discharge can reach one gigawatt. The laser gas is preionized to obtain a controlled and spark-free discharge. The resonator optics comprises a plane-parallel resonator and an inbuilt energy monitor. The machine is controlled through a central laser control board that is interfaced with a hand-held keypad. The machine can be triggered by external signals and can also generate synchronization pulses. The excimer laser is classified as a Class 4 laser according to ANSI Z136 standards. The laser machine is equipped with safety interlocks, and wearing protective eye wear while operating the machine is a prerequisite. [Salient features of the machines taken from Coherent (2008)].

Table 2.1: Specifications of the excimer laser machine COMPex Pro 205

Wavelength	248 nm
Maximum repetition rate	50 Hz
Maximum pulse energy	700 mJ
High voltage range	18 - 27 kV
Demagnification ratio	10
Pulse width	20 ns
Average power	30 W
Beam dimension at generation	24 mm × 10 mm
Beam dimension at the mask plane	20 mm × 20 mm
Energy efficiency	≈2%

2.1.1 Modes of fixing the energy of the laser pulses

The energy of the laser pulses is a function of the high voltage discharge and the age of the excimer laser gas. As the gas ages, the energy obtained from a given high voltage discharge decreases. The machine can be operated in two fundamental running modes. The two modes in which the energy of the pulse can be fixed are the constant high voltage (HV CONST) and the constant energy (EGY CONST) modes. In the EGY CONST mode, the high voltage is adjusted to generate pulses of fixed energies. The maximum energy that can be delivered in a single pulse depends on the quality of the excimer gas, while not exceeding 700 mJ. In the HV CONST mode, the value of the high voltage used to generate the spark is fixed by the user. It can take any integer value between 18 and 27 kV. The pulse energy delivered is determined both by the high voltage and the quality of the excimer gas.

In addition to the two fundamental running modes, the laser machine can be operated with or without gas replacement. In the no gas replacement (NGR) mode, there is no gas action taken while operating the machine. In the partial gas replacement (PGR) mode, macro halogen injections are performed to improve the quality of the gas. In case a complete replacement of the excimer gas is required, the NEW FILL mode is activated by the user.

2.1.2 Modes of triggering pulses from the laser machine

There are several modes in which pulses can be delivered by the machine. The operator can decide the frequency of such pulses, the number of pulses, and the condition under which the pulses are delivered. These modes are mentioned below.

- Internal triggering (INT) - The pulses are triggered by the machine's internal trigger generator. The trigger frequency is fixed by the user.
- Internal gated triggering (INTG) - The pulses are triggered by the internal trigger gen-

erator as long as there is a high signal at the external trigger socket.

- External triggering (EXT) - The pulses are triggered by an external trigger generator connected to the external trigger socket.
- Countdown mode - There is a limit to the number of pulses to be triggered. Any mode of triggering can be used.
- Burst mode - The laser can be operated in a sequences of pulses, each sequence temporally separated from the other.

The external trigger socket is a Bayonet Neill–Concelman (BNC) socket that takes 3.3 V to 5 V DC TTL signals. Similar signals are generated from the synchronization socket.

2.2 Laser micromachining setup

The laser micromachining setup comprises the laser machine and the micro-positioning stage. The experimental setup for laser machining using mask projection is shown in Fig. 2.1. Two 8×8 arrayed insect-eye lenses are utilized to create a $20 \text{ mm} \times 20 \text{ mm}$ square field with a homogeneous top-hat intensity profile at the mask plane [Coherent-GmbH (2 March 2013)]. The images on the left and top of the setup show the beam shape, and changes in it, as the laser passes through the beam delivery section. The last image (top right) shows the square cross section of beam at the mask plane, the location at which the mask is placed for machining. The workpiece is positioned on a three axes micro-positioning stage with the resolution of a single micrometer on each axis. The stage is controlled by a Holmarc (Holmarc Opto-Mechatronics Pvt. Ltd., India) micro-position controller, and positioned so that the top surface of the workpiece is at the image plane of the mask. The power of the laser pulses at the mask plane is monitored with a power meter (Coherent, Field Max II) and the intensity at the image plane is hundred times the intensity at the mask plane.

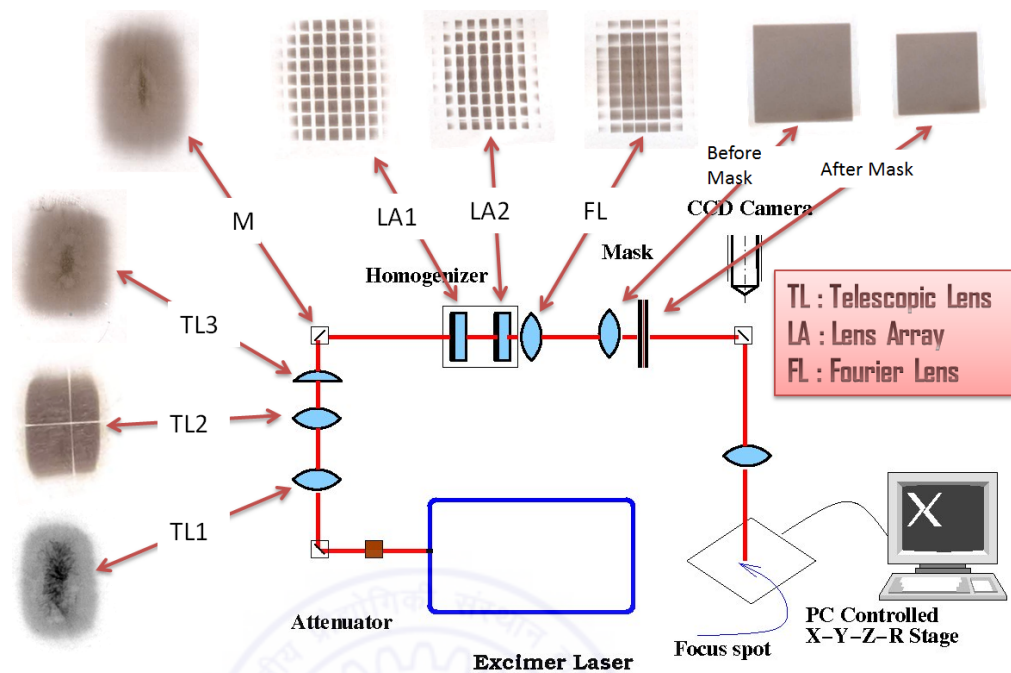


Figure 2.1: Schematic diagram of the experimental setup for laser machining

2.3 Mask projection technique

Excimer lasers are widely used with mask projection. The technique involves use of a mask, through which the laser beam passes before hitting the work piece, as shown in Fig. 2.2. A beam delivery section in the laser machine serves to shape the beam before allowing it to reach the mask. It comprises a number of optics to shape, collimate, homogenize and focus the beam.

A typical focusing arrangement is shown in Fig. 2.3. When a collimated beam passes through a double convex lens, it is converged on to a plane, called the focal plane of the lens. The point of convergence, also called the focal point, is in fact, not a point, but a spot. The spot, with the minimum radius of w_o , is called the beam waist. The minimum possible spot size, to which a beam can be practically focused, is called the diffraction limited spot size, and arises from diffraction (wave) effects. Hence, while using mask projection, it is generally not possible to focus a beam to a size smaller than its diffraction limited spot size.

Lasers with smaller wavelengths can be focused to smaller spots, and vice versa. Hence, it is advantageous to use lasers with small wavelengths (typically in the ultraviolet range), while fabricating micrometer sized features. The spot radius at the beam waist, w_o , is expressed as,

$$w_o = \frac{4\lambda f}{2\pi y_o}. \quad (2.1)$$

The Rayleigh range, z_o , is the distance along the optical axis, on either side of the beam waist, at which the beam area reaches twice its value at the beam waist. Thus, the Rayleigh range is expressed as [Herman and Wiggins (1998)]

$$z_o = \frac{\pi w_o^2}{\lambda M^2}. \quad (2.2)$$

In the expressions above, λ is the wavelength of the laser, M is the beam quality factor, and f is the focal length of the lens. In a laser machining setup with mask projection, the workpiece is kept at the image plane of the mask, with the required placement accuracy of the order of the Rayleigh range. If the workpiece is not properly positioned, a blurred image of the mask features is obtained on the workpiece.

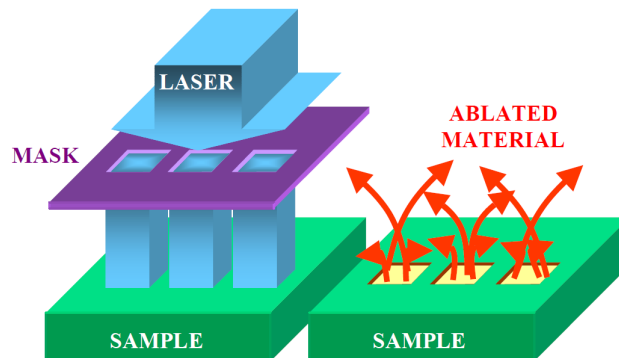


Figure 2.2: Schematic of a mask projection, showing the incident laser beam, passing through a mask with three square holes, before falling on the work piece and ablating a similar pattern on it. [Reproduced from Rizvi (1999)]

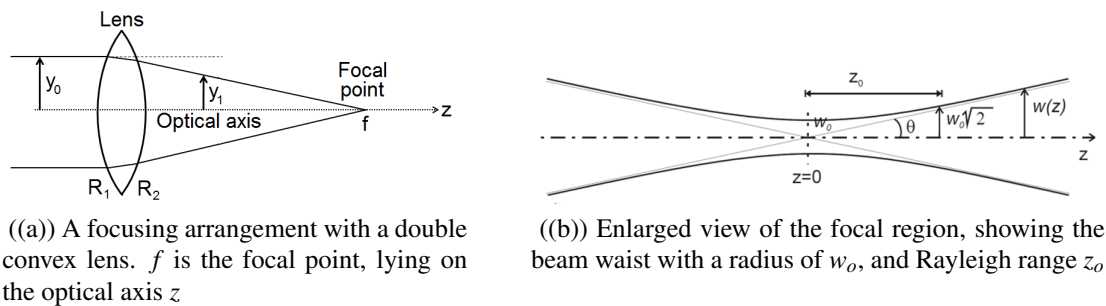


Figure 2.3: Schematic diagrams of a simple optical system showing the convergence of a beam onto a focal plane, with a detailed description of the beam waist

Mask projection employs a mask, which is generally a screen with transparent and opaque portions. The laser beam is allowed to pass through the transparent portion, and the shape of the transparent portion is machined/imprinted on the workpiece by virtue of its ablation. An example of a mask projection setup is shown in Fig. 2.4.

The mask projection technique is a contrast to the direct write technique, and offers several advantages over the latter. The mask and the optics, being away from the work piece, do not suffer any damage due to ablation. Many setups allow movement of the mask as well as the work piece. The combination of mask and work piece scanning provides the ability to produce several complicated features, like arrays of micro features, nested holes, micro-

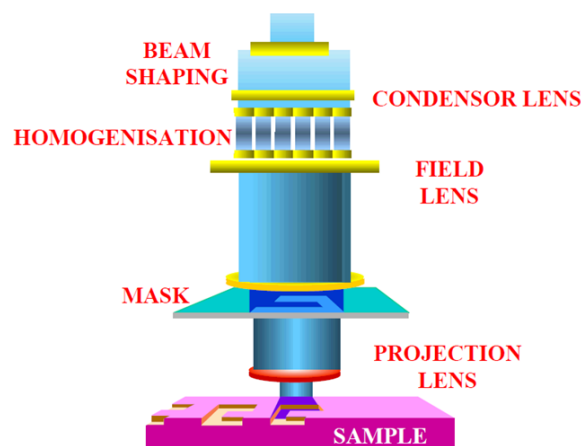


Figure 2.4: Schematic of a mask projection system [Reproduced from Rizvi (1999)]

channels with different kinds of cross sections etc. Since an image of the mask is used to machine micro features, it is possible to de-magnify the image and machine features that are much smaller than those on the mask. Demagnifications of $2\times$, $5\times$ and $10\times$ are widely used. The demagnification allows use of much lower fluences on the mask, thereby saving the mask from laser induced damage.

Several kinds of masks are used in the industry. Binary masks are the most widely used and easiest to fabricate. These generally contain opaque elements deposited on a transparent substrate. These are similar to lithographic masks, but are required to be more resistant to damage, at the large laser intensities used. Gray scale masks are another kind of masks that have varying transmissivity over the cross section. The smoothly varying transmissivity allows fabrication of smooth profiles on the workpiece. These are however much more difficult to fabricate and require calibration of transmissivity to produce desired patterns. Phase shift masks employ interference between portions of a beam passing through two separate regions of the mask, each with a different refractive index. Fine patterns with high contrast and resolution can be produced on the workpiece using such masks, but the masks require complex fabrication. Since binary masks are easy to fabricate, these are mostly used for producing micro features on polymer surface. In the following section we shall present a method to fabricate micro lens array with the help of a binary mask.

2.4 Methods of mask manufacture

Two types of masks have been used in the studies conducted as part of this work, namely, aluminum masks and aluminum coated Kapton (polyimide) masks.

2.4.1 Conventional micromachining of metal sheet

Features in aluminum masks have been fabricated by conventional micromachining techniques such as microdrilling and micromilling. Channels and holes of the characteristic dimensions of 1 mm and 100 μm have been fabricated by this technique.

2.4.2 Micromachining of polymer and metal sheets

Features in Kapton masks have been fabricated by direct machining of the Kapton sheet by excimer laser [Dayal et al. (2013b)]. Sometimes, circular holes were required for use as masks to machine the Kapton sheets. Such circular holes, of diameters ranging from 1 mm to 100 μm were machined in aluminum sheets by microdrilling.

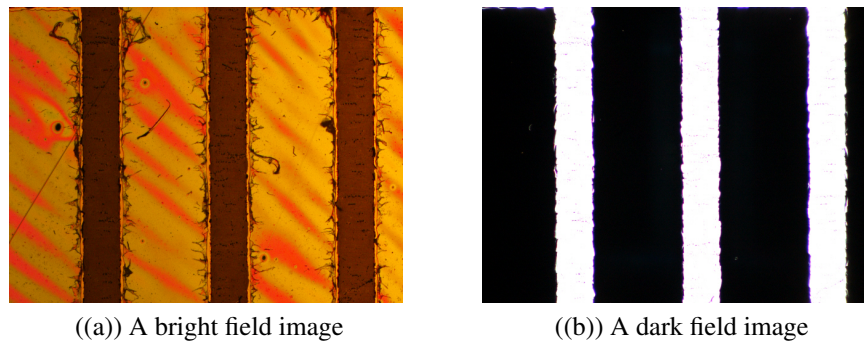
2.4.3 Physical vapor deposition

Polymer sheets cannot be directly used as a mask, because polymers get easily machined even at the low fluence at the mask plane. Hence whenever it was required that the polymer sheet be used as a mask, the sheet was coated by a 200 nm thick film of aluminum, by physical vapor deposition. The reflective aluminum film is able to withstand the fluence falling on it, and helps to keep the mask safe for extended use.

2.5 Characterization techniques and procedures

2.5.1 Microscopy techniques

Microscopy has been used in this work to observe the quality and dimensions of the fabricated micro features in detail. Two types of microscopy techniques - optical microscopy and scanning electron microscopy - have been employed.



(a) A bright field image

(b) A dark field image

Figure 2.5: Examples of optical micrographs of microchannels captured through bright field and dark field imaging techniques

The optical microscope (Olympus, BX51) has both bright field and dark field imaging modes, along with an integrated image acquisition system. Imaging in transmission is also possible. Bright field imaging captures light directly from the sample. It provides low contrast and low apparent optical resolution, with the sample appearing dark on a bright background. Dark field imaging captures scattered light from the sample and the boundaries and peripheries are nicely visualized in the image. It provides a high contrast image and the sample appears bright on a dark background. Images captured in both these modes are shown in Fig. 2.5.

Scanning electron microscopy was performed for high resolution visualization of the fabricated micro features. A field emission scanning electron microscope (FESEM), Zeiss Supra 40 VP, was used to perform the microscopy. The microscope has resolutions of 1.3 nm at 15 kV and 2.1 nm at 1 kV. A maximum magnification of 900,000 \times is possible.

2.5.2 Profilometry techniques

Surface profilometry was carried out for fabricated microfeatures for purposes of qualitative observations and measurements of depths and widths of ablation. Two kinds of profilometry techniques, namely 2D contact and 3D non-contact, were used on polymer and metallic

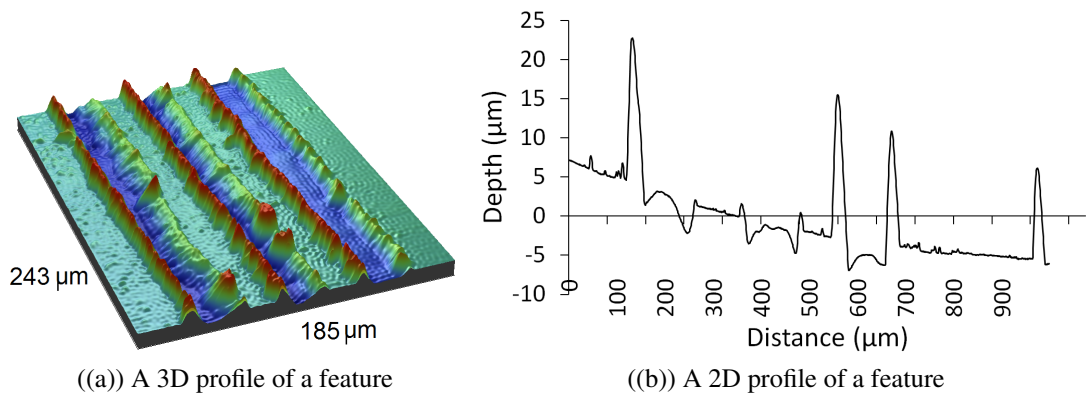


Figure 2.6: Examples of optical and contact profilographs of microchannels

samples. The 2D profilometry was carried out with a KLA Tencor D120 stylus profilometer. A Wyko NT100 white light profilometer was used for 3D profilometry. Typical profiles from the two profilometers are shown in Fig. 2.6.

White light interferometry is a non-contact optical technique used to determine the profile of a surface under inspection. A white light interferometer typically contains a Mirau interferometer, illuminated by a tungsten halogen lamp. The two arms of the interferometer contain a reference surface and the sample. The interferometer setup is moved vertically with respect to the top surface of the sample, thereby, varying the optical length of this arm. The optical length of the reference arm is kept constant. The difference in optical lengths of the two arms introduce a phase difference between them, and interference fringes are observed. The interference fringes are imaged onto a detector, that uses those to calculate the size of the features on the sample surface. The features juxtaposed with the vertical positions at which the fringes were recorded generate the three-dimensional profile of the surface.

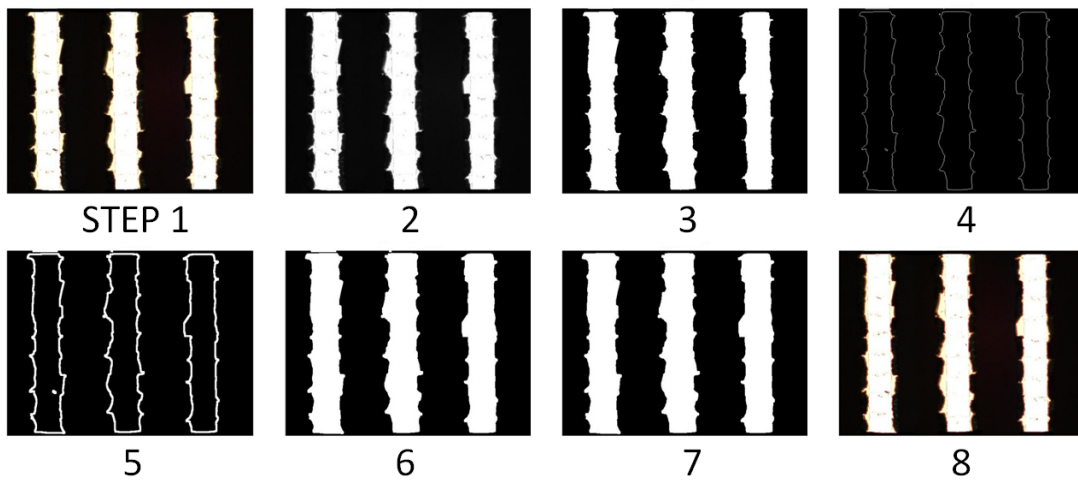


Figure 2.7: Examples of images obtained after each step during the image processing to calculate the edge roughness

2.5.3 Image acquisition, measurement and processing

The images are acquired through a (reflection and transmission) microscope (Olympus, BX51). The edge roughnesses and widths of the channels are obtained post processing of the images. An example of such measurements on a feature is shown in Fig. 2.10. A software code (written in *MATLAB*) processes the images in several steps, which are summarily shown in Fig. 2.7 and also enumerated below. The code is provided in Appendix 7.

1. Editing the image to encapsulate the channels within the dark background
2. Converting the image to gray scale
3. Converting the gray scale to binary with the pixel luminance threshold of 0.3
4. Detecting the edges and hence the objects (channels) within the image using Canny algorithm
5. Dilating the image to fill gaps in the edges
6. Filling the inside of the detected objects (channels)

7. Removing the objects attached to the boundary of the image
8. Outlining the boundary (detecting the edges) of the channels
9. Storing the coordinates of the individual edges one by one
10. Fitting a straight line through each of the edges
11. Calculating the perpendicular distance (d) of the points on the edge from the fitted line
12. Calculating the root mean square of the distance (also called R_{rms} or R_q)

The coordinates of the individual edges are stored one by one and a straight line is fitted through each of the edges using the least sum of squares fit. The perpendicular distance (d) of the points on the edge from the fitted line is used to calculate the root mean square of the distance (also called R_{rms} or R_q), which is the edge roughness. Channel width is the distance between two straight lines, fitted to the outermost edges of the channel.

2.6 Experimental procedures

2.6.1 Procedure for metal machining

Table 2.2: Levels of input parameters varied during micromachining metals

Factors	Values
Fluence (J/cm^2)	3, 4, 5
Number of pulses	1, 10, 20, 30
Ambient atmosphere	Air, helium, oxygen

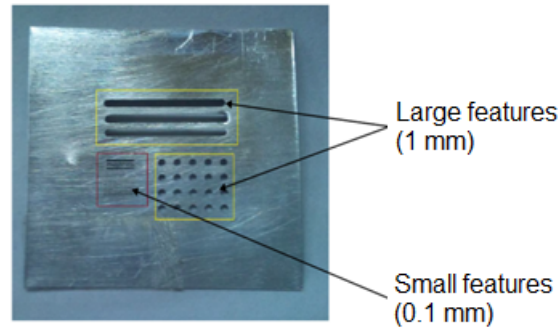


Figure 2.8: The photograph of the mask used for machining channels and holes. It contains features of lengthscales of 1 mm and 100 μm . After a demagnification of $0.1\times$, features of 100 μm and 10 μm are obtained on the workpiece.

In this study, channels and holes have been machined on stainless steel (SS) and beryllium copper (Alloy 25, BeCu) sheets at two characteristic dimensions - 100 μm and 10 μm . A 2 cm \times 2 cm binary mask, shown in Fig. 2.8 is used to fabricate the features. The mask has features of the characteristic dimensions of 1 mm and 100 μm . Figure 2.9 shows the scanning electron micrograph of one such set of features. These features have been machined at $3 \text{ J}/\text{cm}^2$ in air. Large and small channels and holes can be observed on the surface of SS. In the following sections, features on SS are further analyzed. Apart from machining under normal atmosphere, machining under oxygen and helium atmospheres have been carried out. These atmospheres have been provided by the flow of the gas (at the pressure of 2 bar) over the region of machining, through a thin pipe.

2.6.2 Procedure for polymer machining

The mask used in the study is shown in Fig. 2.8. The characterization of the machined workpieces was primarily conducted by a (reflection and transmission) microscope (Olympus, BX51). Optical white-light profilometry (Wyko NT1100) was utilized to characterize shallow and broken features that were difficult to characterize using the optical microscope.

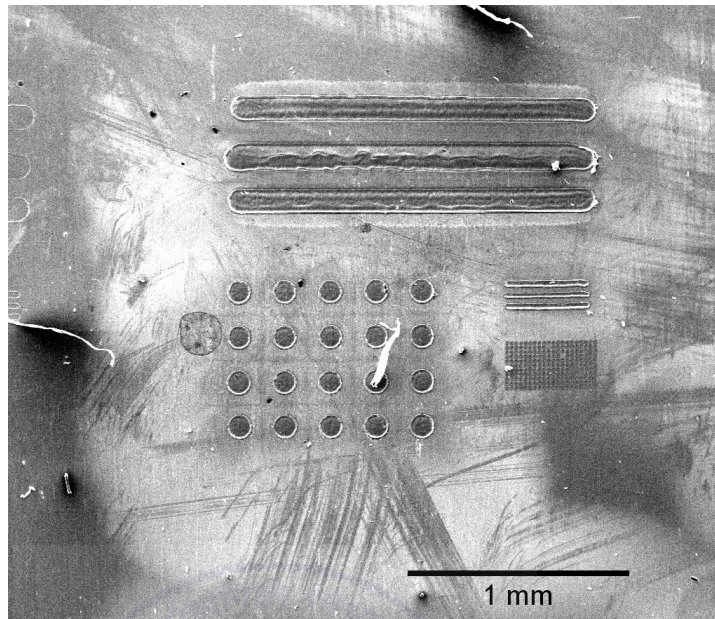


Figure 2.9: The scanning electron micrograph of a set of features machined on SS. The features shown have been machined at 3 J/cm^2 in air. The large channels and holes have the characteristic dimensions of $100 \mu\text{m}$, whereas the small channels and holes have the characteristic dimensions of $10 \mu\text{m}$.

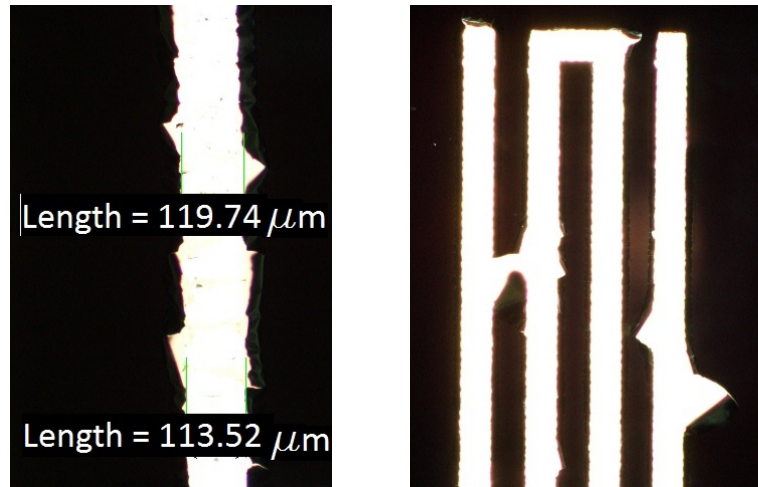
The substrate materials used for making channels are Kapton (polyimide, DuPont), PMMA (a-cast acrylic sheet, Asia Poly Industrial, Malaysia) and commercially available boPET (bi-axially oriented polyethylene terephthalate). Sheets of these materials were cleaned ultrasonically in ethanol and deionized water. This removes all dirt and contamination from the surface of the material. Note that even small amounts of dirt or oil will affect the absorption of the laser, and so also the quality of the feature produced. The machining parameters and their levels are mentioned in Table 2.3. The fluence values are chosen in the range in which the depth varies linearly with it. The mask used for machining had channels of two different widths ($100 \mu\text{m}$ and $10 \mu\text{m}$).

Table 2.3: Levels of input parameters varied during micromachining polymers

Parameters	Values
Fluence (J/cm^2)	3, 4, 5
Number of pulses	1, 10, 20, 30
Atmospheres	Air, Helium, Oxygen

2.6.3 Procedure for metal thin film machining

The substrate used is borosilicate glass (hereafter referred to as glass). Films of aluminum, chromium and gold are deposited by thermal evaporation on cleaned glass substrates. The thicknesses of metal films are 200 nm for aluminum and chromium films, and 40 nm for gold film. The thicknesses of the films have been determined during deposition using a quartz crystal monitor. Typical rms surface roughness of our films is about 5 nm. Thickness variation will not be larger than a few nanometers. On some of the metal films, 1 μm thick film of PVA (hereafter referred to as polymer, unless specified otherwise) is spin coated at 3000 rpm for 45 seconds followed by curing at 80°C for 45 seconds. The workpiece is kept on the XYZ-R micro-positioning stage and brought to the image plane of the mask. It is important to keep the workpiece at the image plane to machine sharp microfeatures [Dayal et al. (2013a)]. The micro channels are machined on the workpiece under varying conditions of fluence, spot overlap and pitch. A series of pulses falls on overlapping spots on the metal film to machine a continuous channel. The machined features are characterized regarding the edge roughness, channel width and integrity of boundary between adjacent channels. All observations are averaged over at least 5 values. These observations are then related to the machining parameters and inference is drawn on the range of parameters that give the



((a)) An example of a machined channel showing the measured width

((b)) The boundary between adjacent channels machined under identical conditions

Figure 2.10: Examples of $100 \mu\text{m}$ wide channels machined on 200 nm aluminum film

optimum feature quality in terms of low roughness and channel width and high integrity of the boundary.

Mask used for machining channels in metal thin films

The mask used in the study is shown in Fig. 2.11. The mask feature is demagnified twice using a mask projection method [Dayal et al. (2013a)], and a $100 \mu\text{m} \times 100 \mu\text{m}$ spot with

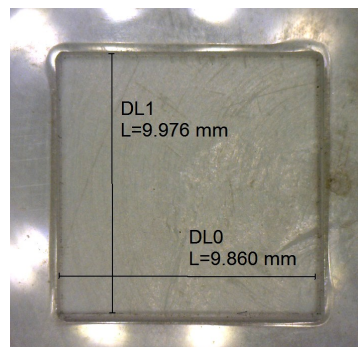


Figure 2.11: The binary mask, machined in acrylic, used in this study. The open area is 1 cm^2 .

Table 2.4: Levels of input parameters varied during machining straight channels

Factors	$-\alpha$	-1	0	+1	$+\alpha$
Fluence (J/cm^2)	0.6	0.9	1.3	1.7	2.0
Overlap (%)	6.3	20.0	40.0	60.0	73.6
Pitch (μm)	48	150	300	450	552

Table 2.5: Levels of input parameters varied during machining tilted channels

Factors	$-\alpha$	-1	0	+1	$+\alpha$
Fluence (J/cm^2)	0.6	0.9	1.3	1.7	2.0
Overlap (%)	6.3	20.0	40.0	60.0	73.6
Angle (degrees)	1.1	10.0	23.0	36.0	44.9

uniform irradiance across the spot is obtained on the workpiece.

Design of experiment

The experiments are designed using the Response Surface Methodology [Montgomery (2008)]. Three machining parameters are considered as input parameters during machining straight channels, namely, fluence, spot overlap (hereafter referred to as overlap) and pitch (inter-channel distance). For the case of tilted channels, angle of tilt of the channel is considered as the third parameter instead of pitch. Using the Central Composite Design [Montgomery (2008)], 20 sets of experiments are carried out using the value of $\alpha = 1.682$ for a rotatable design. The values of these parameters are tabulated in Table 2.4 for straight channels and

Table 2.5 for tilted channels. The machined features are analyzed for edge roughness and channel width, both of which are the measured outputs.

Procedure of statistical analysis

The statistical analysis allows to identify the effects of fluence and spot overlap on the outputs during machining. The observations (variation of measured outputs with the design parameters) are analyzed using ANOVA (Analysis of Variance). The confidence interval used is 95%, and low *p-values* (less than 0.01) and high *F-values* are obtained for the fitted models. This suggests high dependence of the measured outputs on the design parameters. Equations are fitted to the observe data, with independent factors up to third order, and interaction terms with individual factors having a maximum of second order. The equations are summarized in Appendix 6.21(c). All terms used in the model are significant, with *p-values* less than 0.01. The response surfaces are plotted using a commercial software Design Expert 9.0.

2.6.4 Procedure for machining micro lens arrays

The fabrication of micro lens array proceeds through generation of masks in two stages, followed by the fabrication of the lenses. The first stage mask used was a 30 mm × 30 mm piece of aluminum foil inside which the desired cross-sectional profile of the lenses was

Table 2.6: Levels of input parameters varied during machining the micro lens array

Pulse energy (mJ)	176
Pulse repetition rate (Hz)	5
Scanning speed (um/s)	8.3, 16.7, 25.0, 33.3

cut, at a scale of $100\times$. This mask was used to further machine the same profile, albeit at a 10 times smaller scale, on a polymer sheet. The work piece is an 8 mm thick piece of poly(methyl methacrylate) (also known as PMMA). The polymer mask was finally used to fabricate the lenses on the PMMA work piece. The work piece was kept on a micro-positioning XYZ stage, and scanned along the X and Y axes to generate the lens array.

The machining parameters used for the experiments are mentioned in Table 2.6. The pulse energy was fixed at 176 mJ and the pulse repetition rate was fixed at 5 Hz. A set of experiments were conducted by varying the scanning speed of the work piece. The variation in scanning speed causes a variation in the number of pulses falling at a particular spot, and thereby varies the depth to which the feature gets machined.

2.7 Sources of error in the experiments

It is pertinent to discuss the sources of error in experiments before discussing the results in detail. The sources of error are

- Pulse to pulse energy fluctuation within a range of 3%.
- Stainless steel sample has a randomly distributed roughness on the surface that causes fluctuations of light scattering from different parts of the same sample. This leads to subsequent fluctuation in the incident energy, which has not been determined for the present experiments. This effect is more important for highly reflecting metallic surfaces. Workpiece material inhomogeneity at the micro scale can be important, particularly for polymers and large grained materials.
- Laser beam is considered homogeneous and the inhomogeneity has been measured to be about 1% across the cross section.
- The pulse irradiation is carried out over different areas of the workpieces. Hence the

laser machine has been switched off while traversing the workpiece and the parameters changed before starting the irradiation again. The first pulse obtained after switching on the machine does not necessarily conform to the parameters set, and hence in order to stabilize the cavity several pulses are generated before irradiation is allowed to start. This ensures that pulses with stable energy value (within 3%) are obtained.

- The ablation depths for stainless steel were measured using an optical profilometer, with an error of less than 10 *nm*.
- Prior to machining, the workpiece has to be placed at the image plane of the mask. The depth of focus for 100 μm features being larger than the feature size, slight variation in the vertical positioning of the workpiece does not affect the focussing [Dayal et al. (2013a)]. In addition, these variations in positioning can be controlled to within a few micrometers owing to the use of micro stages.

Chapter 3

Excimer laser micromachining of metals and influence of ambient gas

Industrial lasers are mostly used for machining metals. Processes such as cutting, engraving, welding and texturing of metals and metal surfaces using various kinds of lasers are well established. In this context, it is important to understand interaction of nanosecond UV lasers with metals and the quality of the features thus produced, particularly in the context of machining micro features. A thermal ablation model is presented in this chapter to calculate the depths of ablation in metals. Computer simulations of this model are carried out to understand the ablation process at micrometer scales, when using nanosecond UV lasers. The fabrication and feature qualities of 100 μm channels and holes on a metal are discussed. A discussion on the effects of ambient environment on the machined features, in terms of the depths of ablation and the resolidified material, is provided.

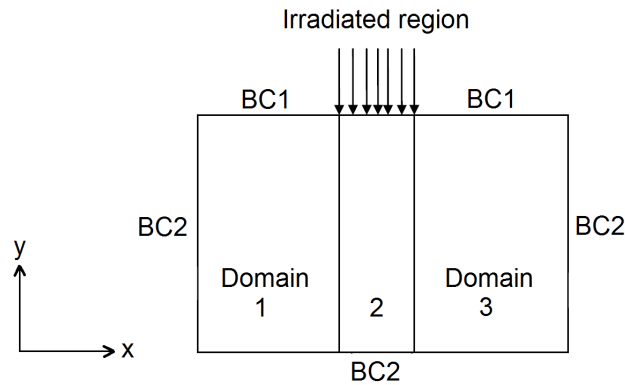


Figure 3.1: The geometrical domain of the model, with incident radiation and boundary conditions. The domain is divided into three sub-domains. The laser fluence falls on the middle domain (2). BC1 is convective and radiative cooling, whereas, BC2 is thermal insulation.

3.1 Numerical simulations of laser ablation of metals

3.1.1 A static thermal ablation model

Irradiation of a surface results in a part of the radiant energy being absorbed into the material and the remaining part being reflected from it, depending on the dielectric properties of the material at the wavelength of the irradiation. For an opaque material, the transmittance is zero (since no energy is transmitted through the material), hence the absorbed energy is equal to $(1 - R)$ times the total irradiated energy, where R is the surface reflectance. The intensity (I , defined as the average energy flux per unit time, averaged over the period of the wave) attenuates inside the material according to the Beer-Lambert law as

$$I(y) = I(0)e^{-\alpha y}, \quad (3.1)$$

where $I(y)$ is the intensity at depth y into the material and α is the linear absorption coefficient of the material. Both R and α , beside being specific to the material, depend on the wavelength of the radiation. Most of the energy is found to be absorbed in the top layers of

Table 3.1: Material properties used in the thermal ablation model. Specific heat capacity (C_p), thermal conductivity (κ), density (ρ), vaporization temperature (T_{vap}), linear absorption coefficient (α) and surface reflectance (R) are mentioned.

Material	$C_p(J/kgK)$	$\kappa(W/mK)$	$\rho(kg/m^3)$	$T_{vap}(K)$	$\alpha(m^{-1})$	R
Stainless steel	490	Varying with T	7800	3273	-	0.3
Air	1.005	0.0271	1.127	-	-	-

the material, called the skin depth, δ , which is expressed as

$$\delta = 2/\alpha. \quad (3.2)$$

From Eq. 3.2 it can be inferred that the absorbed radiant energy may be regarded to be purely absorbed on the surface for a very high value of α (typically for metals), and the energy travels further into the material mainly by thermal conduction [Leong (1999)]. The laser pulse duration is of the order of several nanoseconds, which is much greater than electron cooling time and lattice heating time. During the laser pulse, sufficient electron-phonon interaction leads to increased temperature in the material [Meijer (2004); Yao et al. (2005)]. Thus, laser ablation with nanosecond pulses can be simulated using the classical heat conduction theory [Mazumder and Steen (1980)]. The aspect ratio of a feature (holes and channels) is a critical parameter in small-scale fabrication field [Lim and Yoo (2011)] and hence a two-dimensional modeling of the laser beam (including its width) is performed.

Heat conduction in a material is defined by the transient energy transport equation

$$\rho C_p \frac{\partial T}{\partial t} + \nabla \cdot (-\kappa \nabla T) = Q, \quad (3.3)$$

where ρ is the density of the material, C_p is the specific heat capacity of the material at constant pressure, T is temperature, t is time, κ is the thermal conductivity of the material

and Q is the volumetric heat source (in Watt per unit volume) that takes into account the reflectance as well as the linear absorption coefficient. The heat source for the laser irradiance is defined as

$$Q(y) = (1 - R)I(0)\delta(y), \quad (3.4)$$

for a metal like steel. Here, $\delta(y)$ is the Dirac-delta function. The material is modeled as a rectangle 100 μm wide and 200 μm deep as shown in Figure 3.1. The geometry is divided into three domains along the width, with the top surface of the 10 μm wide middle domain being irradiated with laser energy. The irradiation is modeled as a surface heat flux for steel. The pulsed heat source has a pulse width of 20 ns. The material is considered isotropic and homogeneous and the ablation is modeled using the *birth and death* method. Whenever the temperature of a certain element exceeds the vaporization temperature of the material, the properties of that particular element are changed to that of air. This allows the heat to pass through that element with minimum interaction. Hence, material removal is simulated and only the elements having temperature below the vaporization temperature experience the heat. Convective, radiative and insulating boundary conditions are applied suitably. The properties used in the study are outlined in Table 3.1. For steel κ was taken to vary with temperature as [Bailey (21 June 2012)]

$$\kappa = 14.6 + 0.0127T. \quad (3.5)$$

The specific heat capacity of steel (a metal) remains fairly unaffected by temperature, and hence its variation has not been incorporated in this work. Absorptivity and surface reflectivity are the two optical parameters, the variations of which with temperature have not been studied in detail in the literature for sub-400 nm wavelengths. UV surface reflectivity is generally not available for all materials, and such studies have not been widely conducted at high temperatures. Additionally, the variation of these two parameters are masked by the plasma

shielding that exercises a far greater effect on the amount of radiation reaching the material surface.

3.1.2 A dynamic thermal ablation model

A dynamic thermal ablation model is proposed with the major difference being the movement of the heat source, Q , with the melt surface, along the y axis. The domain is a $2 \text{ mm} \times 2 \text{ mm}$ square, divided into two halves, along the y direction. The model incorporates element switching, whenever the density of an element falls below the value of 500 kg/m^3 . The height of the region, r_0 , at any position along the x axis, is calculated by integrating, along the y axis, the condition $\rho < 500 \text{ kg/m}^3$. The volumetric heat source, Q , is applied to the middle region of the bottom half, similar to the setup shown in the Fig. 3.1, with all boundary conditions remaining the same. If F is the laser fluence, then the heat source is defined as,

$$Q(y) = \alpha F e^{-\alpha(-r_0-y)}, \quad (3.6)$$

if $y \leq -r_0$. This expression makes the heat source disappear from the region that has transitioned into the liquid, and the heat source is assumed to be always incident on the solid surface. The material properties are tabulated in Table 3.2, and the temperature dependent properties are shown in Fig. 3.2. The variations of properties with temperature are second order continuous. The domain is meshed with a mapped mesh, with elements cut diagonally, to generate triangular elements.

The model was numerically simulated, and the temperature variation, and consequent element switching, were observed. The results of the simulations are briefly discussed in the Section 3.2.1.

Table 3.2: Material properties used in the dynamic thermal ablation model. Melting temperature (T_{melt}), vaporization temperature (T_{vap}), specific heat capacity (C_p), thermal conductivity (κ), density (ρ), dynamic viscosity (μ), linear absorption coefficient (α) and enthalpies of fusion and vaporization (ΔH_f & ΔH_v) are mentioned.

Properties	Values
$T_{melt}, T_{vap}(K)$	500, 2500
$C_p(J/kgK)$	550 (liquid and vapor), 895.2 (solid). Refer Fig. 3.2(a).
$\kappa(W/mK)$	160 (solid), 110.9 (liquid), 0.03 (vapor). Refer Fig. 3.2(b).
$\rho(kg/m^3)$	2700 (solid), 1000 (liquid), 10 (vapor). Refer Fig. 3.2(c).
$\mu(Pa \cdot s)$	1000 (solid), 2.8×10^{-4} (liquid), 2.8×10^{-5} (vapor). Refer Fig. 3.2(d).
$\alpha(m^{-1})$	1.43×10^8
$\Delta H_f, \Delta H_v (kJ/kg)$	399, 10530

3.1.3 A dynamic thermal ablation model with fluid flow

In order to realistically realize the machined surfaces produced after laser micromachining, it is necessary to consider the flow of the molten metal, under the action of recoil pressure.

The flow is considered as compressible and modeled using the Navier-Stokes equation,

$$\frac{\rho \partial \mathbf{u}}{\partial t} + \rho(\mathbf{u} \cdot \nabla) \mathbf{u} = \nabla \cdot [-p \mathbf{I} + \mu \{ \nabla \mathbf{u} + (\nabla \mathbf{u})^T \}] - \frac{2}{3} \mu (\nabla \cdot \mathbf{u}) \mathbf{I} + \mathbf{F}, \quad (3.7)$$

and the mass continuity equation,

$$\frac{\partial \rho}{\partial t} + \nabla \cdot (\rho \mathbf{u}) = 0. \quad (3.8)$$

Here, \mathbf{u} is the velocity of the fluid and \mathbf{I} is the identity matrix. The volume force, \mathbf{F} , is equal to ρg , acting in the negative y direction. Under the assumptions that the incident

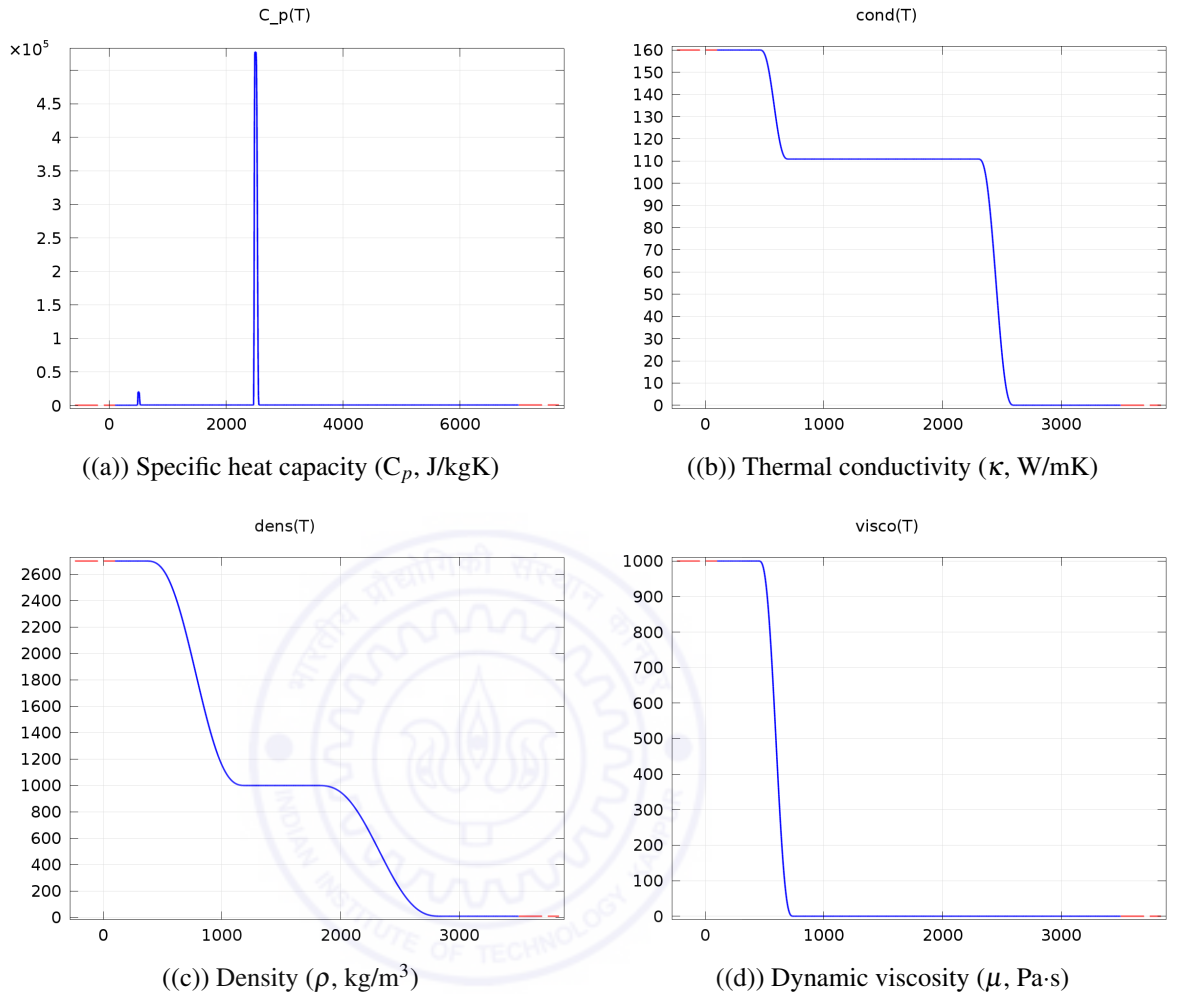


Figure 3.2: Temperature dependent properties of the material used in the dynamic thermal ablation model. The horizontal axes show the temperature in Kelvin.

radiation has a temporally constant intensity, that the vapor is an ideal monoatomic gas that does not absorb the incoming radiation, and that the atoms in the vapor follow the Maxwell speed distribution, the recoil pressure, p_{recoil} , can be defined as [Nath et al. (2010)]

$$p_{recoil} = \frac{1.69F}{\sqrt{\Delta H_v}} \frac{b}{1 + 2.2b^2}, \quad (3.9)$$

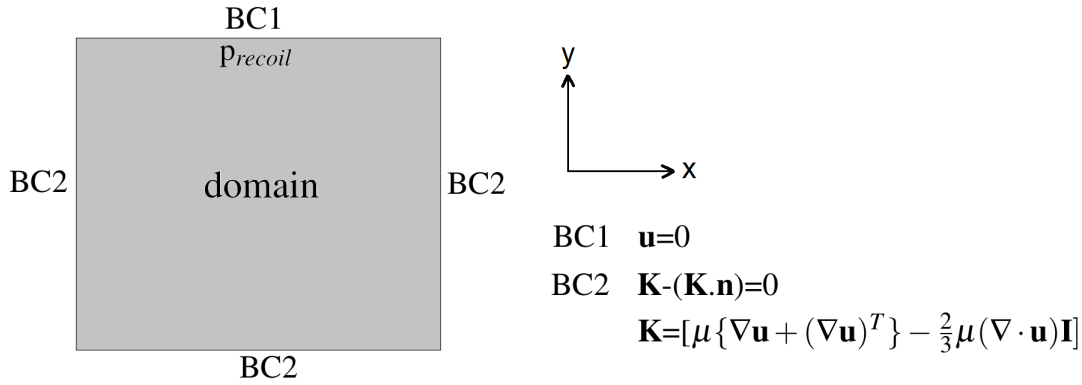


Figure 3.3: A schematic diagram of the domain along with the boundary conditions for the fluid flow. \mathbf{n} is the unit vector normal to the boundary.

where,

$$b^2 = \frac{\kappa T_s}{m_v \Delta H_v}. \quad (3.10)$$

In the equation above, T_s and m_v are the surface temperature and the molecular mass of the vapor, respectively. The model consists of a rectangular domain, at the center of which the volumetric heat source is applied. The melting and vaporization of the material is modeled by varying the material properties with temperature. In addition to the variations in density, specific heat capacity and the thermal conductivity of the material, the dynamic viscosity of the material is also varied in this case. The recoil pressure acts on the top surface of the domain, wherever the temperature of the top surface exceeds $T_{vap} - 50$ K. The boundary condition on the top wall is that of no slip, whereas slip is allowed on all other walls. The boundary conditions are schematically shown in Fig. 3.3. The domain is meshed with triangular elements. The mesh is allowed to deform along with the flow of the material. The mesh deformation is arrested on the side and bottom surfaces of the domain. The top surface follows the velocity of the fluid.

3.2 Results and discussion

3.2.1 Simulations of ablation models

The models discussed above have been implemented in the finite element analysis software, COMSOL Multiphysics. The simulated results for the depths of ablation and the temperature profile from the dynamic ablation model with element switching are shown in Figures 3.4 and 3.5.

The results presented in Figures 3.4 show that the temperature rise within the first few nanoseconds. The reasons for the unrealistic temperature rise is the continuous heating of the material in the absence of flow. Hence it is necessary to incorporate the flow of the molten material in order to realistically model the physics of the process.

The dynamic ablation model with fluid flow was first computed over large time steps (of 0.1 s duration) and domain size, in order to set right the model parameters. The results from the simulations of this model are presented in Figures 3.6. Since the model does not capture the timescale and lengthscale of the laser micromachining process, the absolute values of the temperatures and velocities are not of interest. However, it may be observed from the figure, that the model is able to capture the physics of the process, showing the melted regions and the melt flow, under the action of the recoil pressure. The ridges formed on the sides of the machined regions are clearly visible.

The dynamic ablation model with fluid flow is further refined to consider the time and length scales of the micromachining process. The domain is, hence, resized to a rectangle 700 μm wide and 500 μm high. The heat source is made incident on the 200 nm wide region in the center of the domain. Since the heat flux of a nanosecond pulsed UV laser is very large (of the order of 10^{12} W/m^2), the simulation is carried out with time steps of 0.01 ns. The domain is meshed with 10000 rectangular elements, with finer elements at the center and top of the domain. The results from the simulation are shown in Fig. 3.7. The top surface

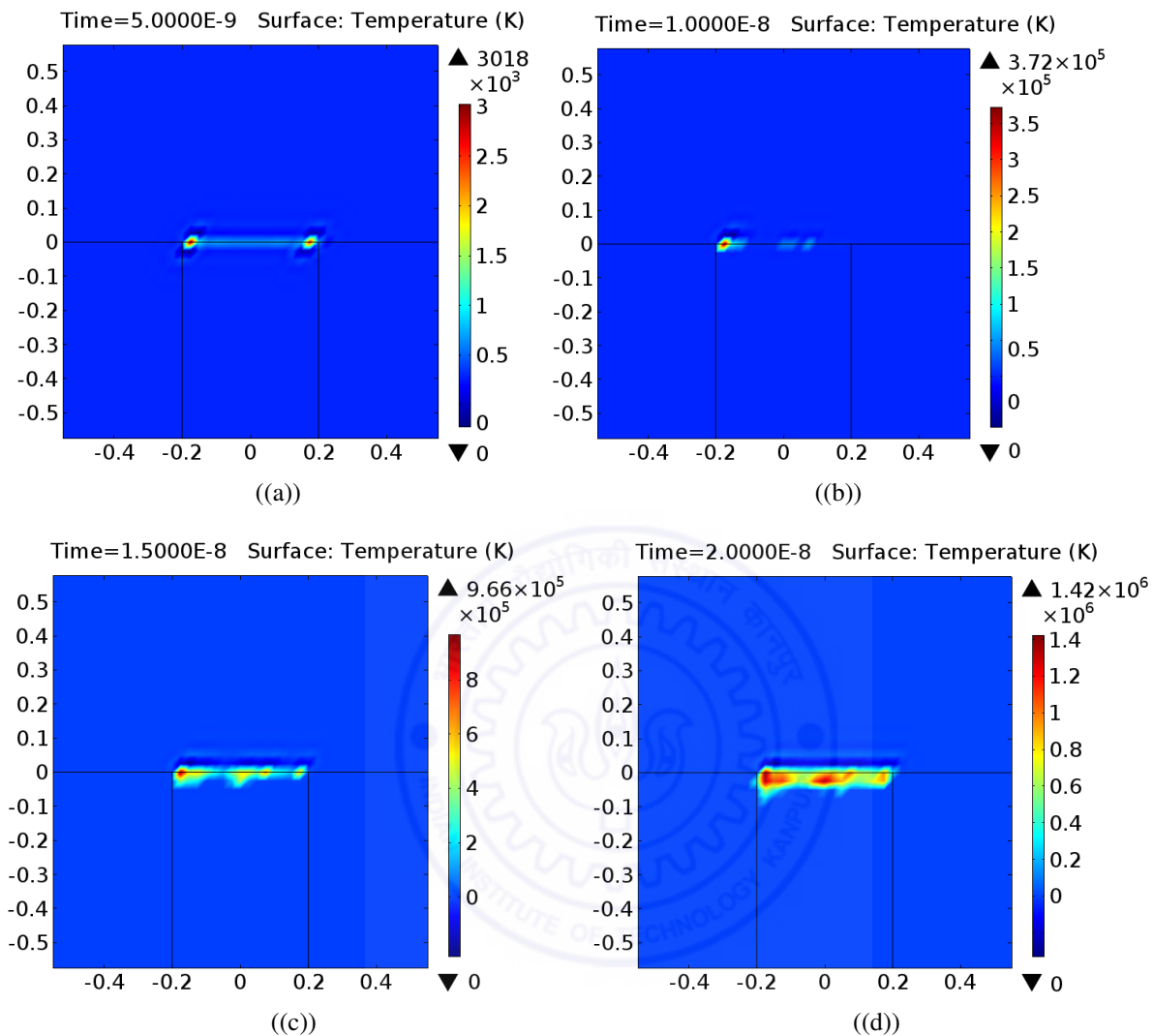


Figure 3.4: Temperature plots of the domain at various times within the 20 ns pulse duration. The model incorporates a moving heat source and element *birth and death* to capture the vaporization of the material.

of the domain is highly unstable, with huge pressure buildup and high surface deformation velocity. From the velocities calculated, it is estimated that the Reynolds number is about 500, indicating that while the flow is more or less laminar, there could be some instabilities. The velocity of 350 m/s is close to the acoustic wave speed in air, and the Mach number (defined as the ratio of the flow velocity to the local acoustic wave velocity) is close to 1.1,

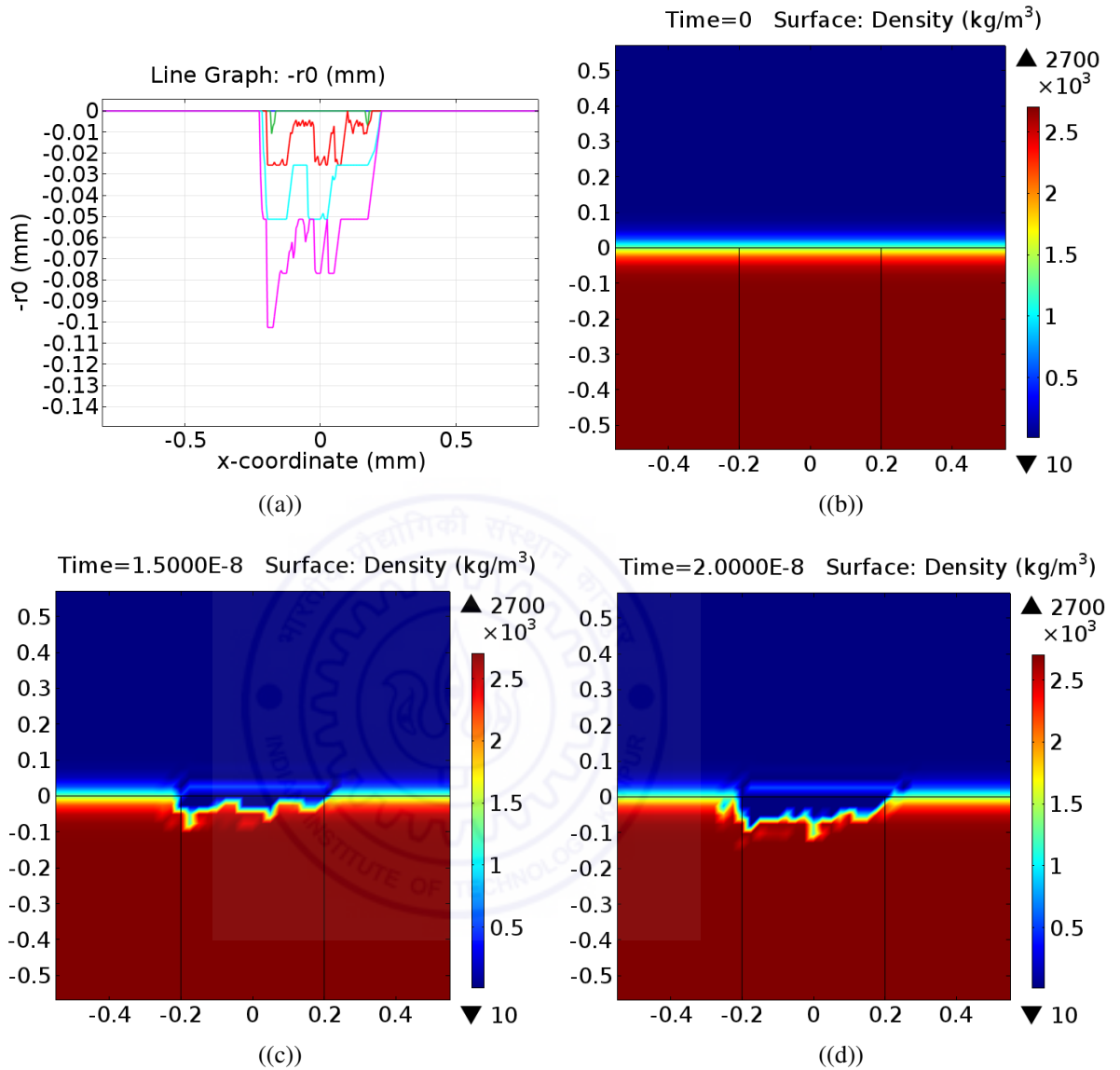


Figure 3.5: Density plots of the domain at various times within the 20 ns pulse duration. The model incorporates a moving heat source and element *birth and death* to capture the vaporization of the material. The green, red, cyan and magenta lines in (a) represent the surface profiles at 5, 10, 15 and 20 ns, respectively.

indicating that the system is in the region of a shock wave instability. The instabilities at the nanosecond time scale and the nanometer lengthscale required advanced stabilization techniques to ensure convergence. This is a problem that is open to future efforts.

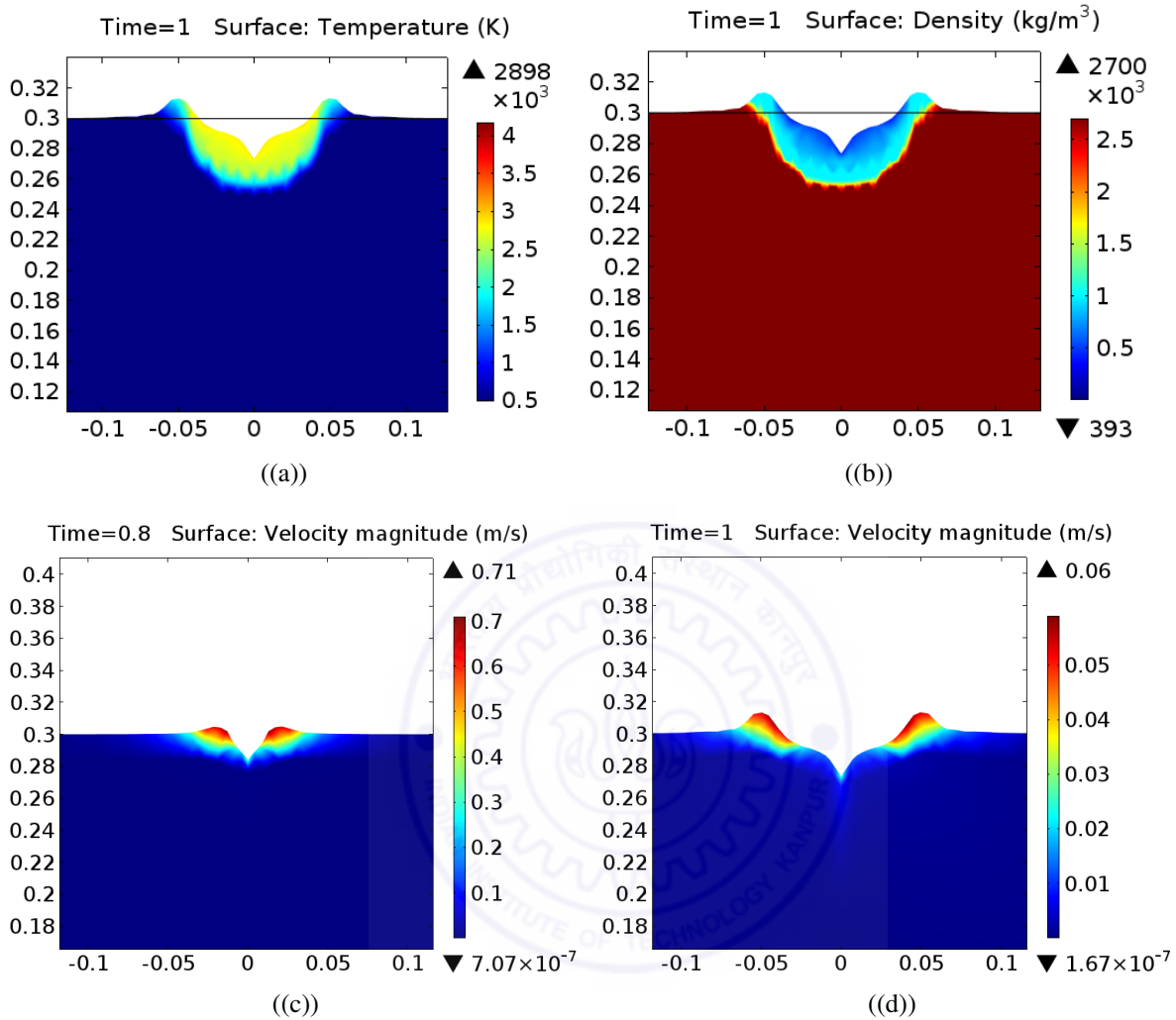


Figure 3.6: Simulation results from the dynamic thermal ablation model with fluid flow, with large time steps and over a large domain.

3.2.2 Analysis of 100 μm wide channels in SS

Here we discuss the observations of machining 100 μm wide channels and 100 μm diameter blind holes (referred to as holes henceforth) on stainless steel (SS). Typical results obtained from experiments on SS are shown in Figures 3.8. The machining in stainless steel is predominantly pyrolytic (due to thermal ablation or melt-vaporization), and hence sharp channels are not observed. The channel boundaries tend to deform during the melt-

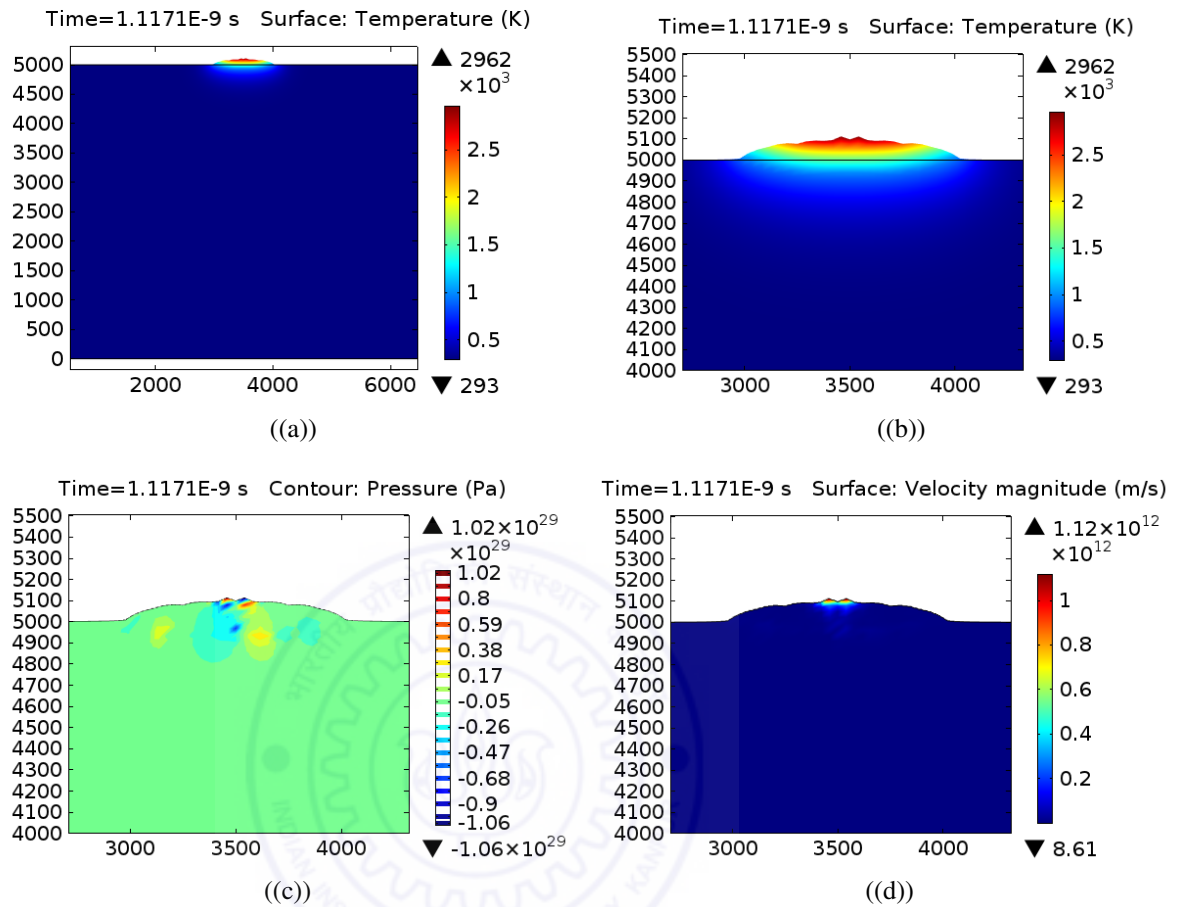
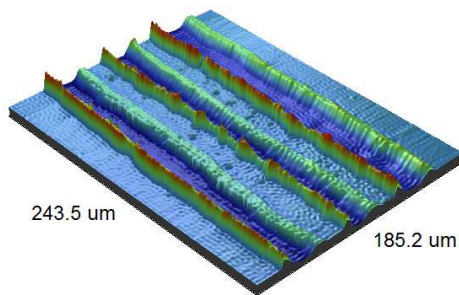
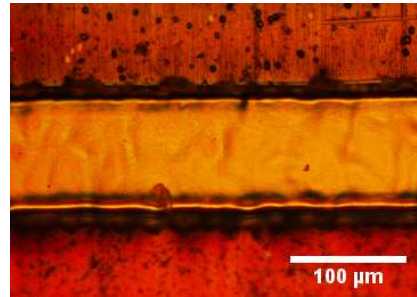


Figure 3.7: Simulation results from the dynamic thermal ablation model with fluid flow, with 0.01 ns time steps and over a small domain. The laser fluence used is $6.25 \times 10^{12} \text{ W/m}^2$.

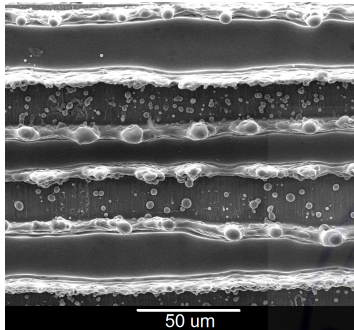
resolidification process leading to irregular boundaries and an uneven bottom surface. Figure 3.8(a) shows the ridges formed on the boundaries. Since the nanosecond pulses of laser deliver huge power to the surface of the metal, the metal is immediately liquefied, creating a pressure wave. This pressure wave throws out the molten material. A lot of this molten material redeposits on the surface of the metal far from the machined zone. The molten material that solidifies at the edges of the channel while getting splashed forms ridges along the edges. Figure 3.8(b) shows the micrograph of a channel with a boundary roughness of $1.3 \mu\text{m}$. It can be seen from the bottom surface profile of the channel (Figure 3.8(d)) that the steel



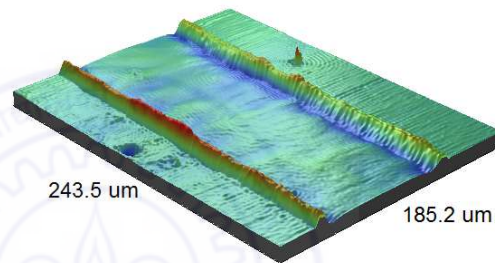
((a)) An optical profilograph of channels in steel, showing distorted edges and ridges at the boundaries



((b)) An optical micrograph of a channel in steel, showing the boundaries. The roughness of the boundary is $1.3 \mu m$.



((c)) A scanning electron micrograph of channels in steel showing deposition along the boundaries



((d)) An optical profilograph of a channel in steel, showing a smooth and bumpy surface after resolidification of the melt in the machined zone

Figure 3.8: Typical results for micro channels machined in stainless steel

melted and flowed before resolidifying. Figure 3.9 shows the scanning electron micrographs of channels machined at various conditions with 30 pulses. The figures on the top row have been machined in air at fluences of 3, 4 and $5 J/cm^2$, respectively. We can observe that at the lowest fluence, there is striking evidence of melt flow along the center of the channels. At higher fluences, redeposition on the side walls of the channels is observed. The redeposition is caused by resolidification of molten material while it is getting ejected. The channels in the middle row have been machined under helium atmosphere. The channels in this case have cleaner boundaries, which suggests reduced redeposition along the edges and effective flushing. The absence of any reactive gas in helium atmosphere prohibits explosive reactions of the melt and vapor molecules, thereby generating much smoother surfaces and edges. The

channels in the bottom row have been machined under oxygen atmosphere. These can be observed to have sharp boundaries and, as we shall see, deeper machining.

Cross-sectional profiles, along with the 3D surface profiles of some of the channels, are shown in Fig. 3.10. The cross-sectional profiles show that maximum resolidification

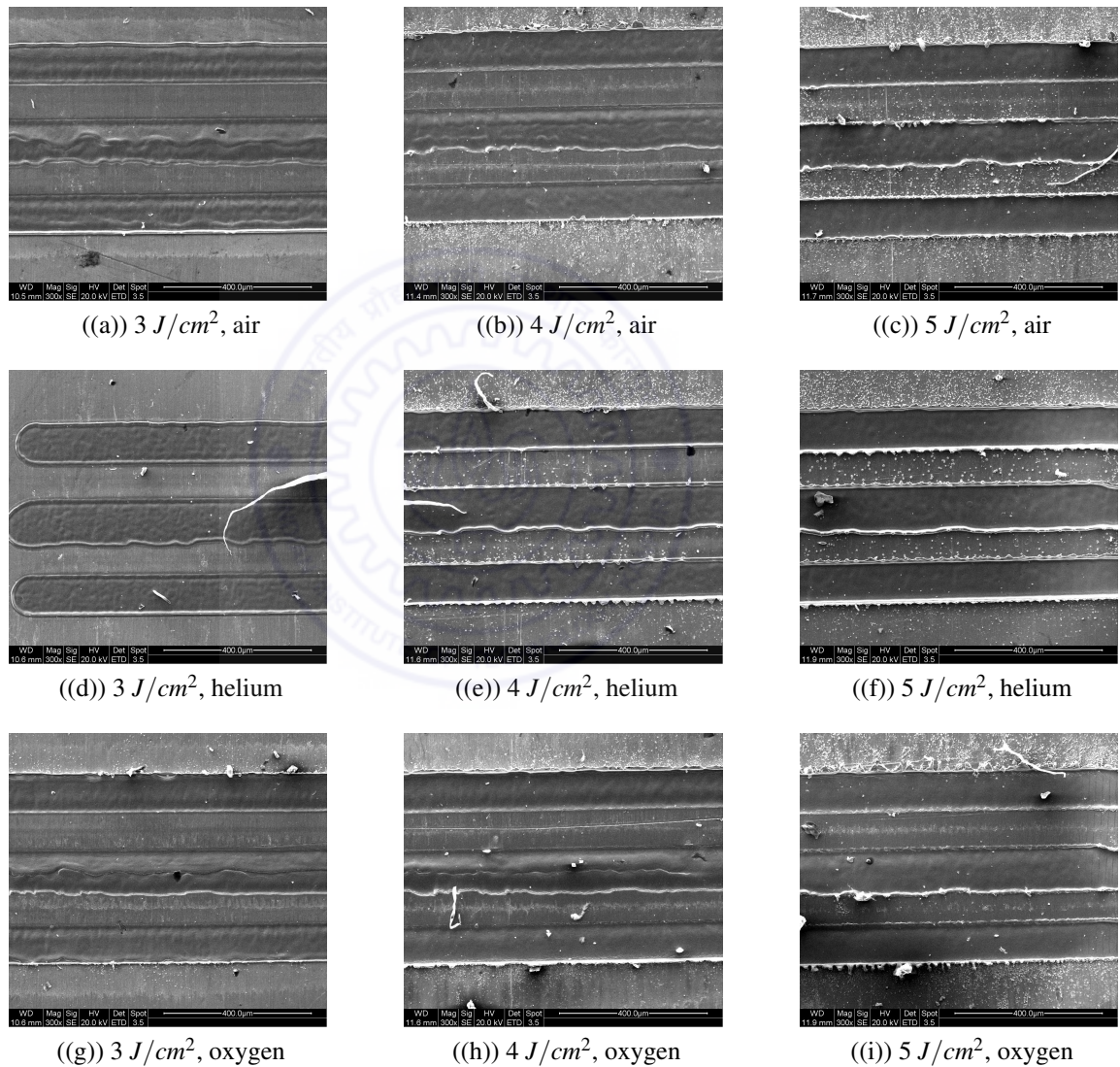


Figure 3.9: The scanning electron micrographs of $100 \mu\text{m}$ wide channels machined in SS. From the top row to the bottom, the channels have been machined in air, helium and oxygen, respectively. From the left column to the right, the channels have been machined at 3, 4, 5 J/cm^2 , respectively. All channels have been machined with 30 pulses.

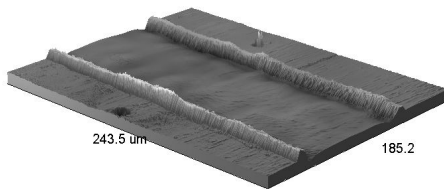
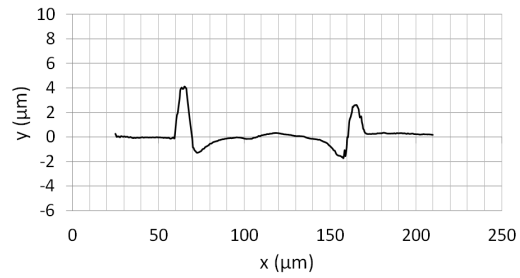
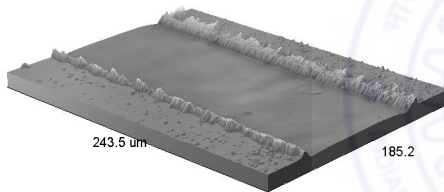
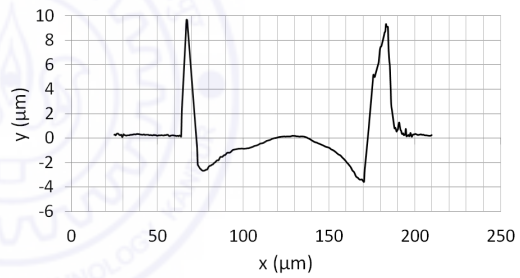
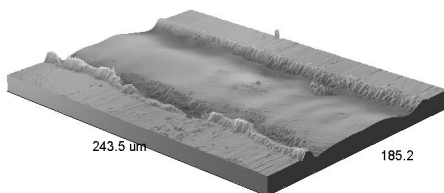
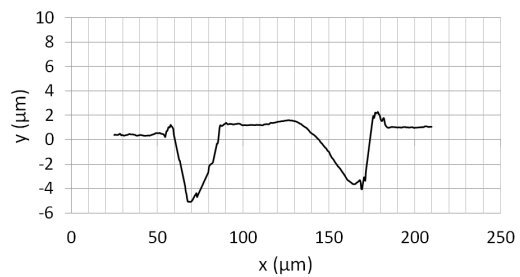
((a)) $5 J/cm^2$, air((b)) $5 J/cm^2$, air((c)) $5 J/cm^2$, helium((d)) $5 J/cm^2$, helium((e)) $5 J/cm^2$, oxygen((f)) $5 J/cm^2$, oxygen

Figure 3.10: The 3D and cross-sectional profiles of $100 \mu\text{m}$ wide channels machined in SS. From the top row to the bottom, the channels have been machined in air, helium and oxygen, respectively, all at $5 J/cm^2$ and with 30 pulses.

Table 3.3: Thermal properties of three gases under which laser micromachining has been carried out

Gas	Specific heat capacity, C_p (J/kgK)	Thermal conductivity, κ (W/mK)
Air	1.005	0.0271
Helium	5.188	0.145
Oxygen	0.92	0.025

happens while machining in helium atmosphere, whereas machining under oxygen generates negligible resolidification along the walls. Helium gas is widely used as a cooling agent, due to its high specific heat capacity and thermal conductivity (refer Table 3.3). Hence the material, while getting splashed out of the surface, experiences a quenching effect due to Helium, and resolidifies to give high ridges. It is inferred that the oxygen content of the atmosphere plays a direct role in oxidizing (burning) the resolidified wall, while it is getting formed. While the molten material is getting ejected, it has increased contact with oxygen molecules in the ambient atmosphere. This leads to quick oxidation and quicker rise in temperature, that does not allow the molten material to solidify. Instead, it either vaporizes or gets scattered around the wall.

Figure 3.11 shows the comparison between the experimentally measured depth with that numerically simulated (by considering the thermal ablation model only) for stainless steel. Figure 3.11(a) shows the variation of depth (μm) with the number of pulses. From the figure it is observed that as the energy per pulse increases, the depth increases. It is also observed that the rate of increase of depth increases with increase in the number of pulses, a trend reported by some researchers earlier [Semerok et al. (1999); Bulgakova and Bulgakov (2001); Byskov-Nielsen (2010)]. Aspect ratio follows a similar trend as depth, the reason being that

laser machining is a directional machining process (here the machining is in the downward direction) and hence the increase in width of the feature is negligible when compared to the increase in height. Additionally, despite having a higher thermal conductivity as compared to, e.g., PMMA, the depth of ablation in steel is small (up to a maximum of $5 \mu\text{m}$ in our case) and there is no observable increase in width, if any, over this small depth of machining. According to simulations performed by Lim and Yoo (2011), laser ablation per pulse for metals increases very rapidly (with a slope of almost 90°) till 10 J/cm^2 . Since, in this study, the fluence ranges from 3 J/cm^2 to 6 J/cm^2 , for a slight increase in fluence, we observe a large increase in depth per pulse (ablation rate). The slope of this graph gives the average depth per pulse (for the particular pulse energy) which, in other words, is the ablation rate. The ablation rate, which is typically between $0.1 \mu\text{m}$ and $0.5 \mu\text{m}$ per pulse, is observed to increase with pulse energy. The low ablation rate is attributed to low penetration depth of the laser in the metal, rendering the laser-metal interaction to be mostly a surface phenomenon.

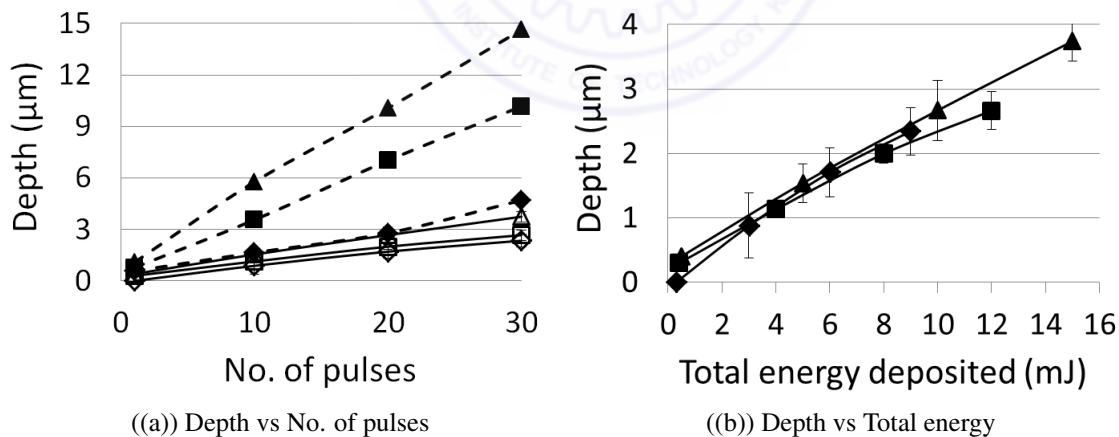


Figure 3.11: Comparison of experimental (solid lines) and simulated (dashed lines) results from micromachining stainless steel (left) and the variation of ablation depth with the total energy delivered to the workpiece (right). The lines are a guide to the eye only. The symbols \blacklozenge , \blacksquare and \blacktriangle represent fluences of 3, 4 and 5 J/cm^2 , respectively. The error bars show the standard errors. Where not visible, the error bars are smaller than the size of the symbols.

Higher energy pulses deliver more power, and hence heat, to the surface of steel. This causes greater amount of melting of steel and hence greater ablation. This observation agrees well with the trends reported by Bulgakova and Bulgakov (2001) and Byskov-Nielsen (2010). Figure 3.11(b) shows the variation of depth (μm) with the total energy (mJ) deposited per pulse. For a particular amount of total energy deposited on the material, different depths are obtained for different energy (energy per pulse) levels. This means that large number of low energy (energy per pulse) pulses generate lesser depth when compared to small number of high energy (energy per pulse) pulses for the same total energy deposited on the material. In other words, if we define ablation efficiency as the depth ablated per unit energy of the pulse, then high energy pulses are more efficient than low energy pulses. Knowing that since the laser delivers energy to the metal in the form of heat and metals are capable of conducting this heat away from the heat source, it can be argued that a portion of the incident energy is lost due to conduction. The heat conducted away is a fraction of the incident energy and this fraction varies inversely with the incident energy. The remaining portion of the heat results in melting and vaporization of the metal. Since the remaining portion is more in case of higher energy pulses compared to that for lower energy pulses, higher energy pulses have a higher ablation efficiency. This observation is further explained below mathematically.

Let us assume two cases of laser irradiation, one with a low energy pulse (p_1) and the other with a high energy pulse (p_2). Hence, $p_1 < p_2$. Let us further assume that after reflective losses from the surface, these pulses deliver e_1 and e_2 amounts of energy, respectively, to the surface of steel in the form of heat. Hence, $e_1 < e_2$, where $e_1 = (1 - R)p_1$ and $e_2 = (1 - R)p_2$. Here, R is the reflectivity of the surface.

Assuming both pulses have sufficient energy to ablate the material, the maximum temperature that will be reached in the material will be T_{vap} , the vaporization temperature of the metal. Hence the temperature gradient will be the same in both cases of irradiation. Considering that the melt pool will be smaller in the first case (low energy pulse) and larger in

the second case (high energy pulse), there will be comparatively higher solid-melt interface area in the second case. It is important to note though, that the solid-melt interface areas will not be significantly different in the two cases, because the laser-metal interaction is mostly a surface phenomenon. These arguments lead to the situation in which, in both cases of irradiation, heat has to be conducted through the same temperature gradient and through similar cross-sectional areas. Assuming that the amount of heat lost due to conduction is h_L , the portions of heat that remain (for melting the metal) in the two cases, respectively, are

$$h_1 = e_1 - h_L, \quad (3.11)$$

and

$$h_2 = e_2 - h_L. \quad (3.12)$$

If the remaining portion of heat be expressed as a fraction (f_1 and f_2) of the incident energy, then

$$f_1 = \frac{h_1}{p_1} = (1 - R) \frac{h_1}{e_1} = (1 - R) \left(1 - \frac{h_L}{e_1}\right), \quad (3.13)$$

and

$$f_2 = \frac{h_2}{p_2} = (1 - R) \frac{h_2}{e_2} = (1 - R) \left(1 - \frac{h_L}{e_2}\right). \quad (3.14)$$

Since $e_1 < e_2$, it follows from equations 3.13 and 3.14 that $f_1 < f_2$. Hence, a lesser fraction of incident energy is used to heat up the material for lower energy pulses (case 1) compared to that for higher energy pulses (case 2). Hence the ablation efficiency of lower energy pulses is lesser to that of higher energy pulses. This holds true for all cases of pyrolytic ablation.

It can be observed from Figure 3.11 that the simulation over-predicts the results when compared with experimental observations. The ablation depth is over-predicted by about

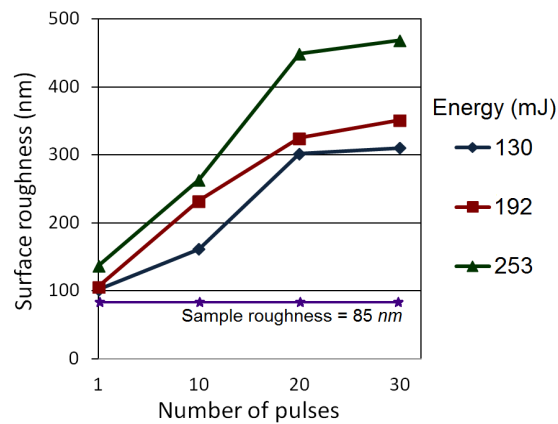


Figure 3.12: Surface roughness (rms, measured in nm) of the bottom of the channels machined in stainless steel for various pulse energies

$5 \mu m$ for the entire range of energy values. This is due to the fact that, firstly, no losses have been considered in the simulation and stainless steel has been modeled as an ideal homogeneous and isotropic material, without any defects. Secondly, plasma shielding has not been incorporated in the simulation. During laser ablation, a plume or cloud of plasma, from the ablated material, is formed above the laser material interaction zone. This plasma cloud absorbs the energy from the tail of the laser pulse and the subsequent irradiation and hence the energy reaching the material can be reduced. This decreases the ablation rate and a smaller depth is obtained for every incoming pulse [Jensen (2004); Leong (1999); Dan and Duan-Ming (2008)].

Measurements of surface roughness of channels are carried out and depicted in Figure 3.12. The surface roughness of the sample was 85 nm to start with. The surface roughness is observed to increase with the number of pulses, indicating that each pulse causes a turbulence in the melt pool formed. The melt pool cools rapidly, solidifying before the surface can even out, and this causes the turbulent surface texture to be retained. It is also observed from the figure, and understandably so, that higher energy pulses lead to higher surface roughness caused due to greater turbulence in the melt pool. Although higher energy pulses lead to a

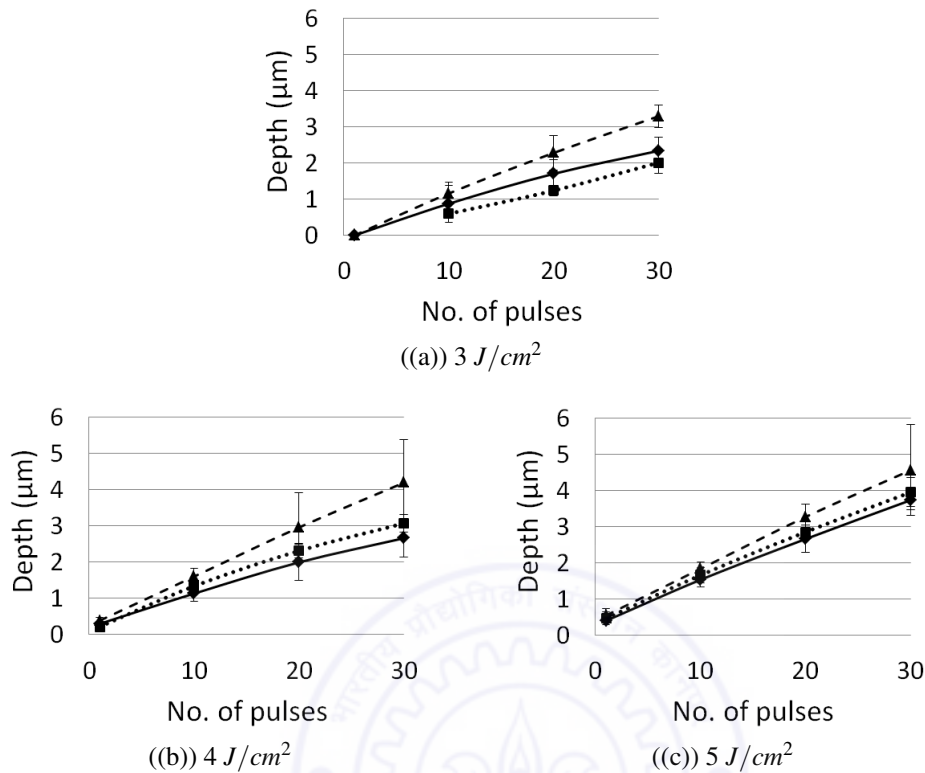


Figure 3.13: The ablation depths of $100 \mu\text{m}$ wide channels machined in SS as functions of the number of pulses, at fluences of 3, 4 and 5 J/cm^2 , from left to right. In each of the figures, the solid, dotted and dashed lines represent atmospheres of air, helium and oxygen, respectively. The error bars show the standard errors. Where not visible, the error bars are smaller than the size of the symbols.

larger melt pool, the feature sizes being in the micrometer domain do not allow gravity to affect the flow. The surface roughness appears to saturate with larger number of pulses as seen in the figure.

Figure 3.13 shows the plots of depth of channels plotted against the number of pulses for three values of fluence and three different atmospheres. It can be observed from all the cases that the depth increases linearly with increasing number of pulses. The depth increases with the fluence as well. Each of the graphs show the depth obtained post machining under air, helium and oxygen atmospheres. At the lowest fluence of 3 J/cm^2 , the machining under air generates more depth compared to that in helium. At low fluences, small amount of

material is ejected, and a comparatively weaker plasma is formed. Hence flushing is not required to help eject the vaporized and molten material. Additionally, use of assist gas has been observed to decrease the speed of ejection of material [Rodden et al. (2001)]. It is the oxygen content of the atmosphere that affects the amount of material vaporized and removed. Since there is no oxygen in helium atmosphere, least depth, amongst the three atmospheres, is observed in this case. The maximum depth observed at $3 J/cm^2$, with 30 pulses, is $3.3 \mu m$.

At larger fluences, such as in the cases shown in Fig. 3.13(b) and 3.13(c), a strong plasma plume is formed, which necessarily requires to be deflected away from the irradiation zone in order for the underlying surface to continue getting irradiated. In the presence of flushing, the pressure of the assist gas supplements the recoil pressure in material ejection [Ng et al. (2006)]. In the absence of flushing, the underlying surface is neither exposed to the laser beam, nor to oxygen. This greatly inhibits ejection of material, whether molten or vaporized. Since no flushing was done in air, least depth is observed in this case. Hence at high fluences, machining under helium, accompanied by flushing, generates more depth compared to that in air, without flushing. The maximum depths observed, at 4 and $5 J/cm^2$, with 30 pulses, are 4.2 and $4.6 \mu m$, respectively.

In the case of machining under oxygen, under elevated temperatures, the gas reacts exothermically with the elements in SS and BeCu [Ng et al. (2006)]. The heat of oxidation further raises the temperature of the melt surface and enhances machining by faster melting and vaporization. The greater the amount of oxygen, the more effective the ablation gets. Hence, the greatest depth is observed in the case of machining under oxygen due to 100% oxygen content as well as flushing. It can be inferred from the above mentioned observations that the use of assist gas has three effects on the pyrolytic ablation process. Firstly, its pressure supplements the recoil pressure. Secondly, the assist gas, if it reacts exothermically with the material, tends to increase the temperature of the irradiated zone, thereby increasing

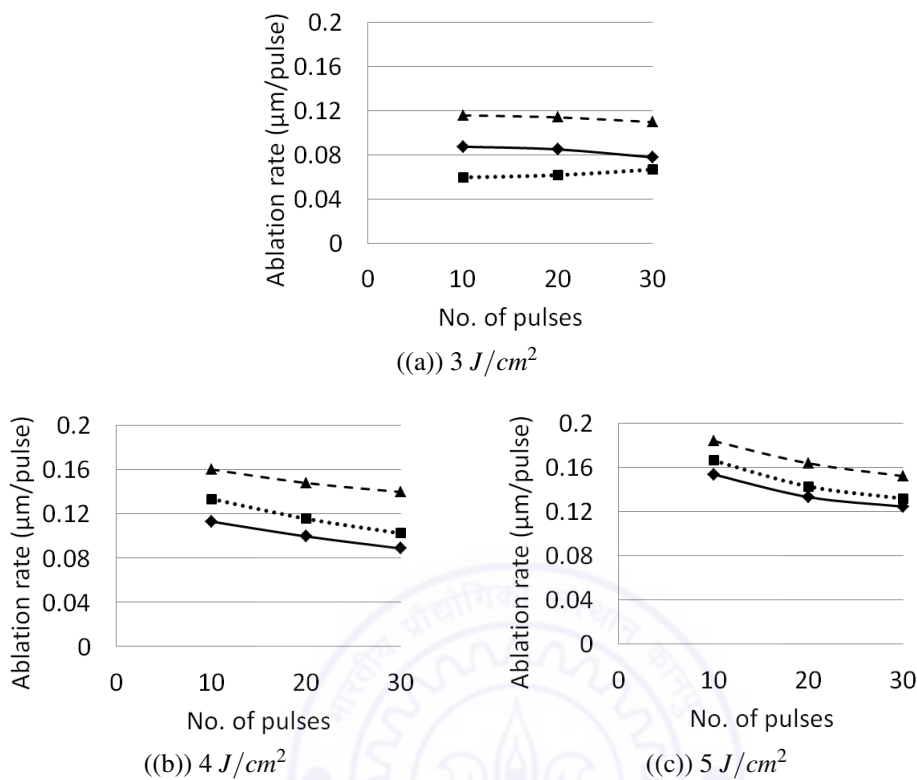


Figure 3.14: The ablation rates of $100 \mu\text{m}$ wide channels machined in SS as functions of the number of pulses, at fluences of 3, 4 and $5 \text{ J}/\text{cm}^2$, from left to right. In each of the figures, the solid, dotted and dashed lines represent atmospheres of air, helium and oxygen, respectively.

the rate of ablation. Thirdly, the assist gas hinders the ejection of material to some extent. The hindering of material ejection and oxygen content of the assist gas are dominant at lower fluences. At higher fluences, flushing aids the melt in ejection, dominating over other effects. Notice that at higher fluences (such as the one in Fig. 3.13(c)), the depths obtained are closer to each other for different atmospheres, with other parameters held constant, compared to those obtained at lower fluences (such as the one in Fig. 3.13(a)).

Figure 3.14 shows the ablation rates for the various cases of machined channels. Upon comparing the three figures it is clear that the ablation rate increases with increase in fluence. The ablation rates for machining under different atmospheres tend to come closer to

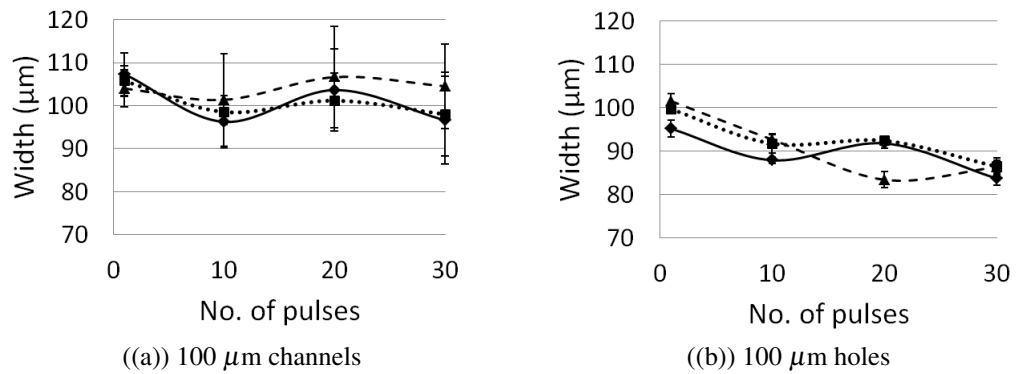


Figure 3.15: The plots of widths of 100 μm channels and holes machined in SS as functions of the number of pulses, at the fluence of $4 J/cm^2$ and with 30 pulses. The widths remain close to the standard dimension of 100 μm . In each of the figures, the solid, dotted and dashed lines represent atmospheres of air, helium and oxygen, respectively. The error bars show the standard errors. Where not visible, the error bars are smaller than the size of the symbols.

each other in value as the fluence is increased, implying that at higher fluence, the ambient atmosphere plays a diminished role. The ablation rate, particularly at high fluences, decreases with increasing number of pulses. This is due to the fact that greater depth per pulse is observed at higher fluences. Material ejection is difficult from greater depth and at high fluences due to formation of a stronger plasma plume, plasma shielding effects and requirement of higher ejection pressures. Such an observation is not made at low fluences (see Fig. 3.14(a)).

Figure 3.15(a) shows the width of the channels machined under different atmospheres at the fluence of $4 J/cm^2$. It can be observed from the figure that the widths of the channels remain practically invariant with changes in machining parameters, and remain close to the beam spot size of 100 μm .

3.2.3 Analysis of 100 μm diameter holes in SS

The scanning electron micrographs of some of the holes are shown in Fig. 3.16. Observing the amount of dross in the figures (compare any three holes machined with the same fluence), it can be inferred that machining under helium is the cleanest with least amount of dross,

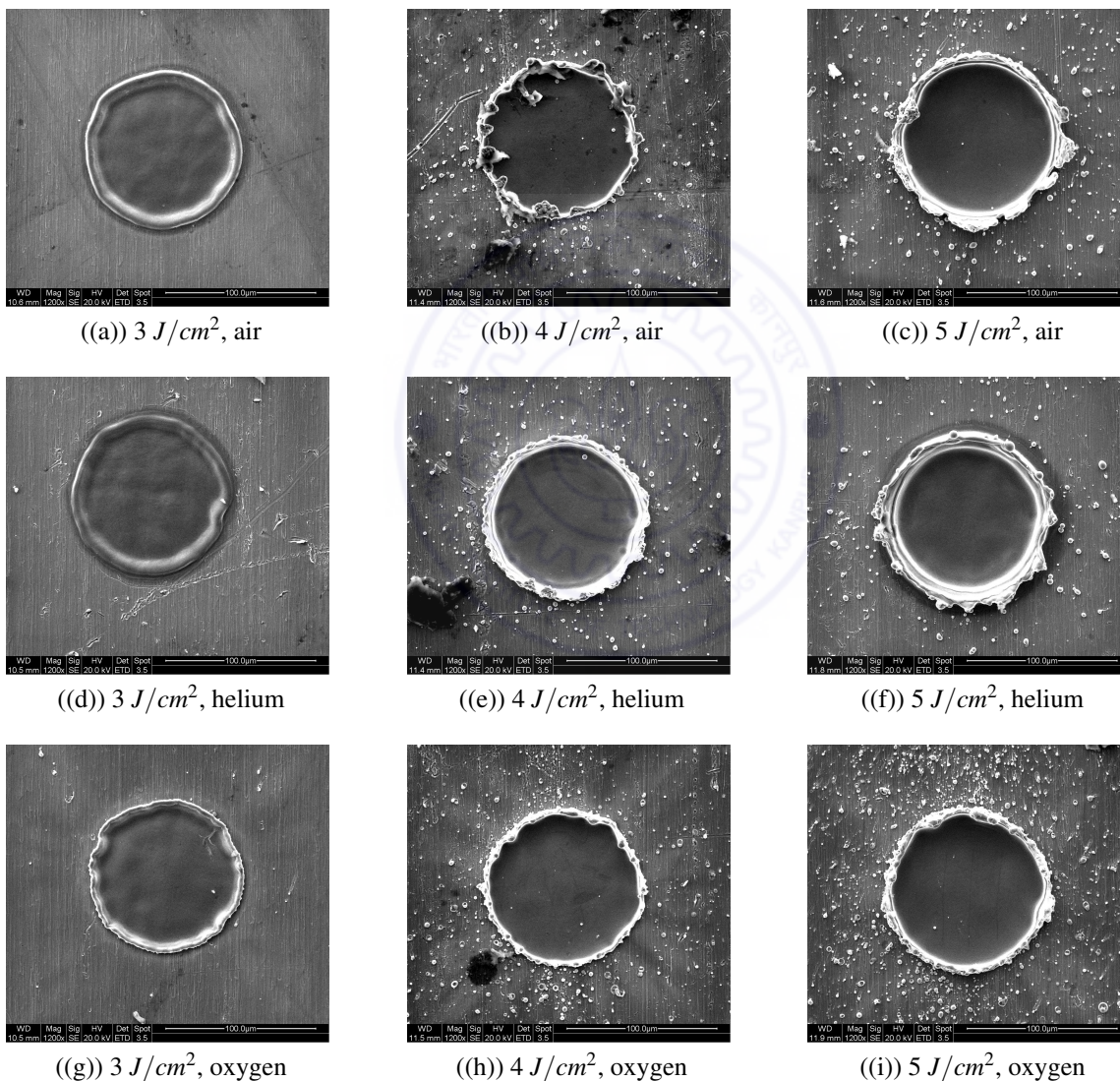


Figure 3.16: The scanning electron micrographs of 100 μm dia holes machined in SS. From the top row to the bottom, the holes have been machined in air, helium and oxygen, respectively. From the left column to the right, the holes have been machined at 3, 4, 5 J/cm^2 , respectively. All holes have been machined with 30 pulses.

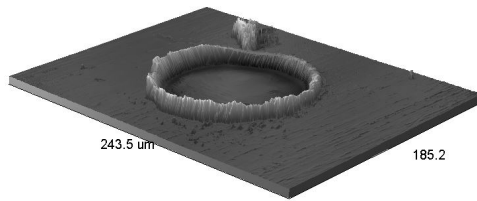
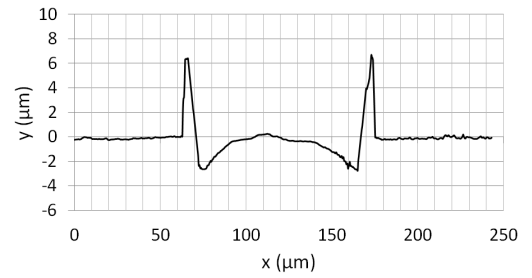
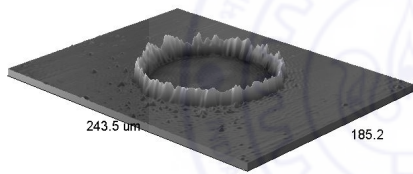
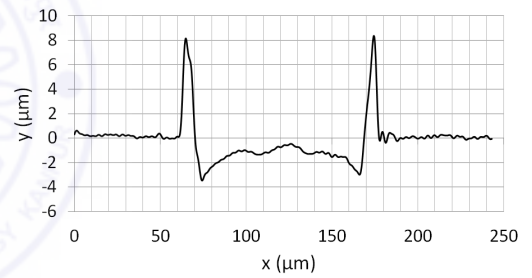
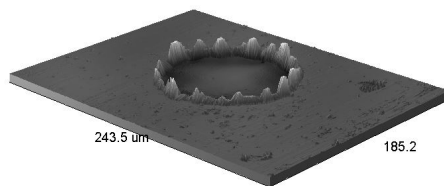
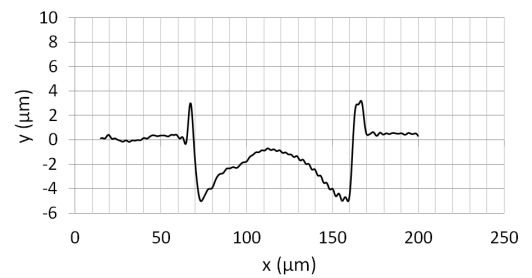
((a)) $5 J/cm^2$, air((b)) $5 J/cm^2$, air((c)) $5 J/cm^2$, helium((d)) $5 J/cm^2$, helium((e)) $5 J/cm^2$, oxygen((f)) $5 J/cm^2$, oxygen

Figure 3.17: The 3D and cross-sectional profiles of $100 \mu\text{m}$ diameter holes machined in SS. From the top row to the bottom, the channels have been machined in air, helium and oxygen, respectively, all at $5 J/cm^2$ and with 30 pulses.

or material scattered around the machined area. Dross is found to be greatest in case of machining under oxygen. This follows directly from our earlier discussion on the effect of oxygen content on the height of the resolidified wall. While the oxygen content reduces resolidification, it aids in scattering the material around the machining zone due to excess heat of oxidation. It is proposed that until the material is ejected, most of the molten material does not get exposed to oxygen. While it gets ejected, it reacts with oxygen and this causes a secondary explosive removal. This secondary explosive removal is responsible for scattering of the molten material that would have otherwise formed a resolidified wall.

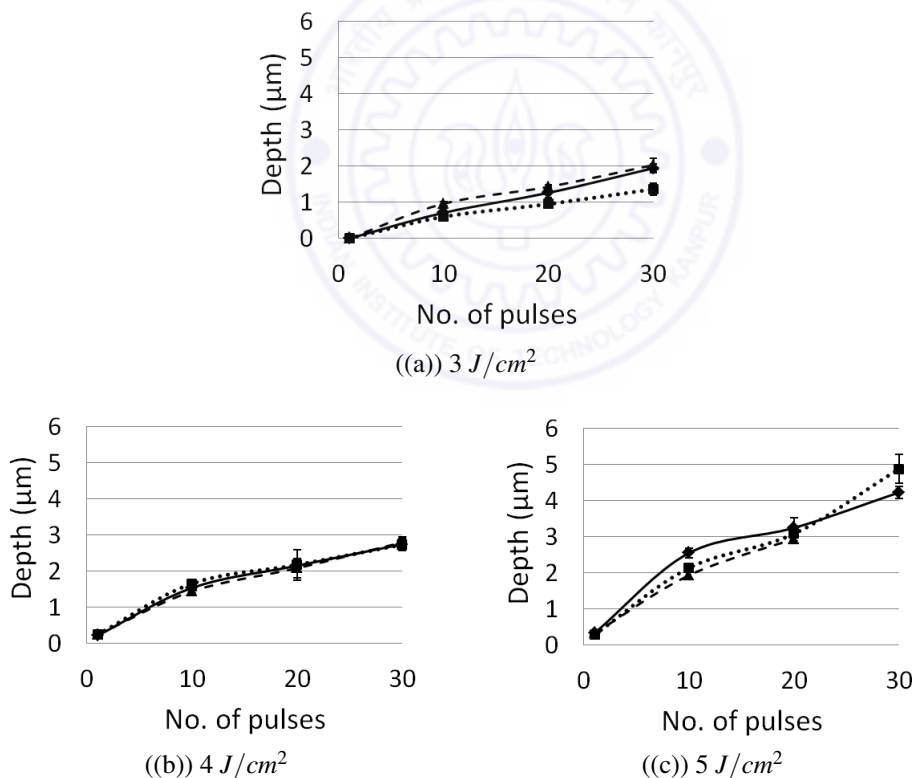


Figure 3.18: The ablation depths of 100 μm diameter holes machined in SS as functions of the number of pulses, at fluences of 3, 4 and 5 J/cm^2 , from left to right. In each of the figures, the solid, dotted and dashed lines represent atmospheres of air, helium and oxygen, respectively. The error bars show the standard errors. Where not visible, the error bars are smaller than the size of the symbols.

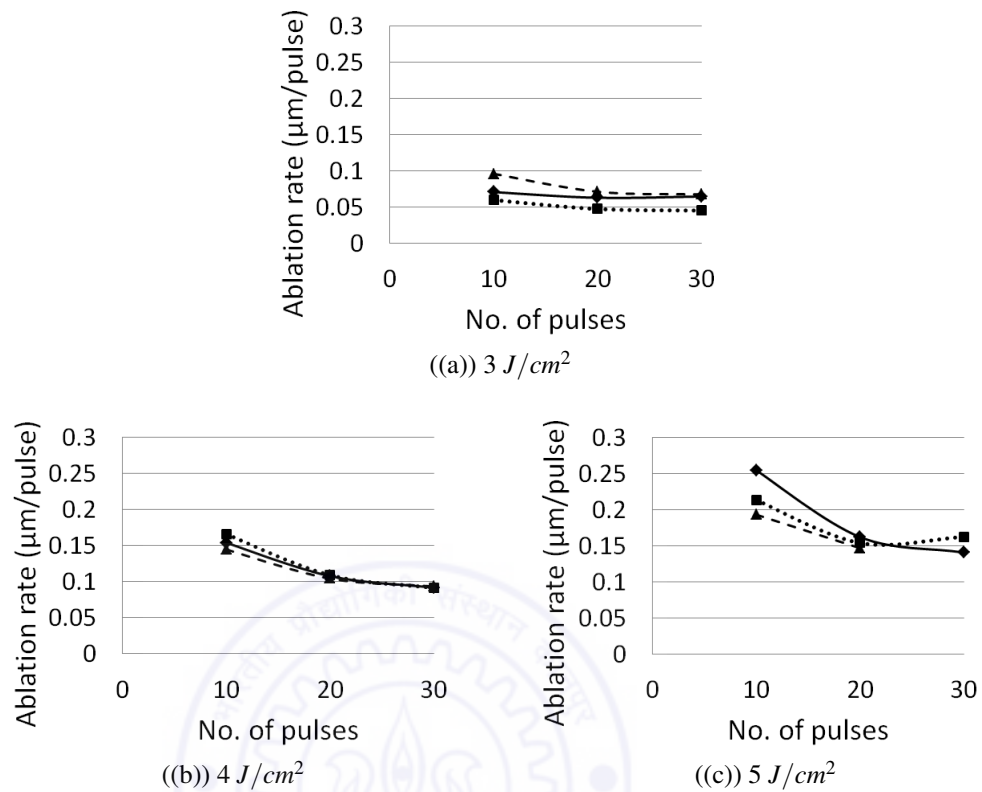


Figure 3.19: The ablation rates of $100 \mu\text{m}$ diameter holes machined in SS as functions of the number of pulses, at fluences of 3, 4 and $5 J/cm^2$, from left to right. In each of the figures, the solid, dotted and dashed lines represent atmospheres of air, helium and oxygen, respectively.

The cross sectional profiles of the holes in Fig. 3.17 show that the height of the resolidified wall is the smallest in case of machining under oxygen, and highest in the case of machining under helium. This is similar to the observations for the case of channels.

The variations in ablation depth for holes are similar to those for channels (see Fig. 3.18 and 3.19), except for the fact that lower depths and ablation rates are observed in case of holes as compared to those for channels. The maximum depths and ablation rates observed at $4 J/cm^2$ are $2.8 \mu\text{m}$ and $0.1 \mu\text{m}/\text{pulse}$. Moreover, the ablation environment (ambient atmosphere) plays a comparatively smaller role in the case of machining holes. The holes, as they get machined, act as a confined space. In addition to material ejection being difficult

from a confined space, the confined plasma hinders the underlying surface from getting irradiated. The confined space even prevents the material from coming in contact with oxygen (or other reactive gases) and hence the oxygen content of the ambient atmosphere does not significantly affect the ablation efficiency, as is observed from Fig. 3.18(a) and 3.18(b). Such confinement is fairly reduced in case of channels because of the large longitudinal dimension (≈ 2 mm), which allows easy expansion of plasma and ejection of material. Hence lower depths and ablation rates are observed in case of holes as compared to those in channels. The widths of the holes do not show any uniform variation with fluence or the number of pulses, as can be seen from Fig. 3.15(b).

3.3 Conclusions

The ablation of metals by excimer laser is numerically modeled in various ways, by considering thermal ablation with and without traveling heat source and fluid flow. The models assume all absorbed laser energy is converted into heat (no plasma shielding losses) and the material evaporates if the temperature at a particular point exceeds its vaporization temperature. Good convergence has been observed for the static thermal ablation model. The numerical results obtained are compared with the experimental results and it is observed that in the case of steel, the over prediction has been observed upto $5 \mu\text{m}$, owing to negligence of plasma-shielding and other losses in the ablation process. The presented model suggests that thermal ablation is the dominant process in the ablation of metals. At the high values of fluence and short time and length scales, the other numerical models could not converge.

Excimer laser micromachining of channels and holes on a metal (steel) is carried out under varying machining conditions, including the ambient atmosphere. Sharp channels and holes are not observed in the metal, due to the pyrolytic nature of ablation in this case. Prominent ridges are observed along the boundaries of the features. The redeposition increases

with increase in fluence. Cleaner features, with greater resolidification and higher ridges, and lower machining, are observed in the case of micromachining under helium atmosphere, an observation attributed to the high thermal conductivity and specific heat capacity of the helium gas, leading to a quenching effect on the molten metal. Deeper machining is observed in the case of micromachining under oxygen, due to the oxidation of the material during irradiation. The oxidation leads to rise in temperature, and hence, aids in material removal.

The depth of ablation increases with increase in fluence, and the ablation rate decreases with the number of pulses. The variations in ablation rate with ambient atmosphere reduce with increase in fluence. The excimer laser ablation rates of steel range from $0.1 \mu\text{m}$ per pulse to $0.5 \mu\text{m}$ per pulse for microchannels, and lie close to $0.1 \mu\text{m}$ per pulse for microholes. Lower depth of ablation is observed in case of micromachining holes, as compared to micromachining channels, because the holes act as a confined space for the material to be ejected. Since the absorption coefficient of metals for UV radiation is very large, the optical penetration depth in metals is very small. Hence the laser-material interaction is almost a surface phenomenon, the reason for observing small ablation rates. For laser micromachining of metals, the ablation efficiency of the laser pulses is found to increase with increase in pulse energy.

Chapter 4

Excimer laser micromachining of polymers, influence of plasma plume absorption and ambient gas

UV lasers have traditionally been used with polymers, specifically photo-resists, for lithographic applications. Lately, direct laser micromachining of polymers, with pulsed UV lasers, is finding wide applications. Researchers are able to fabricate micro components and micro channels directly on polymers. Although the quality of features thus produced is satisfactory in many cases, the understanding of the mechanism of laser ablation of polymers is still growing. This chapter begins with studying the applicability of a thermal ablation model for polymers, and then presents a dynamic photo-ablation model that incorporates plasma shielding effects, to better predict the ablation depth. 10 and 100 μm wide channels have been fabricated, and analyzed for the depths and widths of ablation, on three kinds of polymers. The effect of ambient atmosphere on the nanosecond UV laser ablation of polymers has been studied.

Table 4.1: Material properties used in the thermal ablation model. Specific heat capacity (C_p), thermal conductivity (κ), density (ρ), vaporization temperature (T_{vap}), linear absorption coefficient (α) and surface reflectance (R) are mentioned.

Material	$C_p(J/kgK)$	$\kappa(W/mK)$	$\rho(kg/m^3)$	$T_{vap}(K)$	$\alpha(m^{-1})$	R
PMMA	1420	0.19	1190	473	6300	0.2
Air	1.005	0.0271	1.127	-	-	-

4.1 A static thermal ablation model

The model, including the domain and boundary conditions used for the simulation of polymer machining has been explained in detail in Section 3.1.1. The heat source for the laser irradiance is defined as

$$Q(y) = (1 - R)\alpha I(y), \quad (4.1)$$

for a dielectric material like PMMA. The symbols have their usual meanings, and the values of the material properties are tabulated in Table 4.1. The irradiation is modeled as a volume heat source for PMMA. As discussed in the following section, the polymer undergoes majorly photolytic ablation that lasts for as long as the laser pulse, and there is direct ejection of fragments (vaporization) without much increase in temperature. The duration of the laser pulse is too short (20 ns) to allow for large effects of heat conduction. Considering these, the thermal properties of PMMA have not been varied with temperature during the simulation.

4.2 A dynamic photo-ablation model

The photolytic ablation proceeds via net polymer chain scissions caused by the incident photons. Among the competing mechanisms of bond scission and cross linking in polymer chains, both of which are probabilistic, a net bond scission is obtained when the photon flux density exceeds a certain threshold. A dynamic model had been proposed by Sutcliffe and Srinivasan (1986), in which this threshold is called the flux threshold. It is described as the volume density of photons per second, above which the number of bonds being broken are more than those being formed and above this threshold ablation sets in. The number of bonds needed to be broken, before ablation sets in, is represented by an effective photon density over and above the flux threshold. The quantum efficiency of bond scission is implicit in this model.

The workpiece is modeled as a two-dimensional domain with a depth of ‘ Y ’. At any depth ‘ y ’ from the top of the machined surface, the intensity of radiation at a time ‘ t ’ can be expressed, according to the Beer-Lambert law, as

$$I(y) = I_0 e^{-\alpha y}. \quad (4.2)$$

Here, ‘ I_0 ’ is the intensity at the top surface, measured in W/m^2 , and ‘ α ’ is the linear absorption coefficient of the material at 248 nm wavelength.

The photon flux density, ϕ_p , at the depth ‘ y ’, can then be expressed as

$$\phi_p(y,t) = \alpha I(y,t) / e_{ph}, \quad (4.3)$$

where, e_{ph} is the energy of a single photon.

A net bond scission is obtained when the photon flux, ϕ_p , exceeds the flux threshold, $\phi_{p,th}$. The volume density of such photons, ϑ (called as the effective photon density), at the

depth ‘ y ’ and time ‘ t ’, is obtained by integrating the excess photon flux over time.

$$\vartheta(y, t) = \int_0^t \Gamma \{ \phi_p(y, \hat{t}) - \phi_{p,th} \} d\hat{t}, \quad (4.4)$$

where, Γ takes only the positive part of the expression.

Assuming an implicit quantum efficiency of bond breakage, ablation sets in after the effective photon density exceeds a threshold level, ϑ_{th} . The layer in consideration (at depth ‘ y ’) is considered to be removed when $\vartheta(y, t)$ exceeds ϑ_{th} .

This model does not assume effects such as plasma shielding and absorption of incident radiation over the walls of the machined feature. Both of these tend to decrease the absorbed radiation, and hence lower the ablation rate. It is to be noted that as the depth of a machined feature increases, further machining becomes more difficult. This is because plasma plume is more confined in deeper features. The confined plasma not only absorbs the incoming radiation strongly, but also prevents the ablated fragments from getting ejected out of the material. To consider these effects we propose that, the intensity incident on a layer at depth ‘ y ’ from the top surface is reduced depending on the depth to which the feature has already been machined. The intensity, $\bar{I}(y, t)$, is then expressed as

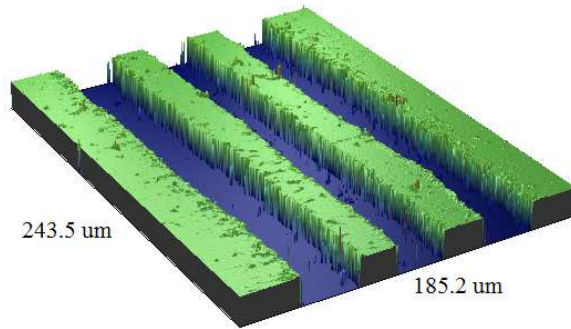
$$\bar{I}(y, t) = I(y, t) e^{a \cdot d(t)^p}, \quad (4.5)$$

where, ‘ a ’ and ‘ p ’ are constants, and ‘ $d(t)$ ’ is the machined depth at time ‘ t ’.

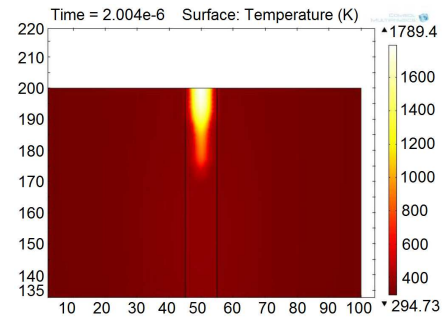
From Eqs. 4.3 to and 4.5, the condition for ablation, while considering plasma shielding, can be modified as

$$\bar{\vartheta}(y, t) = \int_0^t \Gamma \{ \alpha \cdot \bar{I}(y, \hat{t}) / e_{ph} - \phi_{p,th} \} d\hat{t} > \vartheta_{th}. \quad (4.6)$$

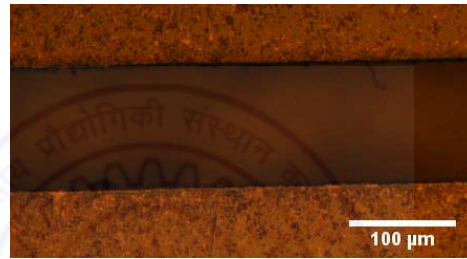
The constants $\phi_{p,th}$ and ϑ_{th} have been determined by Srinivasan and Sutcliffe by fitting the simulated ablation curve to the experimentally observed case, for PMMA and Kapton.



((a)) Surface profile of channels in PMMA showing sharp boundaries



((b)) Simulated temperature profile of a channel in PMMA showing the extent of ablation in terms of temperature



((c)) Micrograph of a channel in PMMA showing the boundaries. The roughness of the boundary is $0.7 \mu m$.

Figure 4.1: Typical results for micro channels machined in PMMA

These constants for the case of boPET are determined in this work, and so also the constants ‘ a ’ and ‘ p ’ for all three polymers.

4.3 Results and discussion

Contrary to the observations for metals (steel), sharp channels are observed in case of polymers (e.g. PMMA, see Figure 4.1) with well defined boundaries, nearly vertical sidewalls and nearly flat bottom surface. The micrograph of a typical channel machined in PMMA is shown in Figure 4.1(c), where the roughness of the boundary is $0.7 \mu m$. The sharpness of the features in a polymer is due to the fact that its ablation with nanosecond UV lasers is mostly

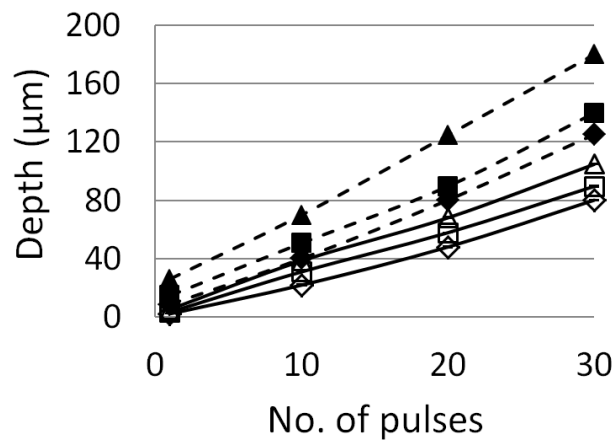


Figure 4.2: Comparison of experimental (solid lines) and simulated (dashed lines, using the thermal ablation model) results from micromachining PMMA. The symbols \blacklozenge , \blacksquare and \blacktriangle represent fluences of 3, 4 and 5 J/cm², respectively. The error bars show the standard errors. Where not visible, the error bars are smaller than the size of the symbols.

photolytic and does not suffer from thermally induced deformations.

PMMA is a widely used polymer in laser micromachining. It is machined by various kinds of lasers, and hence the preliminary investigation of its ablation is carried out using the thermal ablation model presented in Section 4.1. A comparison of the experimental and simulated values of the depths of ablation, for fluences of 3, 4 and 5 J/cm², is shown in Fig. 4.2. The figure shows that the depth (and so also the aspect ratio) increases with increase in energy per pulse. Lazare et al. (1999) and Jensen (2004) report a constant slope of this graph, which is in agreement with the experimental results. The actual depth per pulse, calculated by dividing the depth of ablation by the number of pulses, ranges from 2.4 μm and 3.6 μm , similar to those reported by Jensen (2004); Bailey (25 July 2012); Srinivasan et al. (1986). The depth per pulse calculated from the numerical model ranges from 4.1 μm to 6.4 μm . The static thermal ablation model over-predicts the depth of ablation by 70%, on an average. The reasons for over prediction are the negligence of photoablation, plasma shielding and scattering losses in the numerical model.

The major reason for over-prediction, in addition to those for stainless steel, is the dominating role of photoablation in PMMA, specially at UV wavelengths [Garrison and Srinivasan (1985); Leong (1999); Bailey (25 July 2012)]. A rule of thumb for ascertaining the comparative contributions of photoablation and thermal ablation to the total ablation, is to compare the optical penetration depth with the thermal penetration depth for the material [Jensen (2004)]. For PMMA, the optical penetration depth is around $160 \mu\text{m}$ and the thermal penetration depth is around $0.1 \mu\text{m}$, clearly suggesting that photoablation dominates in PMMA. Bailey (25 July 2012) reports that the thermal component of the total fluence for PMMA at 248 nm is merely 20%, and remains constant for fluences about 1 J/cm^2 . In the experiments conducted in this study, the thermal component being around 0.2 J/cm^2 , is considerably smaller as compared to the total fluence, and hence, photoablation plays a dominating role.

The depth-to-width aspect ratios of the machined micro channels follow the same trend as the depth, because of highly directional machining, specially in case of polymers. The ablation in polymers is mostly photolytic in nature, in which case, the material ablation takes place only from the laser irradiated region. Little lateral heat dissipation occurs in polymers during the pulse irradiation, due to their poor thermal conductivity, and little heat transfer takes place from the irradiated region to the neighboring regions.

4.3.1 Ablation rates

The ablation rates for Kapton, PMMA and boPET have been generated using the model proposed by Sutcliffe and Srinivasan and are shown in Fig. 4.3. The constants $\phi_{p,th}$ and ϑ_{th} used for generating these curves are tabulated in Table 4.2. The constants for boPET have been determined by fitting the simulated curve to the experimental data points. The variation of ablation rate with the logarithm of fluence significantly depends on the linear absorption coefficient. The ablation rate shows an approximately linear variation for large

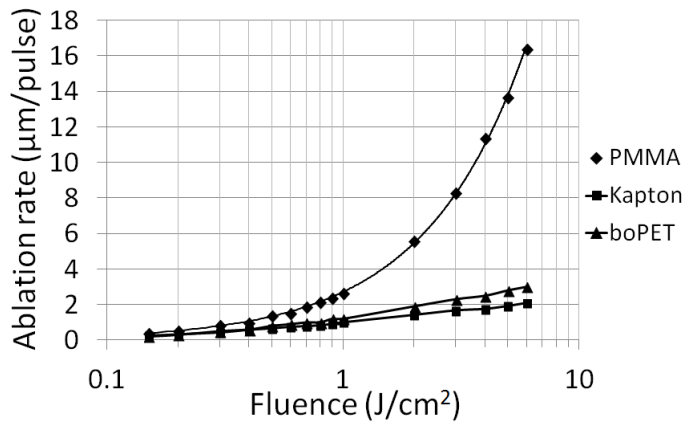


Figure 4.3: Ablation curves for Kapton, PMMA and boPET while machining with 248 nm, 20 ns (FWHM) laser pulses

values of α , e.g. for Kapton and boPET. For PMMA, with α three orders of magnitude smaller than the former, a highly non-linear dependence is observed, which is attributed to the deep penetration of radiation in PMMA and lower ablation threshold. With every incremental unit of fluence, a significantly higher ablation rate is observed.

Table 4.2: Ablation threshold parameters determined for various polymers by fitting the simulated curves to the experimental data. $\phi_{p,th}$ and ϑ_{th} are the photon flux threshold and the effective photon density threshold, respectively. [The parameters for Kapton and PMMA are taken from Sutcliffe and Srinivasan (1986)]

	$\phi_{p,th}$ (phots. per sec per cu.m)	ϑ_{th} (phots. per cu.m)
Kapton	3.1×10^{35}	4.1×10^{27}
PMMA	4.3×10^{33}	4.1×10^{27}
boPET	4.9×10^{35}	4.1×10^{27}

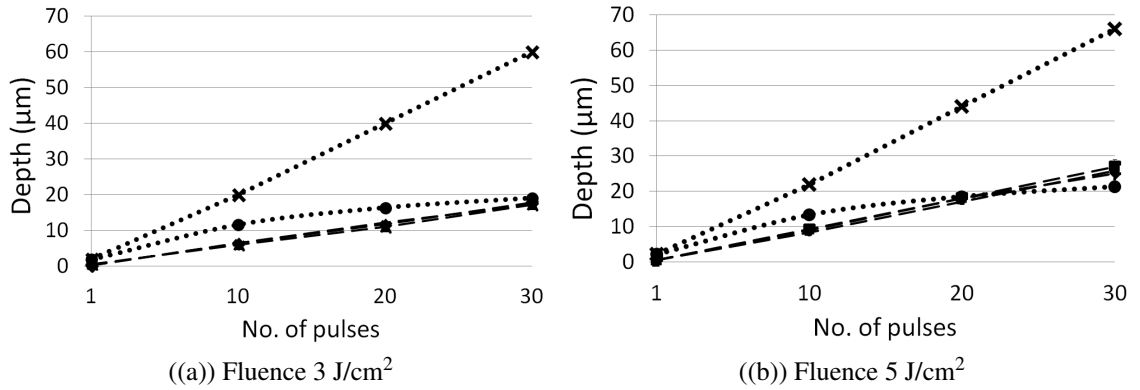


Figure 4.4: Depth plots for Kapton at 3 and 5 J/cm² (channel width 100μm). The dotted and dashed lines represent simulated and experimental values, respectively. × and • are without and with plasma shielding being considered, respectively. The ◆, ■ and ▲ indicate machining in air, helium and oxygen atmospheres, respectively. The error bars show the standard errors. Where not visible, the error bars are smaller than the size of the symbols.

4.3.2 Ablative machining of Kapton

Fig. 4.4 shows the plots of the depth of the 100 μm channels against the number of pulses for three different atmospheres at the fluence of 3 and 5 J/cm². In all plots shown in this chapter, discrete data points have been obtained from experiments and the lines are a guide to the eye only. The trends obtained for the fluence of 4 J/cm² being the same as that for the minimum and maximum fluence used, have not been discussed separately. It is seen from Fig. 4.4(a) that the depth of the machined channels increases linearly with the number of pulses irrespective of the ambient atmosphere. A similar trend is observed from Fig. 4.4(b) that shows the data for the channels machined at 5 J/cm². The dotted lines in the figures represent values of depths obtained from the dynamic ablation model. Without considering effects such as plasma shielding, the predicted values of depth are significantly higher than the experimental values. The predicted depth continues to increase with the number of pulses, indicating the ability to machine holes with as high a depth as desired. It is known that there is a limit to the aspect ratio that can be achieved with any kind of machining, and

so also with laser machining [Lazare and Tokarev (2004); Lazare et al. (1999); Tokarev et al. (2000)]. The machined depth saturates with fluence, as well as the number of pulses. The curved dotted line represents the ablated depth obtained from the model after considering the plasma shielding effect. The constants ' a ' and ' p ' have been determined by fitting the ablation curve to the experimentally observed values. These have been estimated to be -0.17 and 1.01, respectively.

The fact that the ambient atmosphere does not affect the extent of ablation in Kapton suggests the ablation to be a strong photolytic ablation process. The ablation appears to be purely due to photon-material interaction inside the surface of the material. The polymer chains broken by the photons get expelled out of the material [Jensen (2004)] and this is not affected by the atmosphere present outside the material. It also shows that the expelled material does not interact with the ambient atmosphere unlike what happens in the case of metals [refer Low et al. (2000); Yeo et al. (1994)]. This becomes more understandable when we note that photolytic ablation leads to minimal rise in temperature and hence the ablated material does not experience elevated temperatures under which it may react with gases like oxygen, which in itself is an exothermic reaction further raising the local temperature as in metals. Atmosphere has been noted to affect ablation in case of longer duration pulses (pulse durations of the order of microsecond and millisecond) due to the fact that thermal effects in ablation are more pronounced at such time scales [Srinivasan et al. (1995)]. Oxygen, or the lack of it, has been noted to significantly affect the composition of the products of ablation.

Fig. 4.5 shows the variation of the depth of the machined channels with the number of pulses for various fluence. As is obvious from the figure, the depth varies linearly with fluence as well as the number of pulses. The linear dependence of the machined depth has been observed by researchers earlier (e.g. see [Meijer (2004); Lazare and Tokarev (2004); Jensen (2004); Srinivasan et al. (1986)]). However, it is prudent to point out here that the above mentioned observations hold true for a certain range of fluence (see [Srinivasan et al.

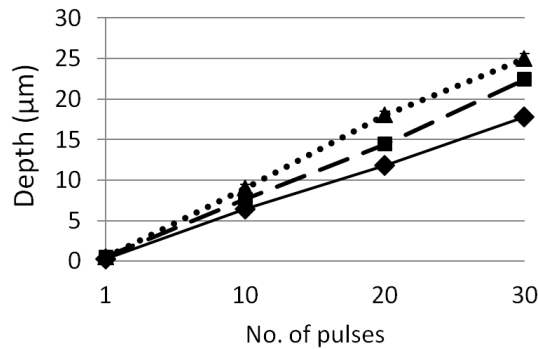


Figure 4.5: Depth plot for Kapton machined in air (channel width $100\mu\text{m}$). The \blacklozenge , \blacksquare and \blacktriangle indicate machining at the fluences of 3, 4 and 5 J/cm^2 , respectively. The error bars show the standard errors. Where not visible, the error bars are smaller than the size of the symbols.

(1986)], the feature size (lateral dimensions) and the ablated depth. For very small sizes ($5\ \mu\text{m}$ or less) and for roughly the same order of ablated depth the ejection of the material becomes increasingly difficult with increasing depth. In order to machine deeper features in such cases the beam's numerical aperture and the fluence become significant factors [Lazare et al. (1999)]. Ultimately the machined feature size is limited by diffraction at very small length scales [Dayal et al. (2013a)].

Fig. 4.6 shows the plots for $10\ \mu\text{m}$ wide channels for varying fluence under helium and oxygen atmospheres. Although most of the observations made for the larger channels hold true in this case as well, it can be noted that at the highest fluence of 5 J/cm^2 the depth tends to saturate with increasing number of pulses. It is possible, in this case, to achieve a greater depth using a lower fluence. This phenomenon is typical of photolytic ablation of Kapton at length scales of the order of a single micrometer. Kapton has been reported to release many gaseous products (like CO, HCN and C_2H_2) upon irradiation with laser and these contribute to 45% of the mass of the ablated polymer [Srinivasan et al. (1995)]. Clearly with increasing number of pulses greater quantities of such gases are formed deeper into the surface. Some amount of these gases escape into the ambient atmosphere and some gets trapped in the plasma (also partially leading to secondary absorption of incoming photons). The remaining

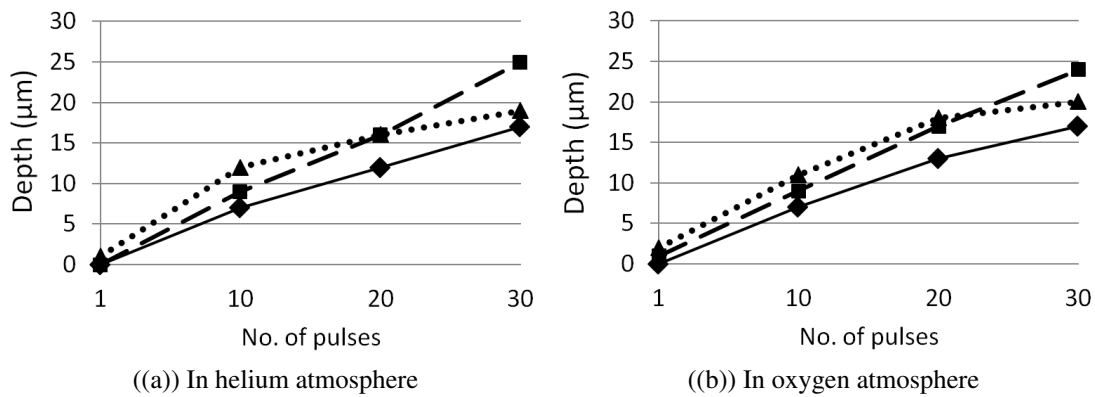


Figure 4.6: Depth plots for Kapton under helium and oxygen atmospheres (channel width $10\mu\text{m}$). The \blacklozenge , \blacksquare and \blacktriangle indicate machining at the fluences of 3, 4 and 5 J/cm^2 , respectively. The error bars show the standard errors. Where not visible, the error bars are smaller than the size of the symbols.

portion of these gases does not leave the parent material; rather it remains trapped inside it. This entrapment of gases leads to swelling up of the irradiated surface of the polymer. The swelling up of Kapton is schematically shown in Fig. 4.7. It is suggested that the decrease in observed depth at the highest fluence of 5 J/cm^2 is due to the swelling up of the bottom surface of the machined channels that makes them to appear shallower. The high fluence over a small area ($10\mu\text{m}$ wide channel in this case) instantaneously generates a strong and

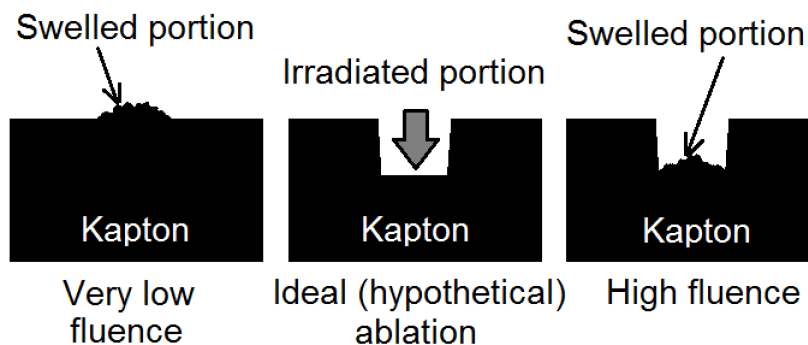


Figure 4.7: Schematic of swelling observed in Kapton when irradiated with a laser pulse, leading to a reduced depth at high fluence

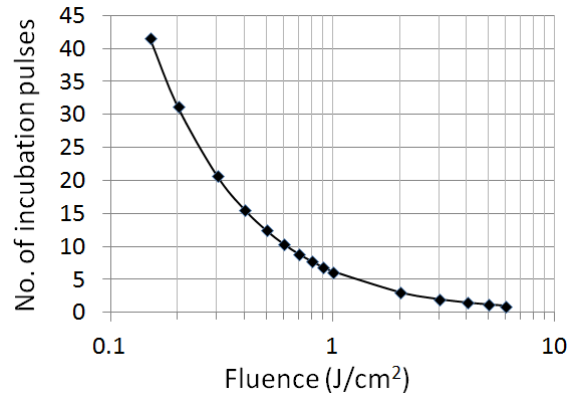


Figure 4.8: Number of (incubation) pulses required to initiate ablation in PMMA as a function of fluence, calculated from the dynamic photo-ablation model

confined plasma inside the machined region. This plasma obstructs the remainder of the incoming pulse thereby decreasing the efficiency of ablation. Further, the confined plasma confines the ablated fragments inside the machined region and causes them to redeposit, thereby decreasing the effective depth of ablation.

4.3.3 Ablative machining of PMMA

PMMA is a considerably weaker absorber when compared to Kapton and boPET (refer their respective absorption coefficients in Table 1.2). The radiation penetrates deep into the material, and as a result, lesser number of photons are available per unit depth. Hence it takes a large number of pulses, called incubation pulses, to irradiate PMMA, before the photon flux crosses a threshold, and ablation is initiated. Figure 4.8 shows the plot of the number of incubation pulses vs. fluence. The number of incubation pulses have been estimated from the dynamic photo-ablation model, by varying the input photon energy (fluence), and counting the number of pulses before ablation sets in. After the material (PMMA in our case) has been irradiated with the incubation pulses, there are enough number of broken polymer chains (within the irradiated volume) that explode out. While studying the ablation charac-

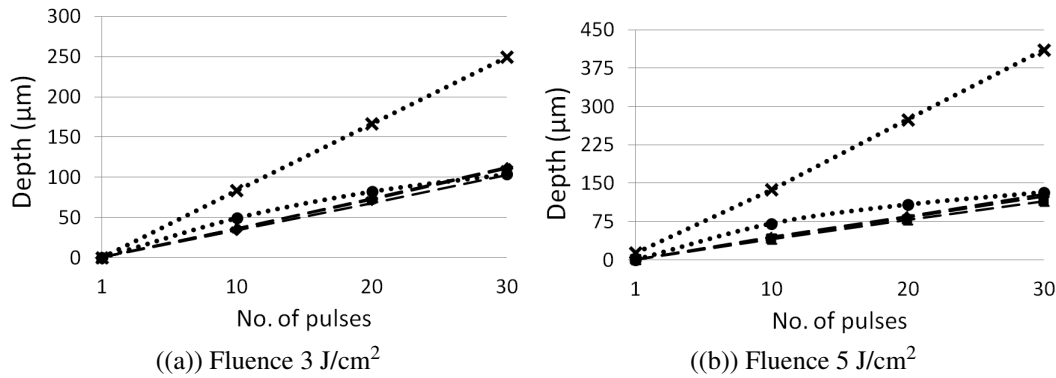


Figure 4.9: Depth plots for PMMA at 3 and 5 J/cm² (channel width 100μm). The dotted and dashed lines represent simulated and experimental values, respectively. × and • are without and with plasma shielding being considered, respectively. The ◆, ■ and ▲ indicate machining in air, helium and oxygen atmospheres, respectively. The error bars show the standard errors. Where not visible, the error bars are smaller than the size of the symbols.

teristics of PMMA, the requirement of incubation pulses should be considered in order to interpret the ablation behavior correctly. Contrary to this, ablation in Kapton and boPET sets in within the first pulse itself.

Fig. 4.9 shows the plots of the depth of the 100μm channels against the number of pulses for three different atmospheres at the fluence of 3 and 5 J/cm². All observations being similar to that for Kapton, it is to be noted that the maximum depth achieved in Kapton and PMMA (for 30 pulses at 5 J/cm²) are 26μm and 129μm respectively. The increased depth in case of PMMA is majorly due to the very low value of the absorption coefficient ($\alpha = 0.0063 \mu m^{-1}$) as compared to that for Kapton ($\alpha = 22 \mu m^{-1}$). The low value of the absorption coefficient leads to a high penetration depth into the surface of the polymer. The absorption coefficients and the optical penetration depths are summarized in Table 1.2. Other factors that influence the extent of ablation are the types of bonds present in the polymer, the critical bond density for initiation of ablation and the melting temperature. The constants ‘*a*’ and ‘*p*’ for PMMA have been determined to be -0.13 and 0.95, respectively.

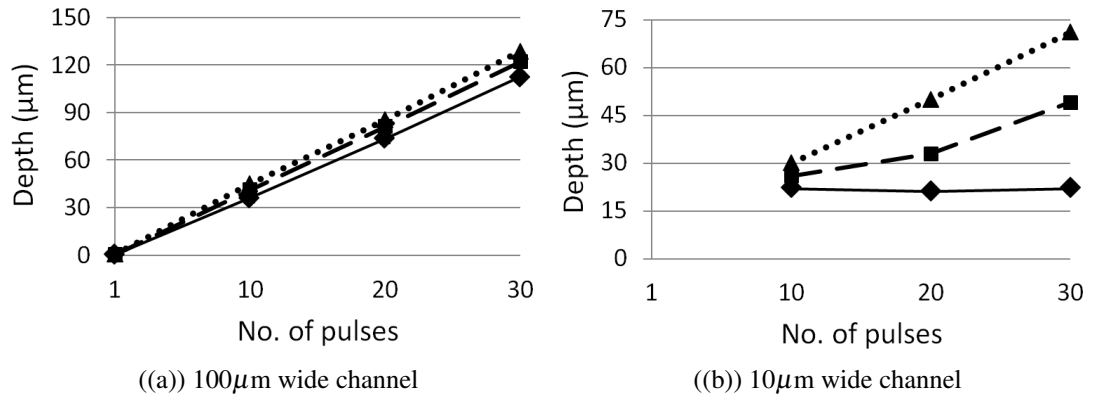


Figure 4.10: Depth plots for PMMA for 100 and 10 μm wide channels machined in normal atmosphere. The \blacklozenge , \blacksquare and \blacktriangle indicate machining at the fluences of 3, 4 and 5 J/cm², respectively. The error bars show the standard errors. Where not visible, the error bars are smaller than the size of the symbols.

Fig. 4.10 shows the plots of the depth of the 100 μm and 10 μm channels against the number of pulses under normal atmosphere. It is to be noted that the depth in case of 10 μm wide channels (Fig. 4.10(b)) is considerably smaller as compared to that for larger 100 μm channels (Fig. 4.10(a)). This difference is attributed to deeper machining in case of PMMA as compared to that in Kapton and hence this was not noticeable in case of Kapton. The reasons for observing the 10 μm channels to be shallower than the 100 μm channels, for all other conditions being same, are: (1) the ejection of ablated material is difficult from larger depths, (2) a dense and confined plume is formed inside the channel that prevents the material from being ejected out and causes it to redeposit and (3) the confined plume causes absorption of incoming photons thereby allowing fewer photons to hit the polymer surface. It is one of the aims of this study to understand the ablation of polymers at different length scales, and our observations explain the mechanics of polymer fragment ejection from inside a micro feature. Achieving deeper depths in features with small lateral dimensions with few micrometer sizes is non-trivial.

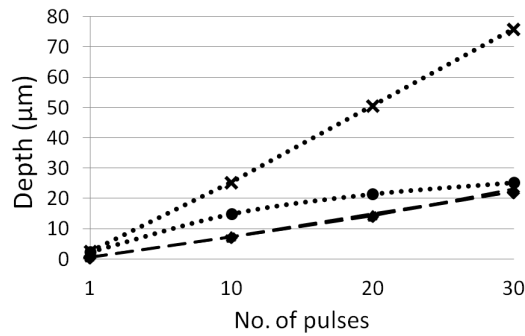


Figure 4.11: Depth plot for boPET at 3 J/cm^2 (channel width $100 \mu\text{m}$). The dotted and dashed lines represent simulated and experimental values, respectively. \times and \bullet are without and with plasma shielding being considered, respectively. The \blacklozenge , \blacksquare and \blacktriangle indicate machining in air, helium and oxygen atmospheres, respectively. The error bars show the standard errors. Where not visible, the error bars are smaller than the size of the symbols.

4.3.4 Ablative machining of boPET

Fig. 4.11 shows the depth plot for boPET at the fluence of 3 J/cm^2 for $100 \mu\text{m}$ wide channels. It can be seen that the maximum depth obtained with 30 pulses at 3 J/cm^2 is $23 \mu\text{m}$, which is close to that for Kapton ($17 \mu\text{m}$), for similar machining conditions. Fig. 4.12 shows the plots of the depth against the number of pulses for the $100 \mu\text{m}$ and $10 \mu\text{m}$ channels respectively. We observe that the maximum depth reached in this case was $34 \mu\text{m}$ which is similar to that for Kapton. Note also that the maximum depths achieved in different polymers with 30 pulses at 5 J/cm^2 are in line with the penetration depths mentioned in Table 1.2. It is also observed, as similar to that in Kapton and unlike PMMA, that both the large width ($100 \mu\text{m}$) and small width ($10 \mu\text{m}$) channels are machined to the same depth, unaffected by the atmosphere. However we do not find anomalous behavior of less depth per pulse at the highest fluence of 5 J/cm^2 , unlike that in Kapton. This suggests that both boPET and PMMA do not release significant amounts of gaseous products upon irradiation with laser so as to affect machining at sub- $10 \mu\text{m}$ scale. The constants ' a ' and ' p ' for boPET have been determined to be -0.17 and 1.01 , respectively.

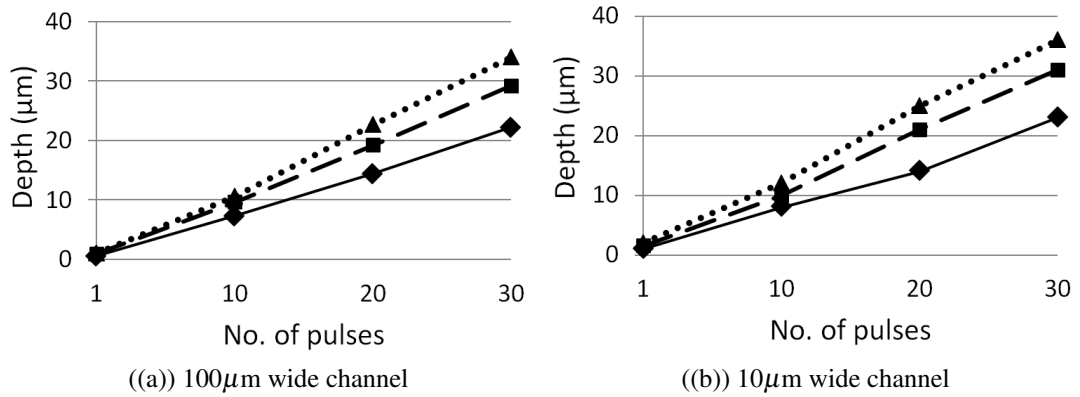


Figure 4.12: Depth plots for boPET for 100 and 10 μm wide channels machined in normal atmosphere. The \blacklozenge , \blacksquare and \blacktriangle indicate machining at the fluences of 3, 4 and 5 J/cm^2 , respectively. The error bars show the standard errors. Where not visible, the error bars are smaller than the size of the symbols.

4.3.5 Discussion on ablation efficiency

The ablation rates of individual pulses have been studied in the preceding subsections. Here, the effect of pulse energy on the ablation efficiency of the pulses is studied, while machining in air. One may recall from the discussion on metals (refer Section 3.2.2 and Fig. 3.11(b)) that for the same amount of energy deposited on the workpiece, higher energy pulses generate higher depths of ablation, in which case, it can be inferred, that higher energy pulses have higher ablation efficiency. Fig. 4.13 shows the plots of depths of ablation vs. the total energy deposited on the surface of three different polymers, for cases of varying fluence (or pulse energy). In each of the figures, the symbols \blacklozenge , \blacksquare and \blacktriangle represent fluences of 3, 4 and 5 J/cm^2 , respectively. These correspond to pulse energies of 0.3, 0.4 and 0.5 mJ, respectively, considering the laser spot size of $100 \mu\text{m} \times 100 \mu\text{m}$ on the workpiece. It can be observed from each figure (and most clearly from Fig. 4.13(a) where the fitted lines are easily distinguishable because of the large depths of ablation) that, for a particular amount of energy deposited on the workpiece, the low energy (or fluence) pulses generate a higher depth of

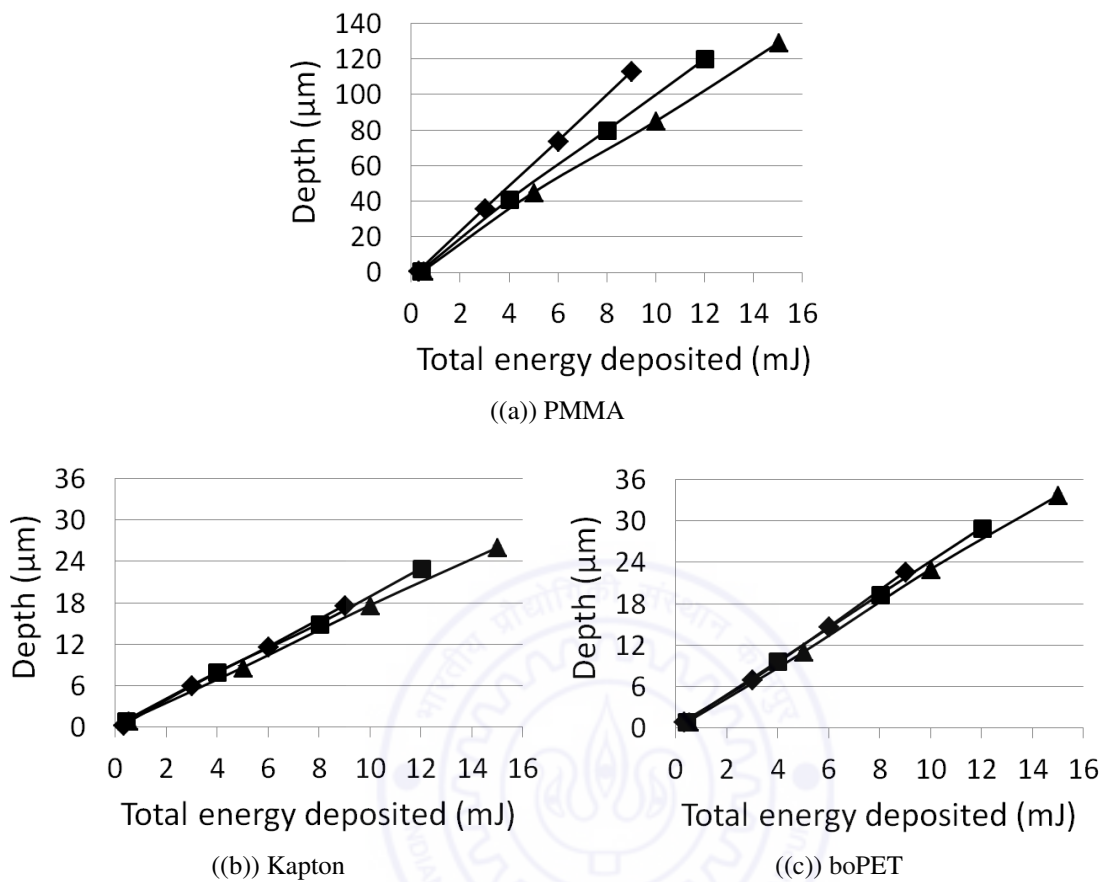


Figure 4.13: Depth plots vs. total energy deposited on the surface of PMMA, Kapton and boPET for 100 μm wide channels machined in normal atmosphere. The symbols \blacklozenge , \blacksquare and \blacktriangle represent fluences of 3, 4 and 5 J/cm^2 , respectively. The error bars show the standard errors. Where not visible, the error bars are smaller than the size of the symbols.

ablation. As an example, referring to Fig. 4.13(a), at the total energy of 8 mJ, the cumulative depths ablated by pulses having fluences of 3, 4 and 5 J/cm^2 , are 97, 78 and 68 μm , respectively. It follows from this observation that in case of polymers, contrary to the case of metals, lower energy (or fluence) pulses are more efficient in ablating material. In other words, more number of lower energy pulses have a higher ablation efficiency compared to that of low number of higher energy pulses. This is true for the case of all three polymers studied in this work.

This observation can be explained by understanding the ablation depth saturation with

pulse energy [Dayal et al. (2013a); Zhang et al. (2001); Jiang et al. (1993)]. The average depth per pulse starts saturating around the fluence of 5 J/cm^2 [Srinivasan et al. (1986)]. The ablation in polymer is photolytic in nature wherein a photon having energy above a certain threshold (bond energy of carbon-carbon bond, that is about 3.5 eV) is enough to break the carbon-carbon (C-C) bond. Low energy pulses do not break enough number of C-C bonds and hence lead to small depths of ablation. Moderate energy pulses are able to break enough number of C-C bonds, and lead to efficient ablation and comparatively greater depths of ablation. High energy pulses break a large number of C-C bonds, but over the same polymer mass (albeit into smaller poly-carbon fragments that explode out) leading to almost similar depths of ablation. The fluences used in this study range from 3 J/cm^2 to 5 J/cm^2 , and fall in the moderate to high range of pulse energies. Hence, beyond a particular pulse energy, the efficiency of ablation (depth per pulse) does not increase.

4.4 Conclusions

A static thermal ablation model has been used for PMMA, and it over predicted the depths of ablation by 70% on an average. It clearly indicates that photolytic ablation dominates the UV laser ablation of polymers. Only about 20% of the incident fluence is used to generate any thermal effects.

A dynamic ablation model has been extended to incorporate the effect of the plasma shielding while machining polymers with excimer laser. The incident fluence is reduced exponentially depending on the depth to which the polymer has been machined. The depths predicted by this model are closer to the experimentally observed values as compared to the ones predicted without considering this effect. Additionally, the depth is found to saturate with fluence, a prediction consistent with the experimental observations. The constants that determine the exponential decay of the incident fluence as a function of depth have been

obtained for Kapton, PMMA and boPET. The constant 'a' has been estimated to be -0.17 for Kapton and boPET, and -0.13 for PMMA. The constant 'p' has been estimated to be 1.01 for Kapton and boPET, and 0.95 for PMMA.

The ablation rates have been predicted by the dynamic ablation model. For Kapton and boPET, the ablation rates increase linearly with the logarithm of the fluence, an observation well known. However, for PMMA, the ablation rate rises exponentially with the logarithm of the fluence, due to the fact that after the ablation threshold is crossed, large depth of PMMA is machined with every pulse, owing to its significantly low absorption coefficient. PMMA is found to require a large number of incubation pulses, owing to its low absorption coefficient. E.g. for fluence lower than 0.2 J/cm^2 , more than 30 pulses are required before ablation sets in. Kapton and boPET, on the other hand, get ablated from the first pulse itself.

The ambient atmosphere does not noticeably affect the nanosecond pulsed laser ablation of polymers owing to the fact that the ablation is entirely photolytic. The ablation mechanism does not lead to any significant rise in temperature, and hence the interaction of irradiated material or the ejected fragments with reactive gases like oxygen is inhibited.

Laser machining of deep features at sub- $10 \mu\text{m}$ lateral dimensions is non-trivial. Smaller kerf width features tend to get machined to smaller depths, owing to the greater plasma plume-laser interaction for high aspect ratio features. This has been found to be more evident in case of PMMA, which gets machined to much higher depths as compared to Kapton and boPET.

Kapton releases considerable amount of gases upon irradiation with laser. This causes it to swell and hence the depth obtained for small lateral dimensions is less than that obtained at larger dimensions. It is found that for small lateral dimensions (of the order of a single micrometer) greater depth can be achieved by using a lower fluence. Although the ablation behavior of boPET is similar to that of Kapton, it does not show the anomalous behavior of Kapton at high fluence. It is understood that boPET, unlike Kapton, does not release

significant amount of gases, if any, upon irradiation with excimer laser. The results presented in this chapter for the excimer laser micromachining of polymers under discussion, provide an understanding that different ablation mechanisms operate at different length scales. The choice of machining parameters, for excimer laser micromachining, needs to be made while considering the lengthscale of machining and the type of polymer.



Chapter 5

Microfeature edge quality enhancement of metal films by coating with a sacrificial polymer layer

Direct micro-patterning of metal films by lasers is an exciting prospect that promises to replace the conventional techniques, because of its one step machining, non-requirement of wet etching and ease of use. The challenge in micro-patterning metal films lies in controlling the sizes of the patterns. The mechanism of ablation of metal films is largely different from that of bulk metals. The tearing of metal films and excessive lateral ablation make it nearly impossible to micro-pattern metal films cleanly. This chapter presents the disadvantage of direct laser micromachining of metal films, while also presenting a novel technique to overcome the disadvantage and to achieve clean ablation.

5.1 Film heating model and numerical simulations

Thin film ablation is quite unlike bulk ablation in that the fluence/temperature required to initiate ablation is much lower than the ablation threshold for the bulk material [Zaleckas and Koo (1977); Matthias et al. (1994); Andrew et al. (1983)]. To understand the levels of temperature reached in the thin metal film and in the substrate, the laser heating process was simulated using a thermal model in a standard finite element analysis software (COMSOL Multiphysics). The model studies the evolution of temperature profile in the metal film over the timescale of the order of 10 ns. The model comprised a 200 nm thick metal film coated on a thick glass substrate. Since glass has a poor thermal conductivity, there is no need to consider the entire thickness of the glass substrate. The properties of glass, aluminum and chromium used for the simulation are mentioned in Table 5.1.

The intensity (I , defined as the average energy flux per unit time, averaged over the period of the wave) attenuates inside the material according to the Beer-Lambert law as

$$I(y) = I(0)e^{-\alpha y}, \quad (5.1)$$

where, $I(y)$ is the intensity at depth, y , into the material and α is the linear absorption coefficient of the material for polymers and skin depth for metals. The laser beam has a uniform top-hat intensity profile across its cross-section, both at the mask plane and at the image plane of the mask (machining plane). Similar spatially uniform intensity distribution has been used in the numerical model. $I(y)$ has the temporal pulse shape defined by a piecewise function with continuous second derivative and having the relative size of the transition zone as 0.499. The function rises from zero to a value of one from 0.2 ns to 5 ns. Subsequently, it decays to zero in another 30 ns. Since the film thickness (200 nm) is smaller than the laser spot size ($100 \mu\text{m} \times 100 \mu\text{m}$) and the thermal diffusion depths of the two metals (refer Section 5.2), there is invariance in directions perpendicular to the thickness. This results in heat diffusion primarily only in one spatial dimension. Hence, a mono-dimensional model

Table 5.1: Thermal and optical properties used in the thermal ablation model. Specific heat capacity (C_p), thermal conductivity (κ), density (ρ), fusion temperature (T_f), enthalpy of fusion (ΔH_f), vaporization temperature (T_v), enthalpy of vaporization (ΔH_v), linear absorption coefficient (α) and surface reflectance (R) are mentioned. [Lide (Internet Version 2005); McDonald (1967); Andrew et al. (1983); Matthias et al. (1995); Attia and El-kader (2013); Shehap (2008); Mustafa (2013)]

Material	Aluminum	Chromium	Borosilicate glass	Polyvinyl alcohol (PVA)
C_p (J/kgK)	$f(T)$	$g(T)$	703	1500
κ (W/mK)	237	93.9	1.38	0.39
ρ (kg/m ³)	2700	7190	2203	1350
T_f (K)	933.5	2130	1093.15* 798.15 (T_g)	437.15
ΔH_f (kJ/kg)	396.96	403.92	-	67.38
T_v (K)	2792	2952	-	501.15
ΔH_v (kJ/kg)	10896.96	6530.11	-	-
α (m ⁻¹)	1.43×10^8	1.17×10^8	-	$5 \times 10^3 - 34.2 \times 10^3$
R	0.86	0.54	-	-

*Softening point

can be used to model heat conduction.

Heat conduction in a material is defined by the transient energy transport equation

$$\rho C_p \frac{\partial T}{\partial t} + \nabla \cdot (-\kappa \nabla T) = Q, \quad (5.2)$$

where, ρ is the density of the material, C_p is the specific heat capacity of the material at

constant pressure, T is temperature, t is time, κ is the thermal conductivity of the material and Q is the heat source (in Watt per unit volume) that takes into account the reflectance as well as the linear absorption coefficient. The specific heat capacities of aluminum ($f(T)$) and chromium ($g(T)$) are functions of temperature as per the NIST database (See Appendix). The latent heats are added to the respective specific heat capacities after distributing those over a small range of temperature. The heat source for the laser irradiance is defined as

$$Q(y) = (1 - R)\alpha I(y). \quad (5.3)$$

Although the surface reflectivity initially increases during melting and decreases after the onset of ablation or plasma formation [Matthias et al. (1995)], we do not consider variation in surface reflectivity. This is because the fluence used is in a moderate range, and secondly a simple model is analyzed to understand the temperature distribution in the metal film. The numerical model is validated using heat balance calculations. By averaging the energy of the pulse over its time period, the total pulse energy is determined to be 32% of the peak energy.

5.2 Results and discussion for straight channels

The thermal diffusion lengths [calculated as $\sqrt{(4\kappa t_p/\rho C_p)}$] for aluminum and chromium, for a 20 ns laser pulse, are 2.8 μm and 1.5 μm respectively. The optical skin depths are 15 nm and 11 nm respectively in aluminum and chromium. Clearly, the thickness of the metal films (100 nm) is an order of magnitude larger than the optical penetration depth and an order of magnitude smaller than the thermal diffusion depth. This implies that there is little thermal gradient across the thickness of the film, and also that the ablation threshold of the film is about an order of magnitude smaller than the bulk ablation threshold [Matthias et al. (1994)].

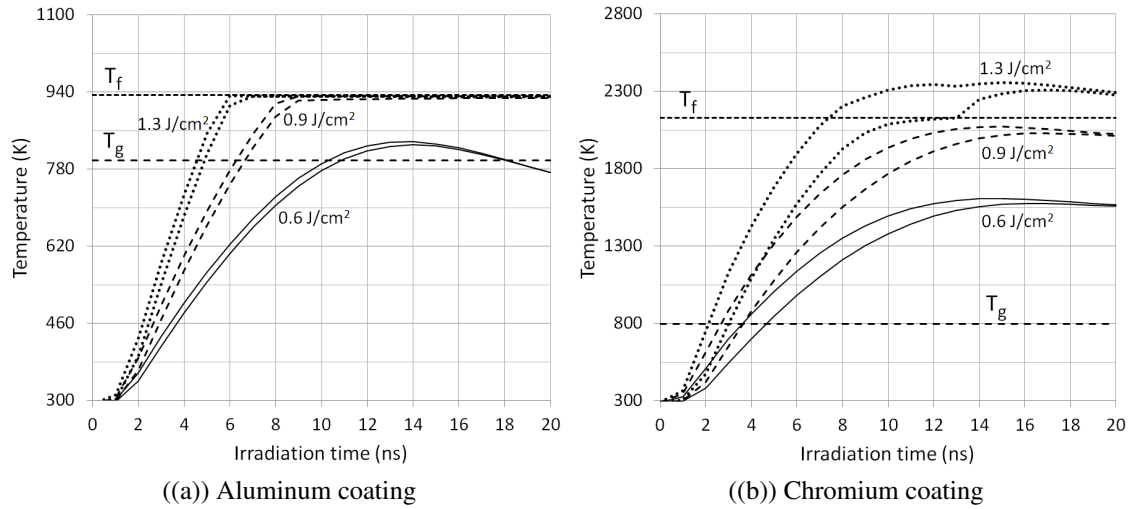


Figure 5.1: The calculated time progression of the temperatures on the top of the metal film and coating-glass interface during laser irradiation at the fluences of 0.6 J/cm^2 (solid curves), 0.9 J/cm^2 (dashed curves) and 1.3 J/cm^2 (dotted curves). The ■ indicate top surface of the coating, and the ◆ indicate the interface. In each set of curves, the top curve indicates the top surface temperature, and the bottom curve indicates the interface temperature. The horizontal short dashed line (---) indicates the fusion temperature (T_f , refer to Table 5.1), and the horizontal long dashed line (---) indicates the glass transition temperature (T_g , 798.15 K). The laser spot size assumed is $100 \mu\text{m}$.

5.2.1 Direct machining of metal film

Figure 5.1 shows the predicted surface and interface temperatures in the aluminum and chromium coated glasses, respectively. These are calculated during irradiation at the fluences of 0.6 , 0.9 and 1.3 J/cm^2 . The times in which the temperatures at the top surface reach the fusion temperatures of aluminum (T_f^{Al} , 933.5 K) and chromium (T_f^{Cr} , 2130.0 K), respectively, are tabulated in Table 5.2.

Melting is not observed with a single pulse at the fluence of 0.6 J/cm^2 , as can be seen in Fig. 5.2. After a single pulse at the fluence of 0.9 J/cm^2 , aluminum melts only partially, whereas, chromium does not melt at all. At both values of the fluence, ablation has been observed in both aluminum and chromium films. Hence it is evident that for ablation to

Table 5.2: Times, in nanoseconds, taken for the surface and interface temperatures of aluminum and chromium coatings to reach the fusion temperatures of the metals, when irradiated with a 100 μm spot size laser beam at the fluences of 0.6, 0.9 and 1.3 J/cm^2 .

Fluence (J/cm^2)	Time (ns)					
	Aluminum coating			Chromium coating		
	0.6	0.9	1.3	0.6	0.9	1.3
Top surface	> 20 ns	8.4 ns	5.9	> 20 ns	> 20 ns	7.4
Coating-glass interface	> 20 ns	> 20 ns	6.5	> 20 ns	> 20 ns	13.1

Table 5.3: Maximum temperatures reached in the metal films after irradiation by a single pulse. The temperatures are calculated at the fluences of 0.6, 0.9 and 1.3 J/cm^2 , using numerical simulations (Case I, at the metal-glass interface) and heat balance calculations (Case II).

Fluence (J/cm^2)	Maximum temperature (K)					
	Aluminum coating			Chromium coating		
	0.6	0.9	1.3	0.6	0.9	1.3
Case I. Simulation	830	928	931	1576	2029	2309
Case II. Heat balance	836	933	933	1476	2049	2130

set in, the fusion temperature in the material need not be reached. In this case, the ejected solid fragments continue to be irradiated by the laser pulse, and may melt/vaporize mid-air. The molten and vaporized material that is ejected from the surface of the film or from the solid pieces, shields the underlying material from the remaining laser pulse (Toth et al. (1995)). Hence complete melting (or absence of solid ejection) is not observed except at

very high fluences. At the fluence of 1.3 J/cm^2 , aluminum and chromium are shown to melt completely after 6.5 ns and 13.1 ns, respectively. The maximum temperatures reached in the metal films after irradiation by a single pulse are mentioned in Table 5.3. The temperatures are calculated at the fluences of 0.6, 0.9 and 1.3 J/cm^2 , using numerical simulations and heat balance calculations. The values of the theoretically and numerically calculated temperatures are close to each other, thereby validating the numerical model.

Aluminum film machining

Figure 5.2 shows the plots of edge roughness and channel width vs. fluence for $100 \mu\text{m}$ wide channels machined. For the case of the plain aluminum film, it is observed from Fig. 5.2(a) and 5.2(c) that both edge roughness and channel width increase with fluence. This is non-intuitive unlike the case of the dependence of ablation rate on fluence. Higher fluence leads to quicker heating of the film and the glass substrate, thereby leading to a greater buildup of the ejection pressure (refer Sec. 1.8). The higher ejection pressure not only ejects the metal film directly above, but it also gets dissipated sideways, thereby causing the surrounding non-irradiated film to be torn and ejected out. The irradiated film gets ejected into solid pieces, carrying away with itself the torn regions of the film from the surroundings. The maximum roughness and widths obtained with the chosen machining parameters are $63.8 \mu\text{m}$ and $371.9 \mu\text{m}$ respectively, indicating a maximum lateral overcut of 272%.

Figure 5.3 shows the factors acting behind the ablation of aluminum film. The ablation is schematically shown in Fig. 5.3(a) where a large overcut is shown for a single pulse. With lateral overcut of the order of the intended width, the overlapping portion of the subsequent pulse does not encounter any metal. Hence, pulse overlap does not affect the channel width or the roughness. The contribution of overlap towards the channel width and roughness is insignificant, as can be seen from Fig. 5.3(b). Figure 5.3(c) shows the response surface of the channel width, as a function of fluence and overlap. The optimum values of fluence and spot

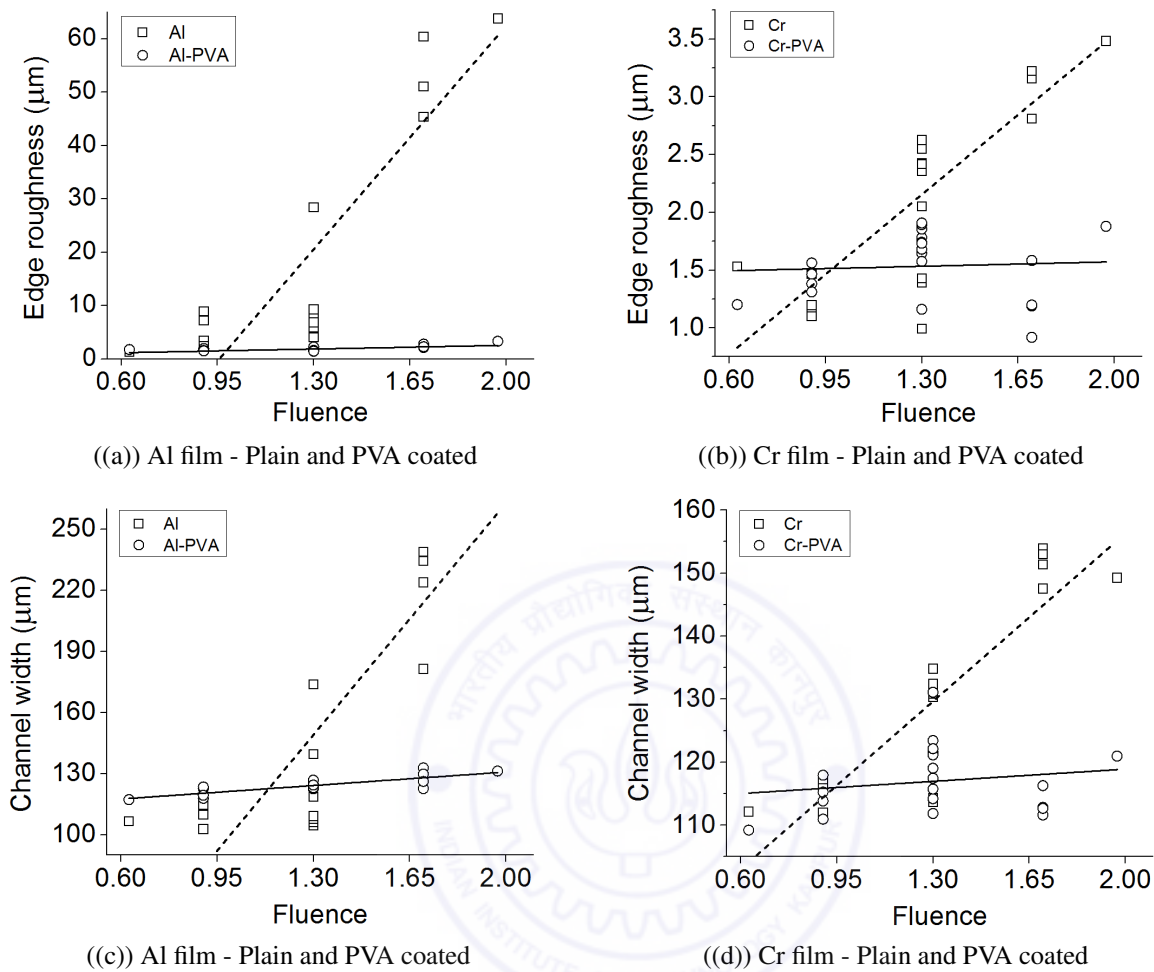


Figure 5.2: Plot showing variation of edge roughness and channel width (of 100 μm channels) with fluence for uncoated and PVA coated aluminum and chromium films. The lines show the linear trend. Dotted line is for uncoated metal film, whereas solid line represents polymer coated metal film.

overlap for obtaining minimum width and roughness are $0.9(\pm 0.1) \text{ J/cm}^2$ and $30(+1,-10)\%$ respectively [Akhtar et al. (2013b)].

Chromium film machining

Figures 5.2(b) and 5.2(d) show the plots of edge roughness and channel width as a function of fluence and overlap for 100 μm channels machined on chromium film on glass. Both the

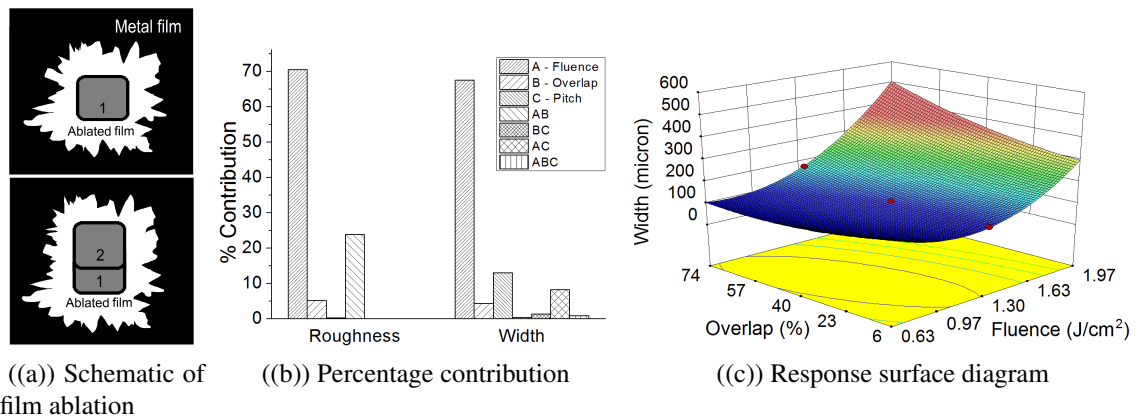


Figure 5.3: Schematic diagram of aluminum film ablation by one and two pulses (left), the relative contribution of various machining parameters towards edge roughness and channel width (center, all parameters shown are significant, with p value less than 0.01) and the response surface for the channel width (right)

edge roughness and channel width are found to increase with fluence. The maximum roughness and channel width are $3.5 \mu\text{m}$ and $153.9 \mu\text{m}$ respectively. These values are considerably smaller than those in aluminum film, implying a much cleaner ablation in chromium. There are two reasons for this observation. First, chromium has much better adhesion to glass compared to aluminum, and hence it takes larger ejection pressure to eject out the non-irradiated film. Second, the high volume specific heat of chromium causes a slower rise in temperature as compared to that in aluminum (refer Fig. 5.1). Hence, a large ejection pressure is probably not built up.

It is observed that edge roughness and channel width have little dependence on the spot overlap. Both responses are, in fact, randomly distributed. This can be explained with two reasons. First, the metal film undergoes single shot ablation (recall that the thickness of the film is an order of magnitude smaller than the thermal diffusion depth), and the area over which the spot overlaps does not see any metal film (refer Fig. 5.4(a)). Figure 5.4(b) shows the contribution of various factors to channel width and roughness. Fluence is the single most important factor influencing the response. Overlap has a limited impact on roughness as high

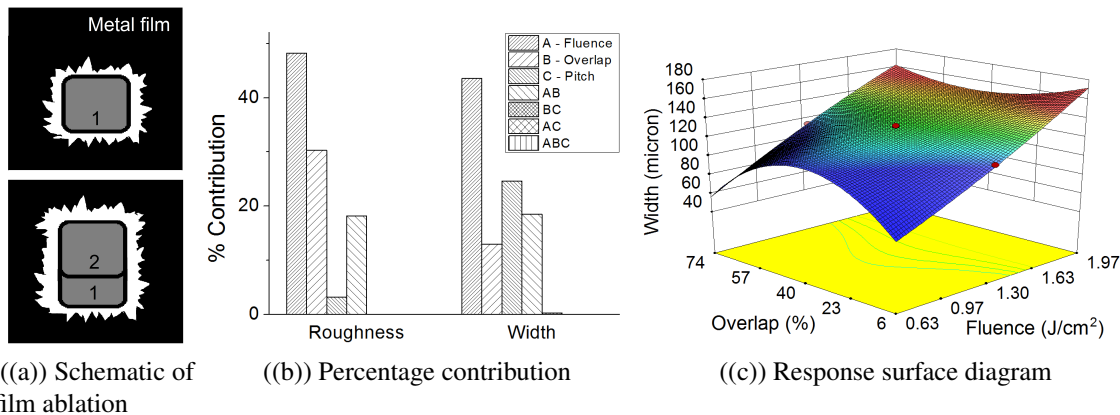


Figure 5.4: Schematic diagram of chromium film ablation by one and two pulses (left), the relative contribution of various machining parameters towards edge roughness and channel width (center, all parameters shown are significant, with p value less than 0.01) and the response surface for the channel width (right)

overlaps tends to disturb the boundary profile of the channels, ablating corners protruding into the channel. Second, the overlapping spot falls on the glass substrate, which does not conduct any heat to the non-irradiated film due to its poor thermal conductivity, and hence, does not significantly affect the channel width. Figure 5.4(c) is the response surface of the channel width, as a function of fluence and overlap. The optimum values of fluence and spot overlap for obtaining minimum width and roughness are 0.9 J/cm^2 and 20% respectively.

As the maximum widths obtained for channels machined in aluminum ($372 \mu\text{m}$) and chromium ($158 \mu\text{m}$) are much higher than the design width ($100 \mu\text{m}$), this process is not found to be suitable for fabrication of lithographic masks, miniaturized circuits or metamaterials. This calls for a novel intervention in the process that will allow machining of features with sizes closer to the desired dimensions.

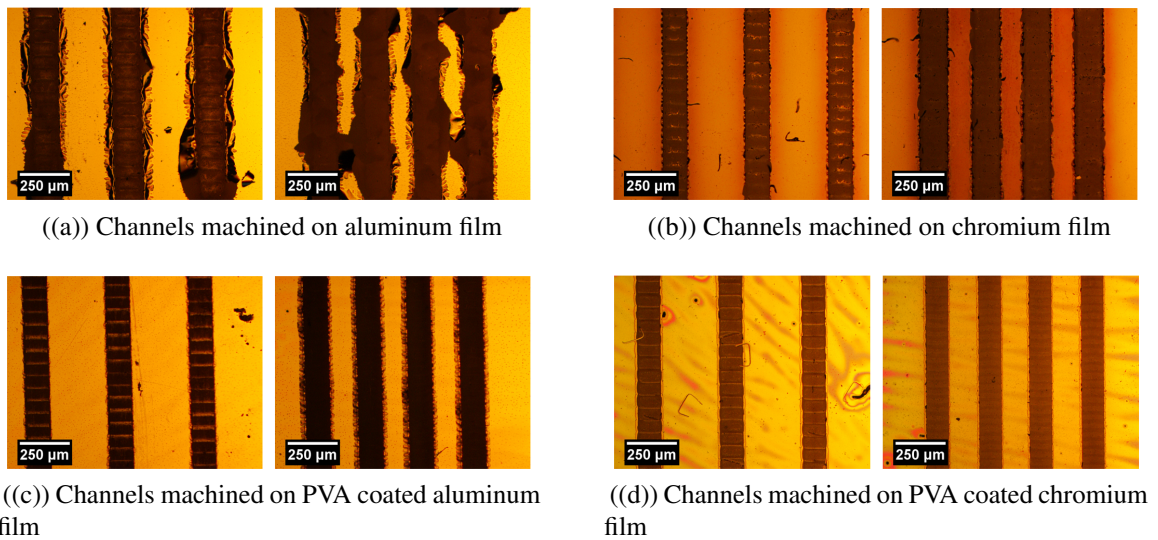


Figure 5.5: Optical micrographs of channels machined on aluminum (left) and chromium (right) films on glass, both with (bottom) and without (top) PVA coating. In each of the four blocks, the channel on the left has been machined at the fluence of 1.3 J/cm^2 and $300 \mu\text{m}$ pitch with 40% spot overlap. The channel on the right has been machined at the fluence of 1.7 J/cm^2 and $150 \mu\text{m}$ pitch with 60% spot overlap.

5.2.2 Machining of polymer coated metal films

Machining after coating metal films with a polymer film was carried out. This process was developed to grossly improve the quality of the laser micromachining of metal films. Micrographs of some of the machined channels are shown in Fig. 5.5. In this figure, the four images on the top indicate channels machined on the metal film, whereas the four images on the bottom are for channels machined in polymer coated metal film, under identical machining conditions. From the figures it is amply evident that machining a metal film after coating it with a polymer produces a drastic improvement in the quality of the machined features. While we quantitatively analyze the features a little later, it is rather important to discuss the related issues here.

It is well known that chromium adheres more strongly to glass as compared to aluminum [Jensen (2004)]. Aluminum, in fact, not only has poor adhesion, but is also a soft metal,

with a low melting point. The combination of these three factors make aluminum thin films highly prone to peeling/delamination and getting scratched. It is no surprise, then, that while machining aluminum thin films, much lateral ablation is observed, the reasons for which have been discussed earlier. It is worthy of note that machining aluminum film after coating it with a polymer improves the feature quality significantly, as observed from Fig. 5.5(c). The channels machined in polymer coated aluminum are quite similar to the ones machined in chromium film (see Fig. 5.5(b))

It will be premature to attribute the reasons for the improved feature quality to the effect the polymer layer has on the laser absorption in the metal film and the consequent rise in temperature. The optical absorption depth of the polymer for 248 nm wavelength ranges from 29 μm to 200 μm , depending on the molecular weight of the polymer [Attia and Elkader (2013); Shehap (2008); Mustafa (2013)]. In the worst case scenario, 96% of the laser intensity would be transmitted across the 1 μm thick polymer film. In fact, the 1 μm thick polymer layer gets ablated at the very beginning of the pulse, and does not significantly interfere with the incoming radiation. We do not expect the thickness of the polymer film to have a significant effect on the ablation characteristics of the metal film, as long as the thickness of the polymer film is less than about 5 μm . Hence we must look at the other effect that the polymer layer might have on the metal film, which is, its action as a clamping force that prevents the non-irradiated surrounding portions of the aluminum film from tearing and getting ejected at the slightest pressure buildup at the metal-glass interface. It is this clamping force that makes the polymer coated aluminum film behave similar to a chromium film. Strength of adhesion to the substrate, hence, is an important factor in high resolution patterning of metal films.

Figure 5.2 shows the plots of edge roughness and channel width (of 100 μm channels) versus fluence for PVA coated aluminum and chromium films. An immediate observation is that the edge roughness and the channel width have a stronger dependence on fluence

for polymer coated aluminum film compared to the polymer coated chromium film. The maximum roughness and width obtained in polymer coated aluminum film are $3.3 \mu\text{m}$ and $132.8 \mu\text{m}$ respectively, while those in polymer coated chromium film are $1.9 \mu\text{m}$ and $131.1 \mu\text{m}$ respectively. With similar maximum widths being obtained for both cases, it is assumed that ideal ablation occurs in these cases, one with the minimum overcut or lateral ablation. The polymer coating with good tensile properties serves a good clamping device in this respect.

The edge roughness obtained in the two cases need further understanding. Chromium films (chromium being a refractory metal under the wider definition that includes all elements with a melting point greater than or equal to 2123 K), have been reported to undergo cracking during irradiation with excimer lasers at fluences lower than the threshold for plasma formation, irrespective of the film getting ablated or not [Matthias et al. (1995)]. The cracks get smaller as the fluence is increased. The fine cracking at higher fluence allows finer pieces of chromium to be ejected from the boundary (as well as the interior) giving a smoother profile. Aluminum films are much more uniform with large grain sizes. Absence of cracking in aluminum films allows even larger pieces to be ejected from the surrounding regions near the channel boundary, generating a rougher profile. Hence, we obtain a higher maximum edge roughness in case of polymer coated aluminum film ($3.3 \mu\text{m}$) compared to that in polymer coated chromium film ($1.9 \mu\text{m}$).

With the ability to obtain edge roughness within $2 \mu\text{m}$ demonstrated with polymer coated chromium films, we analyze the sizes of the patterns usually machined on metal films for use in metamaterial and plasmonic devices. Ravirajan et al. (2005) fabricated Au electrodes on hybrid multilayer polymer-porous metal oxide photovoltaic devices by using shadow deposition. The electrodes had characteristic dimensions of the order of $10 \mu\text{m}$. Electrically coupled ring resonators and the crosses, having characteristic dimensions of the same order [Smith et al. (2004)], were fabricated using negative lithography and liftoff by Landy et al.

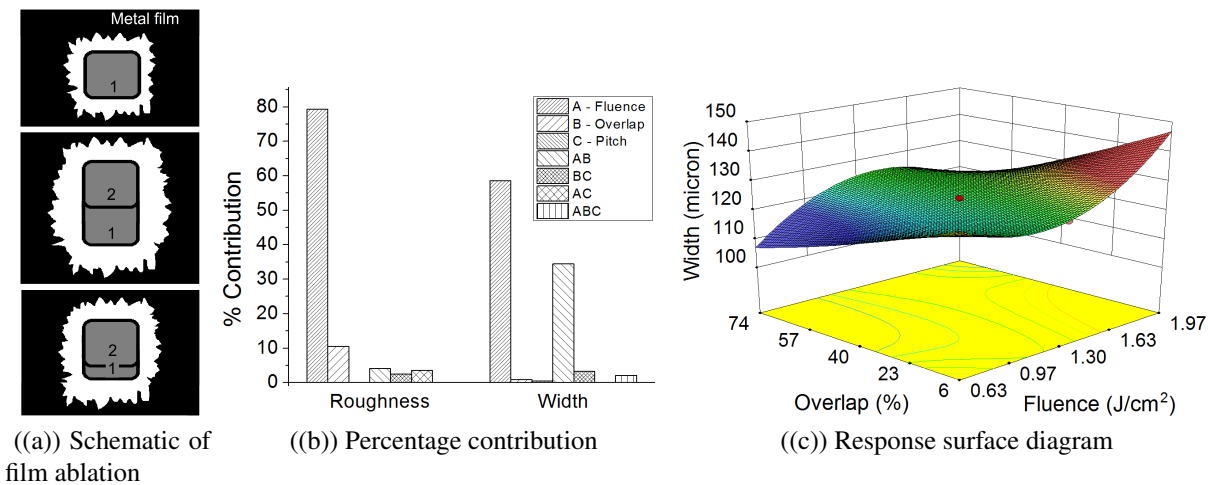


Figure 5.6: Schematic diagram of PVA coated aluminum film ablation by one and two pulses (left), the relative contribution of various machining parameters towards edge roughness and channel width (center, all parameters shown are significant, with p value less than 0.01) and the response surface for the channel width (right)

(2009). Terahertz pulse shaping devices were fabricated by Agrawal et al. (2005) by making apertures and grooves on metal foils by chemical etching. The sizes of the apertures and grooves were of the order of $100 \mu\text{m}$. Nagpal et al. (2009) used template stripping to form a smooth and patterned gold film for use as a plasmonic device. Template stripping is a complex process comprising substrate patterning by focussed ion beam machining or chemical etching, metal deposition by thermal evaporation, epoxy coating and then lift-off to generate the patterned metal surface. Shelby et al. (2001) fabricated a device with a left handed material to verify the existence of the negative index of refraction. The device consisted of split ring resonators and wires etched onto fiber glass circuit boards using shadow mask and etching. Each of the devices mentioned above employed a series of wet processing for its fabrication. The patterns required in these devices, if machined using excimer laser post polymer coating, can be obtained in a shorter time and over larger areas (since excimer laser machining allows workpiece scanning) without the use of etchants.

The spot overlap has different degrees of influence on the edge roughness and channel width, depending on the fluence. In case of polymer coated aluminum film, a close to ideal ablation is observed at low fluence. Any overlapping pulse sees unablated material in its vicinity. Hence, overlap serves to increase the channel width. On the other hand, high fluence pulses cause considerable lateral overcut. Hence, only pulses with low overlap can see a considerable amount of unablated material. Therefore, larger channel width is observed for low overlap pulses, and vice versa. Hence the effect of spot overlap depends on the level of fluence. The spot overlap contributes to the channel width not as an independent factor, but interactively with the fluence, as can also be seen from Fig. 5.6(b). The spot overlap is not found to have any significant effect on edge roughness, an observation similar to that in case of aluminum film, and attributed to excessive lateral ablation. Figure 5.6(c) shows the response surface of the channel width as a function of fluence and spot overlap for polymer coated aluminum film. The optimum values of fluence and spot overlap for obtaining minimum width and roughness are 0.9 J/cm^2 and $56.6(\pm 0.3)\%$ respectively.

Spot overlap has a much stronger influence on the channel width for polymer coated chromium film. Being the most difficult to remove film out of the four cases considered here, it gets machined to the closest to ideal size (refer Fig. 5.7(a)). Hence any overlapping pulse finds unablated material in its vicinity and thereby increases the channel width. The degree of its effect does not depend on the level of fluence, and it appears as an independent factor, as seen in Fig. 5.7(b). The spot overlap does not significantly affect the roughness, nor does the fluence. These, hence, appear as almost equal contributors to the edge roughness. The overlap does not appear as an independent factor because its effect is more pronounced at lower fluence. Figure 5.7(c) shows the response surface of the channel width as a function of the fluence and spot overlap, for polymer coated chromium films. The optimum values of fluence and spot overlap for obtaining minimum width and roughness are 0.9 J/cm^2 and $40.0(\pm 0.4)\%$ respectively.

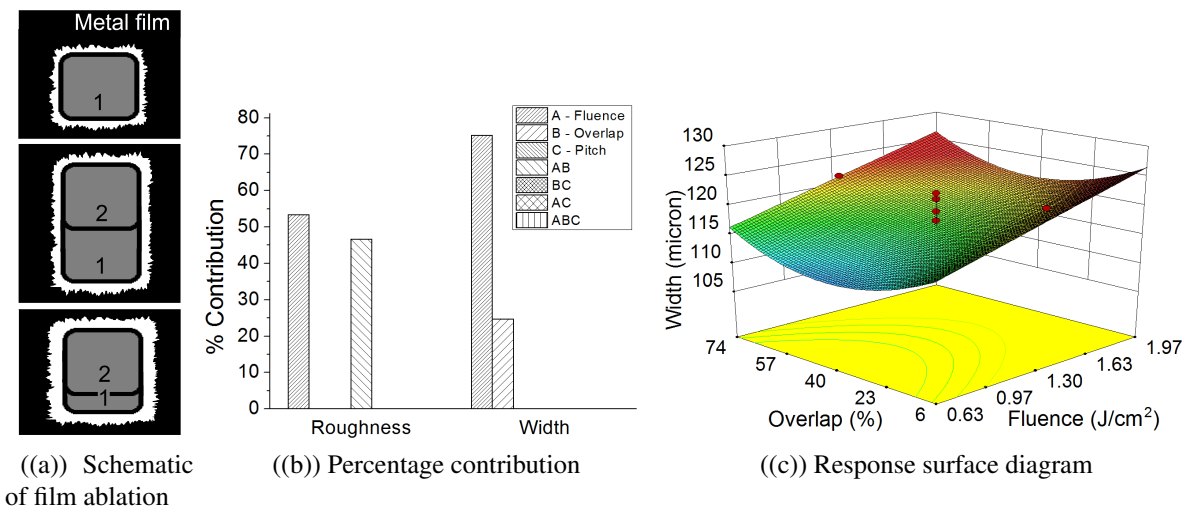


Figure 5.7: Schematic diagram of PVA coated chromium film ablation by one and two pulses (left), the relative contribution of various machining parameters towards edge roughness and channel width (center, all parameters shown are significant, with p value less than 0.01) and the response surface for the channel width (right)

The integrity of the boundary is a qualitative (categorical) response. The integrity is ranked on a scale of 1 to 5, with 5 for the completely solid (integrated) boundary between adjacent channels and 1 for the completely destroyed (ablated) boundary. An example of two such channels, machined on aluminum, with ranks 5 and 1 are shown in Fig.5.8. The pitch (or

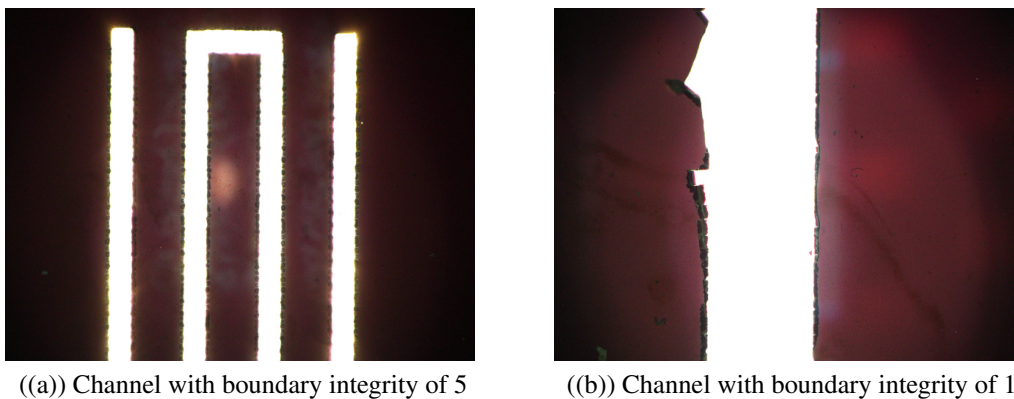


Figure 5.8: Example of boundary integrity of channels, with completely preserved (integrated) boundary in 5.8(a) and completely destroyed (ablated) boundary in 5.8(b)

from each other, higher the probability that the boundary will be preserved. Its dependence on fluence is through the channel width. As long as the channels are narrow and far enough so that their boundaries do not touch, the boundary integrity is maintained.

5.3 Results and discussion for oblique channels

Fabricating devices, such as the ones mentioned in the preceding paragraphs, often requires fabricating curved features, such as circular pads, and interconnects. In order to achieve sharp corners, a square or rectangular mask is often used to produce a projected and demagnified laser spot with sharp features. This, however, causes difficulty in making oblique or curved features where the axis of traverse of the laser spot does not align with the edges of the square/rectangular spot. The produced line or feature has a rough or serrated edge due to successive pulses falling on displaced areas. In such a case, the factors that determine the quality of the feature, are the spot overlap and the angle of tilt in addition to the laser fluence. Spot overlap is a measure of the area that is common to two consecutive laser spots. The angle of tilt is a measure of the lateral offset of successive laser spots from a straight line. Using these three factors, experiments are conducted to fabricate oblique microchannels. The microfeatures are characterized for their edge roughness and channel width. The polymer coated metal films are shown to be machined with sharp boundaries in comparison to uncoated metal films.

5.3.1 An ideal oblique microchannel

Figure 5.11 shows the schematic diagrams of channels tilted at various angles and with varying spot overlaps. One of the first observations from the schematic diagrams shows that with variation in fluence, the diagram does not change. Hence, fluence does not affect the edge roughness and channel width of an ideal channel. Figures 5.11(a) and 5.11(c) show chan-

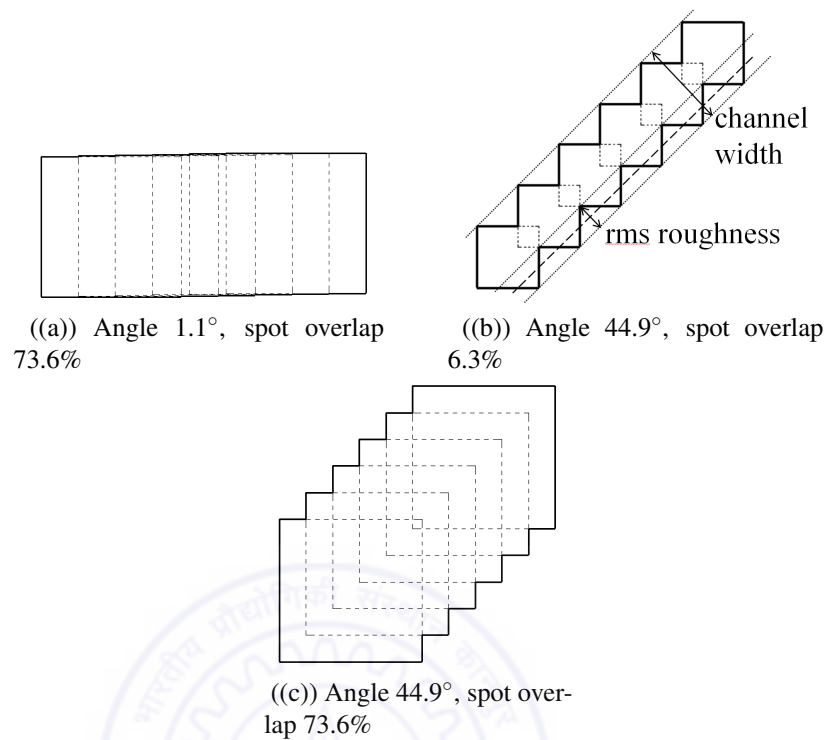


Figure 5.11: The schematic diagrams of oblique microchannels fabricated at different angles and spot overlaps. The edge roughness increases with angle and decreases with spot overlap. The channel width only depends on the angle of tilt, and increases with it.

nels made at same spot overlap (73.6%). Comparing the two, it is obvious that the channel machined at greater angle has a higher edge roughness and higher width. Hence edge roughness and width increase with the angle of tilt. Similarly, comparing channels in Fig. 5.11(b) and 5.11(c), both of which are machined at the same angle of tilt, it can be inferred that the edge roughness increases with decrease in spot overlap, and the channel width remains independent of the spot overlap.

5.3.2 Aluminum film machining (without and with polymer coating)

A thorough study on the direct ablation of aluminum film while making $100\ \mu\text{m}$ wide straight channels, with their axes parallel to the edges of the square spot, has been presented in

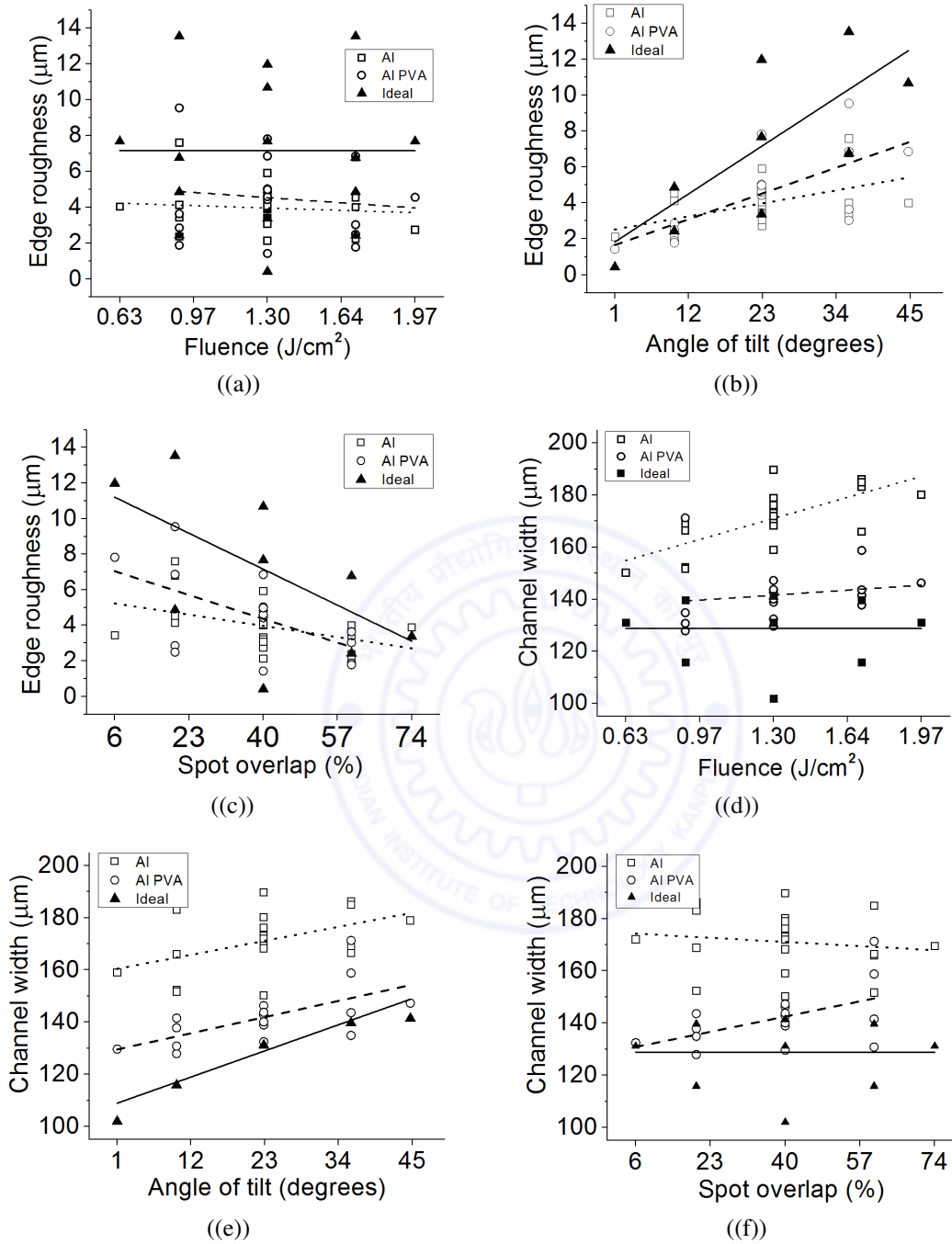


Figure 5.12: Plot showing variation of edge roughness and channel width (of $100 \mu\text{m}$ channels) with fluence, angle and overlap, for uncoated and PVA coated aluminum. The lines show the linear trend. Dotted line is for uncoated metal film, dashed line is for polymer coated metal film, whereas solid line represents the ideal variation.

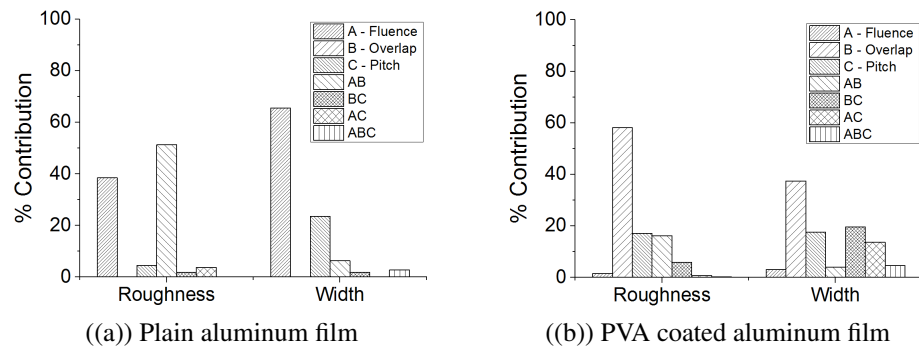


Figure 5.13: Contribution of various factors to edge roughness and channel width of oblique channels machined in plain (left) and PVA coated (right) aluminum films

Ref. [Akhtar et al. (2013b)]. Here, we discuss the feature quality of oblique microchannels. Figure 5.12 shows the variations of edge roughness and channel width with fluence, angle and overlap, for $100\ \mu\text{m}$ wide channels. As seen in the figures, the ideal roughness, denoted by the solid line, is independent of the fluence, and it increases with angle and decreases with overlap. This has been discussed in the preceding subsection. For the case of the plain aluminum film, denoted by the dotted lines, it is observed from Fig. 5.12(a) that roughness remains fairly unaffected by fluence. If we were to consider the effect of fluence alone, the roughness actually increases with fluence. This is due to development of larger ejection pressures at higher fluences, that also gets dissipated sideways and causes ejection of both radiated and the surrounding irradiated portions of the metal film. Aluminum is known to undergo large lateral ablation, with lateral overcut of the order of the intended width [Akhtar et al. (2015. In press.)]. This is a result of poor adhesion of aluminum to glass [Jensen (2004)], softness, low melting point of aluminum and outgassing from the glass substrate. The combination of these three factors make aluminum thin films highly prone to peeling/delamination and getting scratched. Aluminum films are much more uniform with large grain sizes. Absence of grain boundaries in aluminum films allows large pieces to be ejected from the surrounding regions near the grain boundary, generating a rougher

profile. However, interactive effects of fluence and overlap cause the roughness to decrease. Hence, the two factors, fluence as an independent factor, and fluence-overlap interaction, have opposing effects on the roughness and tend to negate the effects of each other. This is evident from Fig. 5.13(a), where both the above mentioned factors have almost equal contributions to the edge roughness, albeit in opposite senses.

Edge roughness, ideally and actually, decreases with increasing overlap, as shown in Fig. 5.12(c). (This is unlike the ablation of straight channels, where overlap has little role to play, even in interaction with other factors.) At high overlap, the successive pulses see little unablated material. Hence additional ablation by a pulse is small, leading to lower roughness. However, it is to be noted that overlap does not affect the roughness independently (refer Fig. 5.13(a)), rather only at small fluence. High fluence pulses cause such excessive ablation that even at small overlaps, successive pulses see little unablated material. Edge roughness increases with angle, as shown in Fig. 5.12(b). Such a response is expected, as at higher angles, successive pulses fall at higher offsets from the preceding ones. Referring to Figure 5.11, it can be seen that at higher angles (or offset), a pulse sees unablated material on all four sides. This leads to excessive ablation and hence increase in roughness. However, the contribution of the angle towards the edge roughness is significantly lower than those of fluence and overlap, as can be seen from Fig. 5.13(a).

The ideal width, as already discussed, does not depend on the fluence or overlap. However, we do see in Fig. 5.12(d) that the width of the channel increases with fluence (dotted line). This is attributable to the excessive lateral ablation in case of machining aluminum film directly, an observation already discussed in the preceding paragraphs. Understandably so, fluence is the most highly contributing factor towards channel width, as can be seen from Fig. 5.13(a). The channel width increases with angle (see Fig. 5.12(e)), quite like an ideal case. There is little variation observed in channel width with spot overlap (see Fig. 5.12(f)), reiterating the fact that excessive lateral ablation renders the extent of spot overlap

polymer coated aluminum films is always higher, and the channel width, lower, compared to that of channels machined in plain aluminum films. This is similar to the case of ideal channels, which have the highest roughness and the lowest width of the three. The maximum edge roughness and channel width obtained in the case of PVA coated aluminum film with the chosen machining parameters are $9.5 \mu\text{m}$ and $171 \mu\text{m}$ respectively.

The improvement in feature quality cannot be attributed to the interaction of the polymer layer with the laser pulse. This is because the $1 \mu\text{m}$ thick polymer layer gets ablated within a few nanoseconds of the beginning of the pulse [Akhtar et al. (2015. In press.)]. It is the action of the polymer layer as a clamping force that prevents the non-irradiated surrounding portions of the aluminum film from tearing and getting ejected at the slightest pressure buildup at the metal-glass interface. Indirectly, the polymer layer keeps the aluminum film adhered to the glass surface. Strength of adhesion to the substrate, hence, is an important factor in high resolution patterning of metal films.

5.3.3 Chromium film machining (without and with polymer coating)

Chromium films (chromium being a refractory metal [Akhtar et al. (2015. In press.)]), undergo cracking during irradiation with excimer lasers [Matthias et al. (1995)]. Cracking occurs irrespective of the film getting ablated or not. The cracks get smaller as the fluence is increased. The fine cracking at higher fluence allows finer pieces of chromium to be ejected from the boundary (as well as the interior), allowing cleaner ablation.

Figure 5.15 shows the plots of edge roughness and channel width versus fluence, spot overlap and angle of tilt, for $100 \mu\text{m}$ channels machined on chromium film on glass, both with and without polymer coating. Considering the case of plain chromium film only, the edge roughness remains independent of fluence, increases with angle and decreases with overlap. The channel width increases with all the three factors. All responses, except one, are similar to those of plain aluminum film. The width increases slightly with overlap, unlike

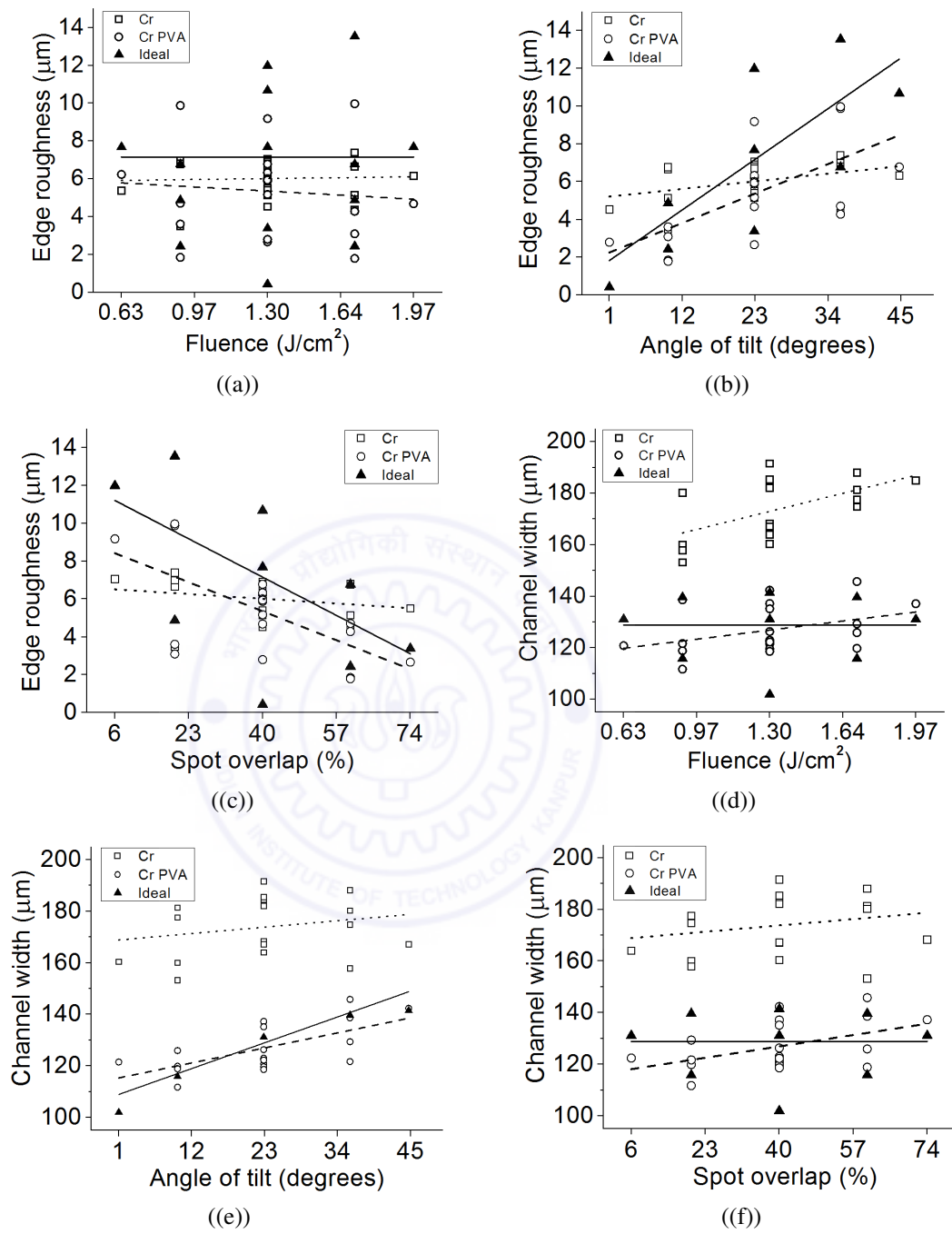


Figure 5.15: Plot showing variation of edge roughness and channel width (of 100 μm channels) with fluence, angle and overlap, for uncoated and PVA coated chromium films. The lines show the linear trend. Dotted line is for uncoated metal film, dashed line is for polymer coated metal film, whereas solid line represents the ideal variation.

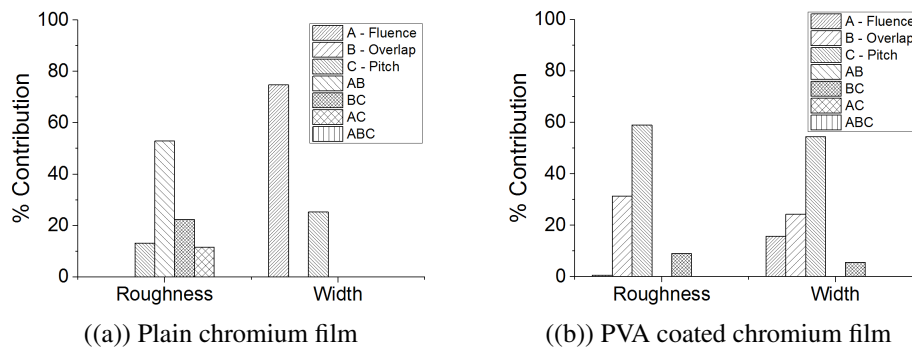


Figure 5.16: Contribution of various factors to edge roughness and channel width of oblique channels machined in plain (left) and PVA coated (right) chromium films

the case of plain aluminum film. It is, in fact, similar to the case of PVA coated aluminum film. The reason for this is the absence of excessive lateral ablation due to good adherence of chromium film to glass and fine cracking upon irradiation. Larger ejection pressure is required to eject out the non-irradiated film when adherence to the substrate is high. Additionally, lesser ejection pressure is built up in this case because of the high volume specific heat of chromium that causes a slower rise in temperature as compared to that in aluminum. Fluence and overlap, interactively, are significant contributors to roughness (refer Fig. 5.16(a)). Fluence and angle contribute most towards the channel width. The maximum edge roughness and channel width obtained in the case of chromium film with the chosen machining parameters are $7.4 \mu\text{m}$ and $192 \mu\text{m}$ respectively.

Figure 5.17 shows optical micrographs of some of the oblique channels machined in, both, plain and PVA coated chromium films. Similar to the observation for aluminum films, micromachining post polymer coating gives a significant improvement in feature quality. Features in PVA coated metal film are sharply machined with enhanced edge quality. The variations in edge roughness and channel width as functions of the machining parameters are similar to those of polymer coated aluminum films. However, unlike the case of polymer coated aluminum film where spot overlap contributed most significantly to the edge rough-

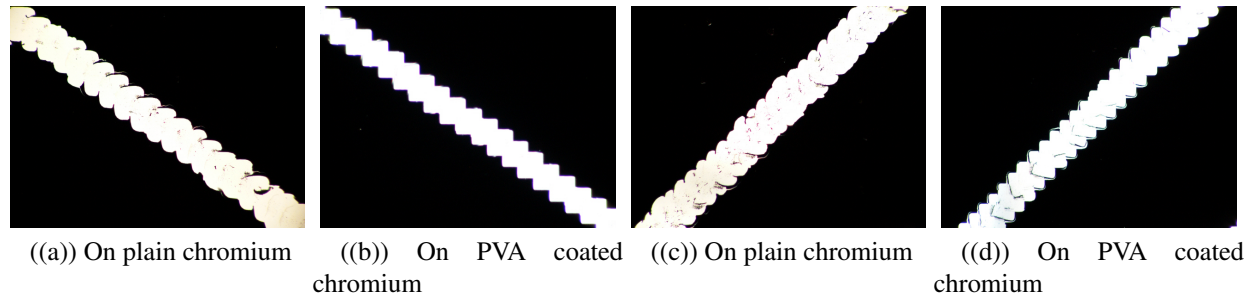


Figure 5.17: Optical micrographs of some $100 \mu\text{m}$ wide oblique channels machined in chromium, without (a & c) and with polymer coating (b & d). Channels a & b are machined at 0.9 J/cm^2 , 36° and 20% spot overlap. Channels c & d are machined at 1.3 J/cm^2 , 44.9° and 40% spot overlap.

ness and channel width, in case of polymer coated chromium film, angle of tilt is the most significant factor, and spot overlap comes second. This is much closer to the response of an ideal channel. Unlike polymer coated aluminum films, in case of chromium films, the roughness of both coated and plain films are close to each other. The channel width, however, like the former, is always lower for polymer coated chromium film compared to that of plain chromium film. The maximum edge roughness and channel width obtained in the case of chromium film with the chosen machining parameters are $10.0 \mu\text{m}$ and $146 \mu\text{m}$ respectively.

5.4 Conclusions

Laser machining is being used to fabricate integrated circuits by ablation of metallic films. It is then imperative to understand how the microfeature quality, and most importantly the microfeature edge quality, responds to changes in machining parameters. The effect of three such machining parameters on edge quality have been studied in this work. A set of machining experiments have been carried out on uncoated and polymer-coated aluminum and chromium films, coated on a glass substrate. $100 \mu\text{m}$ wide straight and oblique channels

have been fabricated by excimer laser micro machining using a square laser spot. Metal films have been observed to ablate at fluences much lower than the ablation threshold, and often before the onset of melting.

For the case of straight channels, the edge roughness and channel width have been found to be majorly dependent on the fluence used, and little affected by the spot overlap. The pitch (distance between adjacent channels) is found to influence the boundary integrity and is recommended to be kept as large as possible relative to the width of the channels being machined. Better feature quality has been observed while machining chromium compared to aluminum, an observation primarily attributed to the strong adhesion of chromium films to the glass substrate. Secondly, the higher volume specific heat of chromium, vis a vis aluminum, allowed a slower rise in temperature and also the build-up of ejection pressure. The spot overlap does not significantly affect the feature quality. The feature quality obtained after machining polymer coated metal films shows considerable improvement. The action of the polymer film as a clamping force prevents large pieces of non-irradiated metal film from getting ejected, leading to a smoother edge and smaller channel width. With polymer coating, smoother channels are generated on chromium films as compared to aluminum films. Cracking of chromium films upon irradiation leads to ejection of fine pieces, thereby giving a lower edge roughness.

For the case of oblique channels, the edge roughness has been found to be little affected by the fluence, very unlike the case of straight channels. The edge roughness, in all cases, has been found to increase with the angle of tilt and decrease with the spot overlap. Owing to the strong adhesion of chromium films to the glass substrate, the roughness of the channels machined in chromium is more than that in case of aluminum films, an observation contrary to the case of machining straight channels.

In case of plain metal films, the interaction of fluence and spot overlap most significantly affected the edge roughness, whereas spot overlap and angle of tilt were the most significant

factors in determining edge roughness for polymer coated metal films. (It is relevant to mention here that spot overlap does not affect the edge roughness of straight channels machined in polymer coated metal films.) In this regard, polymer coated metal films underwent close to ideal ablation, little affected by fluence. Hence, polymer coating created a clamping force preventing large pieces of non-irradiated metal film from getting ejected, leading to a sharp ablation and improved feature quality.

The channel widths, in all cases, were observed to increase with fluence and angle of tilt. Spot overlap had little effect on channel width. High fluence causes excessive lateral ablation, thereby increasing the channel width. The extent of overcut, however, is less in polymer coated metal films compared to that in plain metal films. Because of sharp and close to ideal ablation in polymer coated metal films, the widths of channels machined in such films are always lower compared to those in case of plain metal films.

We have demonstrated a novel technique of machining sharp curved features on thin metal films using a square laser spot. This technique helps in curtailing the edge roughness of the microfeatures to values less than $10\ \mu\text{m}$, when the ideally expected roughness is close to $13\ \mu\text{m}$. For oblique channels, the channel width has been demonstrated to be reduced to $150\ \mu\text{m}$ from $190\ \mu\text{m}$ by using a polymer coating. Ideally expected channel width is about $140\ \mu\text{m}$, which is close to the size of the square laser spot.

The developed fabrication technique has a huge potential for thin film patterning that can be used in cutting-edge MEMS technology and processes. This invention can be an alternative approach for the direct machining of the metal films for mass production of the MEMS, photonics devices, micro fluidic channels etc. This method can produce a new generation of high-precision patterned thin films for applications such as surface texturing for bio medical applications, heat transfer applications, for developing diffractive optical elements, photonic structured materials for future photonic communications devices, and metamaterial structures for infra-red materials, generating microstructure lumped elements for microwave

transmission lines and miniaturized microwave hybrid circuits. Specifically, the direct micro-machining of metal films is important for the board manufacturers, miniaturized microwave circuits for space and automobile industries as well as futuristic markets in terahertz devices and infra-red metamaterial devices and technologies.



Chapter 6

Fabrication of novel setups and structures

During the course of the work presented in this thesis, the learnings allowed fabrication of various kinds of microfeatures and development of setups useful for carrying out laser micromachining using mask projection. This chapter presents, as an assortment, the various features that have been fabricated, and the different setups that have been developed in the past few years. The study of the mask projection technique, coupled with the study on the excimer laser micromachining of polymers, allowed the fabrication of micro lens arrays, more on which is discussed in the following section. The requirement to fabricate complex and distributed features on a substrate allowed the fabrication of a device to automatically switch on and off the laser machine. Fabrication of microfeatures of varying shapes and sizes requires frequent change of masks, which is a tedious process. Hence a mask indexing setup was fabricated that allows simultaneous mounting of up to ten masks. Any particular mask may be used during the course of the micromachining process. Finally, several test patterns of miniaturized circuits were fabricated on different kinds of substrates to demonstrate the ability of the excimer laser micromachining technique to directly pattern the circuit elements.

6.1 Microlens arrays and their fabrication

In recent years the fabrication of micro lenses has gained attention of researchers. These micro lenses have found use in a plethora of components such as CCD arrays [Povel et al. (1997)], digital projectors, 3D imaging [Hess (1912)], and integral photography [Lippmann (1908)]. Moreover, current research indicates that array of micro lenses has the ability to act as concentrators for high efficiency photovoltaics [Karp et al. (2010)]. They are also used to couple light to optical fibers [Cohen and Schneider (1974)]. Therefore, the use of micro lenses in compact high performance micro optical devices has become essential. That is why, in the past decade, researchers have emphasized on deriving novel methods to fabricate lenses with lens diameters ranging from a few micrometers to few millimeters.

Thus, there is a growing need to establish a cost effective, less complex and efficient method to fabricate micro-lenses. For the past two decades, researchers have been exploring various methods to fabricate refractive micro lenses. Some research was based on glass based lenses, while the study on polymer based lenses has opened a whole new window of opportunities. The photo-resist reflow method [Popovic et al. (1988)], ultraviolet curing of polymer [Okamoto et al. (1999)], LIGA method [Sankur et al. (1995)], micro jet technique [MacFarlane et al. (1994)] and micro molding or hot embossing method [Ong et al. (2002)] are some such new techniques which are used to fabricate micro lenses. However, these methods suffer from poor surface quality of features that cannot be improved. Hence, the use of these methods is restricted to some extent. Excimer laser micro machining has an important role in the fabrication of polymer based micro lenses as it interacts via photo-chemical mechanism or the cold ablation mechanism and therefore the surface quality can be controlled accurately [Brannon (1990); Dyer and Sidhu (1985)]. The material is removed by laser ablation while the shape of the pattern is controlled by mask projection of laser source and the motion of a micro positioning stage.

For fabricating a 3-dimensional micro structure, one can use a photo mask which modulates the spatial laser intensity on the work piece, producing features of varying depth [Tien et al. (2003)]. Another method is known as contour mask scanning [Zimmer et al. (2000)], in which contour or mask opening is synchronized with sample movement to achieve depth variation.

Lee et al. (2005) have successfully fabricated axi-symmetric micro lens using a new approach termed as Planetary mask contour scanning method. In this method the mask revolves as well as rotates at the same time. The underlying principle is to create a probability distribution of laser intensity with the help of a self spinning mask which revolves around the sample producing axis symmetric feature. Authors have used 0.5 mm thick polycarbonate samples. According to the principle, the motion of the sample stage and mask revolution should be synchronized with laser firing sequence and before machining the mask center should be in alignment with the sample stage. Lee and Wu (2007) used this method to fabricate axis symmetric micro lenses of 200 μm aperture with high surface quality, i.e. surface roughness ranged from 3 - 6 nm.

Although several methods have been proposed over the years, but yet a systematic study and derivation of a less complex and accurate method is required. In this section, we present a systematic study of a fabrication process of micro lenses with excimer laser micromachining via use of a contour mask and work piece scanning.

6.1.1 Fabrication and analysis of masks

It is desired that spherical microlenses be fabricated with excimer laser micromachining using a contour mask. The cross-sectional view of the microlenses is shown in Fig. 6.1. The spherical microlenses have a circular cross-section, colored as gray, as shown in the figure. Consider two points in the cross-section, A and B. While fabricating the microlenses, point A does not need to be machined, whereas point B needs to be machined to the largest depth.

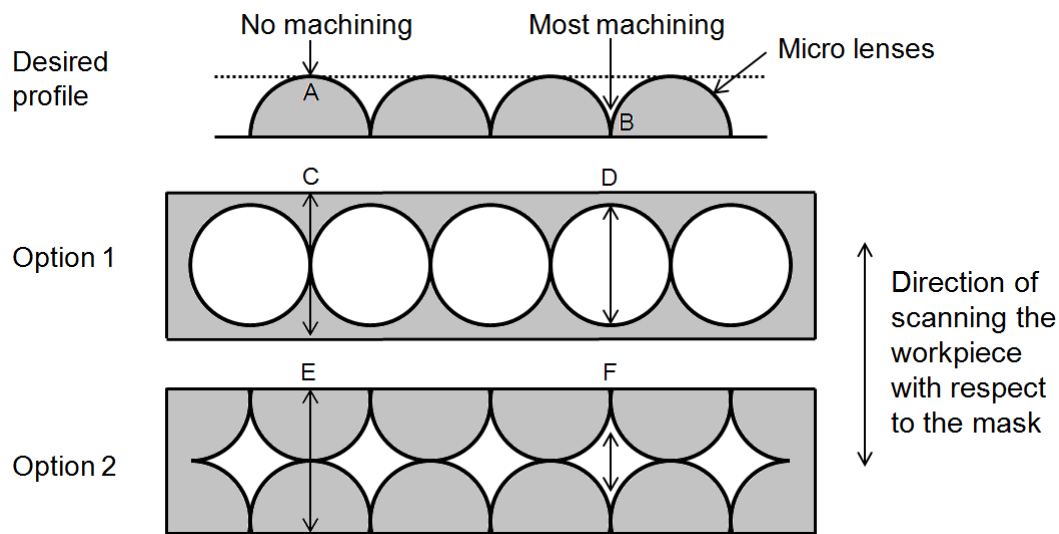
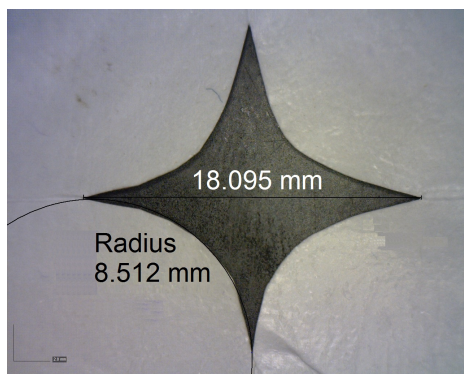
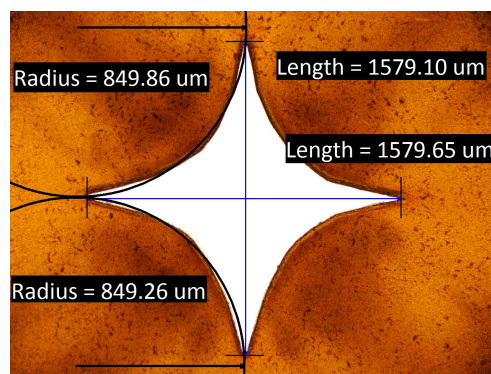


Figure 6.1: A schematic flowchart for deciding the mask shape for a desired profile of micro lenses (top). Two options for the masks are shown. The white regions in the designs of masks are transparent to the laser radiation.

Hence, in the binary mask to be designed, the opening in the mask should be minimum in the region corresponding to point A, and maximum in the region corresponding to point B. The opening in the mask need to have a second order variation, so as to obtain a circular profile. Two options of the probable mask designs are shown in Fig. 6.1. Points C and E correspond



((a)) First stage mask made in aluminum foil



((b)) Second stage mask machined in Kapton sheet

Figure 6.2: The optical photographs of the masks used to machine the micro lens arrays

to point A in the desired profile. Points D and F correspond to point B in the desired profile. Note that the opening in the mask is minimum at points C and D (because point A does not need to be machined), whereas it is the largest at points D and F (because point B needs to be machined to the largest depth). Since the design shown in the second option is easier to fabricate, it was chosen to serve as the binary mask for this microfabrication process.

The first stage mask was fabricated in a piece of aluminum foil, and is shown in Fig. 6.2. The profile of the mask was designed in a way that the exposed length is largest at the center and it reduces, by second order, towards the periphery. This allows the manufacture of two halves of a lens, with peaks at the periphery and valley in the middle. Note that the region that has a larger exposed length sees more number of pulses per spot, and hence experiences greater machining depth.

The maximum exposed lengths in the first and second stage masks are 18.095 mm and 1.579 mm respectively, which is a reduction of about 11.5X. Clearly, an overcut of about 12.7% is observed, which is expected in a laser machining process. The radius of the curved profile, has been reduced 10 times, as can be seen from Fig. 6.2.

6.1.2 Analysis of the microlens profiles

The cross-sectional micrographs of the various lenses are shown in Fig. 6.3. Arrays of 3×3 lenses have been fabricated and their profiles are measured and compared with the theoretical profile expected from machining in PMMA. Note that it is easy to extend the size of the array to 10×10 or 100×100 or even much larger arrays. The dimensions shown on the top of each figure (e.g. $70.0 \mu\text{m}$ in Fig. 6.3(a)) show the depth to which the entire array has been machined. This depth is compensated for when comparing these profiles with the theoretical profile.

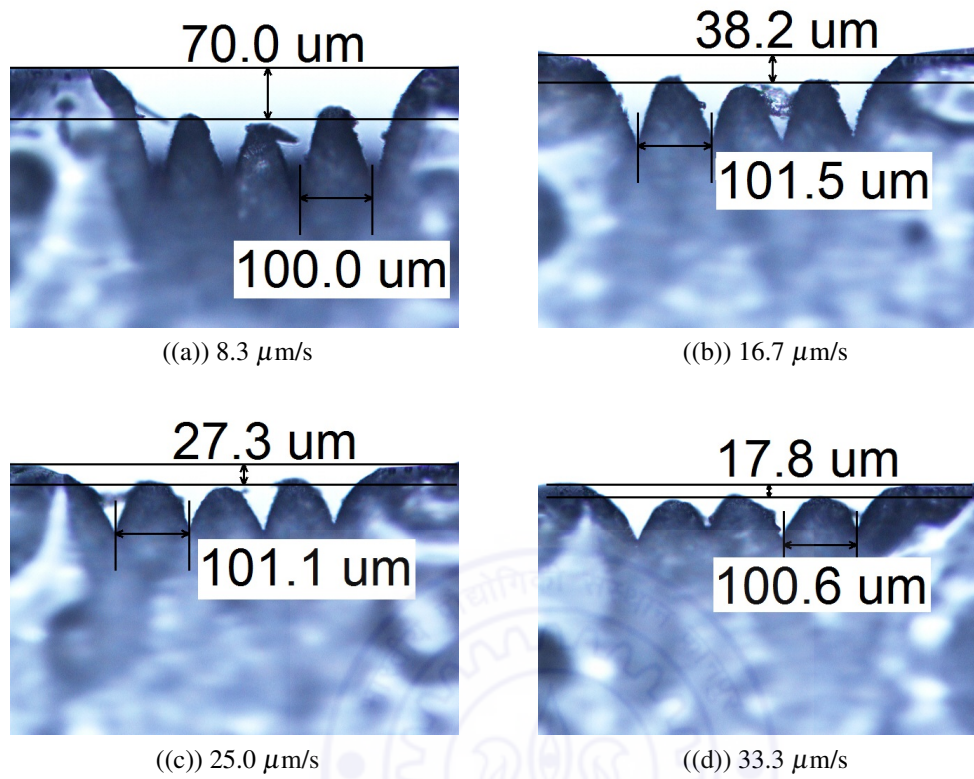


Figure 6.3: The optical micrographs of the cross-sections of the microlenses machined at various scanning speeds, with 176 mJ pulses and at 5 Hz. The adjacent lenses have been fabricated after indexing the workpiece by 100 μm . The images are acquired through a Dino-Lite USB microscope.

Measurement of ablation rate of PMMA

Basic experiments were conducted on PMMA to measure the depth of ablation. Depths were measured after machining with several pulses of laser at three different pulse energies (120, 175 and 225 mJ). It is important that these measurements are done with several pulses in PMMA, so that the incubation effects of photon absorption are compensated, and the ablation depth per pulse reaches a steady value (see Section 4.3.3). Fig. 6.4 shows the plot of ablation depth per pulse at the three different pulse energies, for varying number of pulses. As is widely reported, the etch depth per pulse varies linearly with the fluence. A value of 5.3 m/pulse is obtained for the pulse energy used (175 mJ). This value is used further to

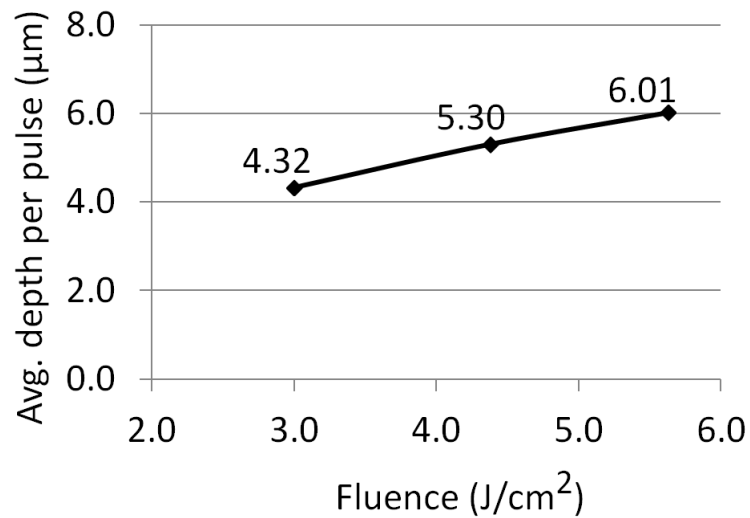


Figure 6.4: Ablation rates of PMMA with 248 nm pulsed excimer laser

determine the theoretical profile of the lenses machined on PMMA.

Calculation of the theoretical profile

In order to determine the theoretical profile of the lenses, it is important to determine the number of pulses that fall at each spot on the work piece. Larger number of pulses generates a greater depth. The number of pulses at a spot is determined by the scanning speed of the work piece (s), the repetition rate of the laser (r) and the feature size (exposed length, l), in the direction in which the work piece is being scanned.

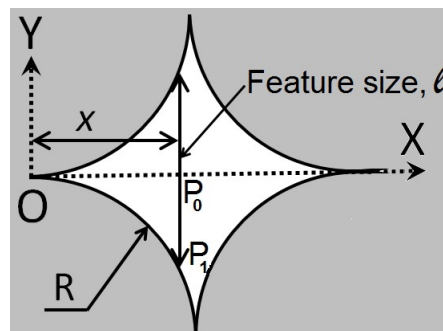


Figure 6.5: Schematic of the procedure to calculate the feature size (exposed length)

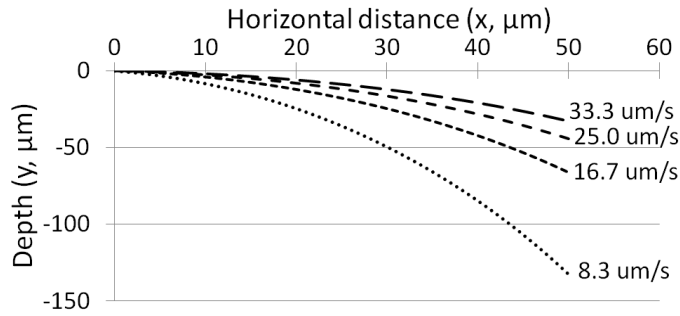


Figure 6.6: Theoretical profiles of lenses machined at different scanning speeds

The origin of coordinates is fixed at the point ‘O’ as shown in Fig. 6.5. The vertical distance to the bottom profile, from the horizontal axis, at a distance ‘x’ from ‘O’ is calculated (P_0P_1 , as shown in the figure). The feature size, or the exposed length, l , is then, twice of this distance, and is expressed as

$$l = 2(R - \sqrt{R^2 - x^2}). \quad (6.1)$$

If the distance moved by the stage in 1 second is ‘s’, then ‘s’ units of length see ‘r’ pulses in a second. Hence, the number of pulses per spot will be the number of pulses falling per ‘l’ units of length, and is expressed as

$$\text{pulses per spot} = \frac{r \times l}{s}. \quad (6.2)$$

The ideal depth of ablation is, then, given by,

$$\text{Ideal depth} = \text{pulses per spot} \times \text{ablation rate}. \quad (6.3)$$

The ideal depth of ablation helps to generate the theoretical profile of the lens. The theoretical profiles for all four cases of scanning speed are shown in Fig. 6.6.

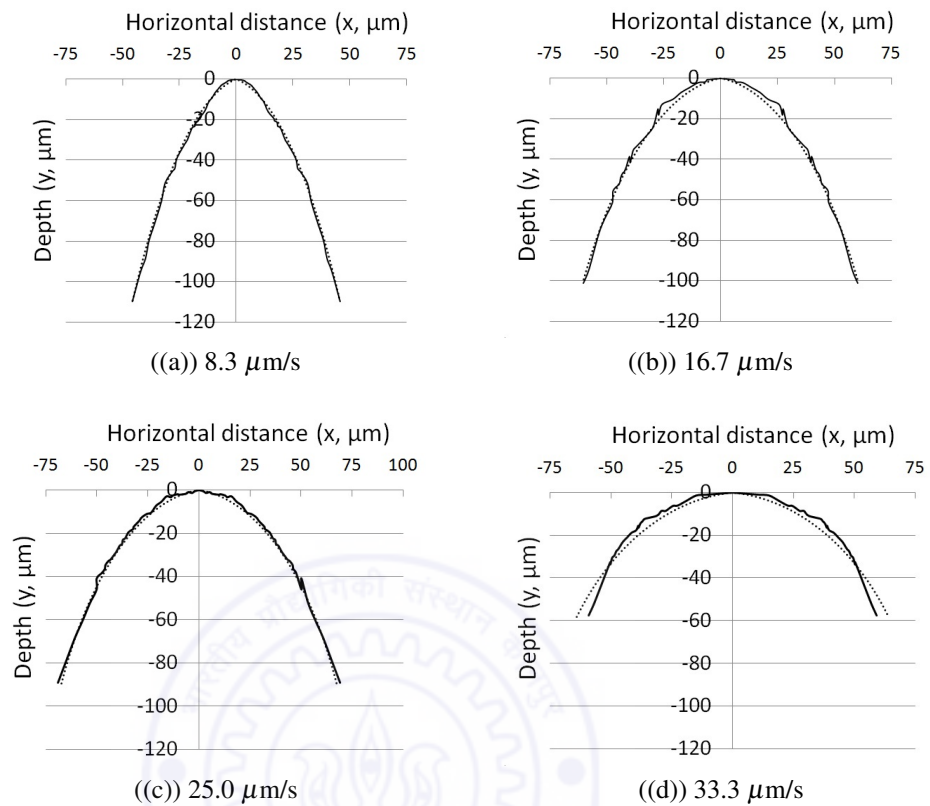


Figure 6.7: Experimental and theoretical profiles of micro lenses plotted for varying scanning speeds. (Solid line - experimental, dotted line - theoretical)

Micro lens profile - Experimental results

Figure 6.7 shows the experimentally determined profiles of micro lenses in comparison with the theoretically predicted ones. All features show conformance to the theoretical profile to a very high degree. It can be noted that lenses machined at higher scanning speeds have lower machined depths. This is because lesser number of pulses fall per spot at a higher speed. The surface roughnesses of the lenses are not low enough for direct application in micro-optics application. The roughness can be reduced by, for example, the polymer reflow method. Figure 6.8 shows the surface profiles of the machined lenses for the case of scanning speed of $33.3 \mu\text{m/s}$.

Excimer laser micro machining has provided a novel method to fabricate micro lens arrays. Unlike any other present technique used to fabricate the micro lenses, most of which are spherical, excimer laser micromachining with mask projection offers a great control on the profile (asphericity) of the lenses. This is specially useful in applications that require a deviation from a spherical profile. It allows machining of the desired profile by direct designing of the mask, and does away with the trials and errors with experimental parameters. The effects of scanning speed and mask pattern are discussed in this section. At moderate scanning speeds the experimental profile agrees with the theoretical feature accurately. The number of pulses per spot is high at low scanning speeds. Hence, lenses are machined to a greater depth at low scanning speeds.

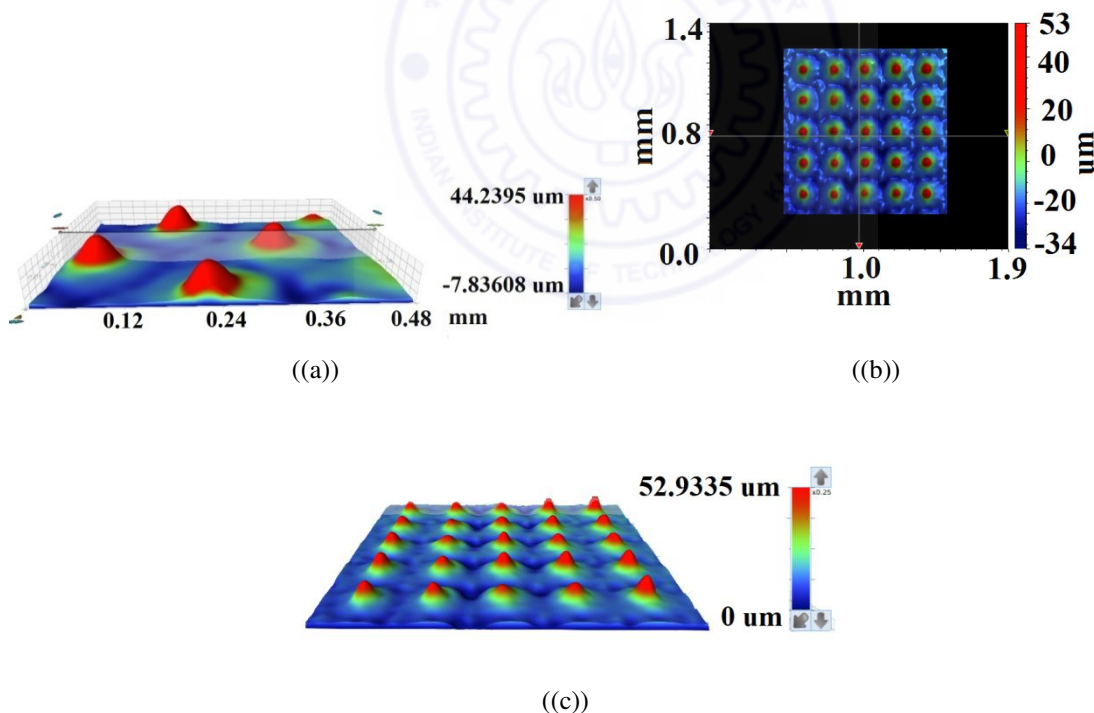


Figure 6.8: 3D optical profilographs of 5×5 array of micro lenses fabricated at the scanning speed of $33.3 \mu\text{m/s}$

6.2 Development of a bistable multivibrator

A leading edge triggered bistable multivibrator (also called a T flip flop, or TFF) was developed for automatic switching operation of the excimer laser machine. Generally, the design of a complex pattern comprises several sub-patterns (features) that are not connected to each other, and are spread over a certain area. While moving from one such feature to another, the laser machine is required to be switched off. After the translation of the workpiece, when the new area comes at the position of machining, the laser machine has to be switched on. If there are a few disconnected features, the switching on and off of the laser machine can be done manually. However, when the number of features is more, the manual switching operation not only becomes tedious, but also makes the fabrication process slow. It is then required, that the laser machine be automatically switched on and off, as per the requirement of the process.

6.2.1 Description of the setups and communication protocol

The excimer laser machine has been described in the Section 2.1, and the modes of triggering pulses from the machine are described in Section 2.1.1. For automatic switching of the laser machine, it is required that the machine be operated in the INTG mode. The external trigger socket on the machine is a BNC port, that takes TTL input of 3.3V to 5V DC, with pulse duration between 10 ms and 100 ms. The pulses are triggered as long as the signal at the socket is LOW.

The 3 axis micropositioning stage is controlled by G and M codes. The stage controller has a TRIGGER OUT port, that generates 3.3V to 5V TTL pulse, of 50 ms duration, whenever the code M666 is executed. An electronic circuit (a leading edge triggered bistable multivibrator) is designed that is triggered by the pulse from the controller, and switches its output (from HIGH to LOW, or from LOW to HIGH, depending as the case may be), so that

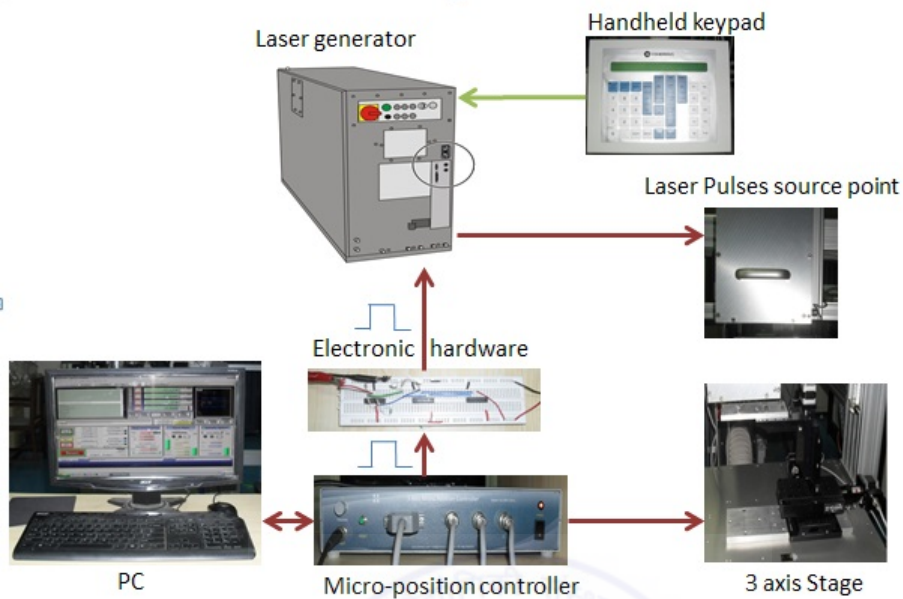


Figure 6.9: A schematic diagram showing the interface between the different components of the laser micromachining setup

the voltage at external trigger socket on the laser machine is either kept LOW (if the pulses have to be fired) or HIGH (if the pulses do not have to be fired).

Figure 6.9 schematically shows the interface between various components of the laser machining setup. In the figure, the workpiece is kept on the 3 axis micropositioning stage (bottom, right). The stage is controlled by the micro-position controller (bottom, center), that in turn is controlled by the computer (bottom, left). Upon execution of a particular code, the controller sends a trigger pulse to the electronic hardware (center, center). The electronic hardware processes the pulse and sends a stable HIGH or LOW signal to the external trigger port of the laser generator (center, top).

The data acquisition of the trigger pulses generated by the micro-controller was performed using the NIcDAQ 9172 and NI 9234 cards. These cards were interfaced with the computer by a USB.

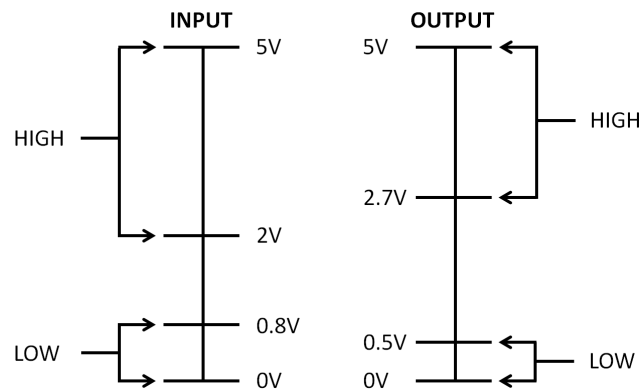


Figure 6.10: A diagram showing the HIGH and LOW voltage ranges for input and output TTL signals

TTL signal protocol

In the TTL (transistor-transistor logic) protocol, a voltage signal of 0V is called LOW and of 5V is called as HIGH. Exact values of 0V and 5V are not possible due to voltage drops in transistors and other resistors. For input signals, the acceptable voltage ranges are 0V to 0.8V for LOW and 2V to 5V for HIGH signals. For output signals, the acceptable voltage ranges are 0V to 0.5V for LOW and 2.7V to 5V for HIGH signals. These values are typically specific to the IC (integrated circuit) chips being used [Kuphaldt (09 March 2014)]. Figure 6.10 schematically depicts the acceptable input and output voltage ranges of TTL gates.

6.2.2 Trigger pulse analysis

The trigger pulse is generated from the micro-controller when the code *M666* is executed by the computer. An analysis of the trigger pulse was performed. Figure 6.11 shows the shape of the trigger pulse. It has the typical HIGH voltage of 4V, and lasts for about 60 ms. Table 6.1 mentions the time and voltage parameters of the various pulses being generated in the electronic hardware, including the trigger pulse. The noise in the HIGH state of the trigger pulse is a cause of concern, which will be addressed in the section on signal conditioning.

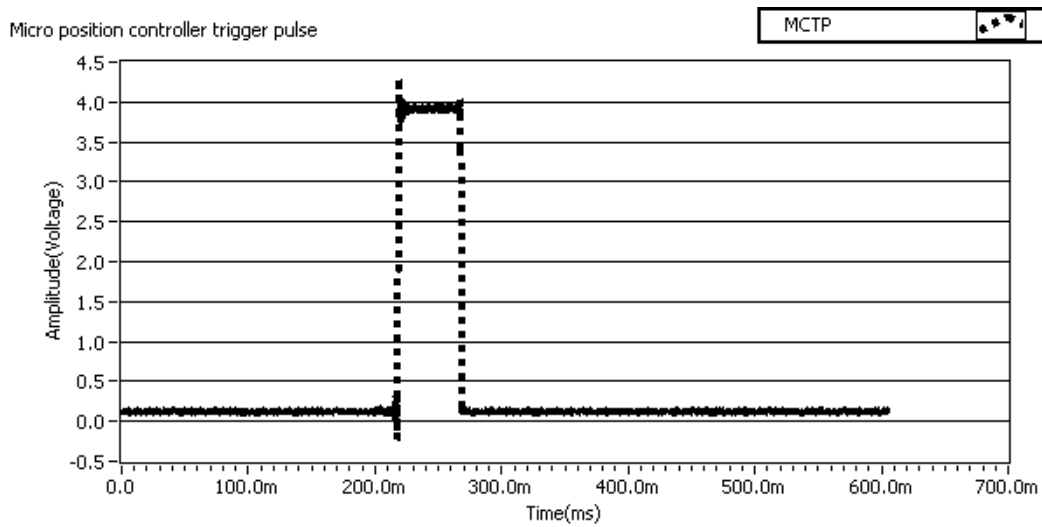


Figure 6.11: The trigger pulse generated from the micro-controller when the code *M666* is executed by the computer

6.2.3 T flip flop

The TFF is a latching circuit, that holds on to its state until a trigger pulse is applied to it. Upon application of the trigger pulse, the TFF toggles its output, and holds on to it. Since it has two output states, it is called a multivibrator. Since it latches, or holds on to either state until a trigger pulse is applied, it is called bistable. The TFF is schematically shown in Fig. 6.12 along with its pulse diagram. The TFF takes two inputs - a data input and the clock

Table 6.1: Voltage domain and time domain parameters of the various pulses

Parameters	Trigger Pulse	Comparator output	Flip flop (FF) output	Amplified FF output
V_{pp}	4.88 V	3.44 V	3.12 V	3.68 V
V_{high}	4.00 V	3.44 V	3.20 V	3.84 V
V_{low}	320 mV	240 mV	160 mV	480 mV
Rise time	766.6 μ s	820.5 μ s	799.9 μ s	800.0 μ s
Fall time	735.9 μ s	800.0 μ s	-	-
Pulse width	61.02 ms	60.98 ms	-	-

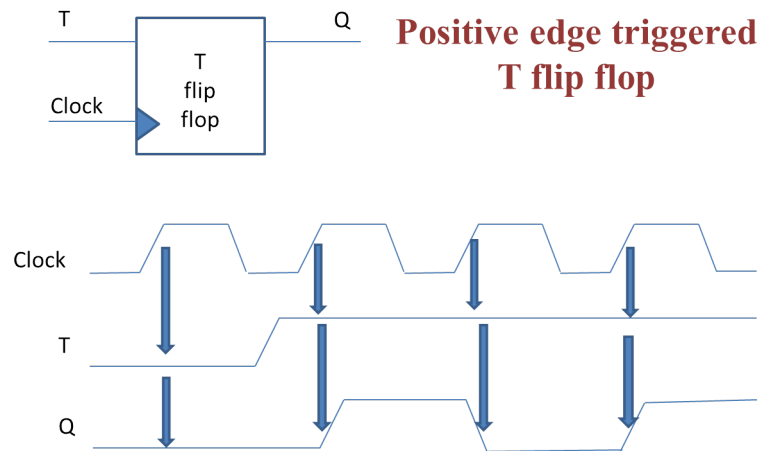


Figure 6.12: A positive edge triggered T flip flop, showing the input 'T' and the output 'Q'. Note that it toggles its state at every clock pulse, if the input is HIGH.

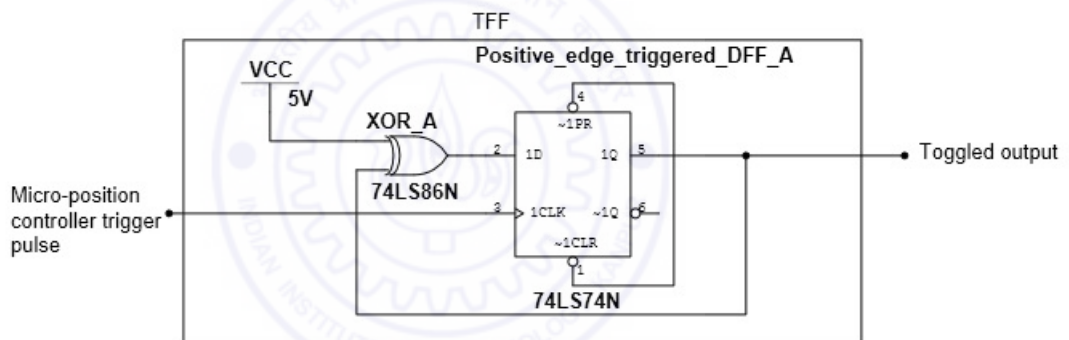


Figure 6.13: The circuit diagram of T flip flop

signal. If the data input is HIGH, every clock pulse triggers the output of the TFF, as can be seen from the pulse diagram.

The TFF was built using a D flip flop (IC 74LS74N) and a XOR gate (74LS86N). The circuit diagram of the TFF, drawn in NI Multisim, is shown in Fig. 6.13. The voltage of the HIGH output from the TFF is 3.18 V, which is below the HIGH threshold (3.3 V) of the TRIGGER IN port of the excimer laser machine. Hence the output of the TFF needs to be amplified, the procedure of which is described in the section on signal conditioning.

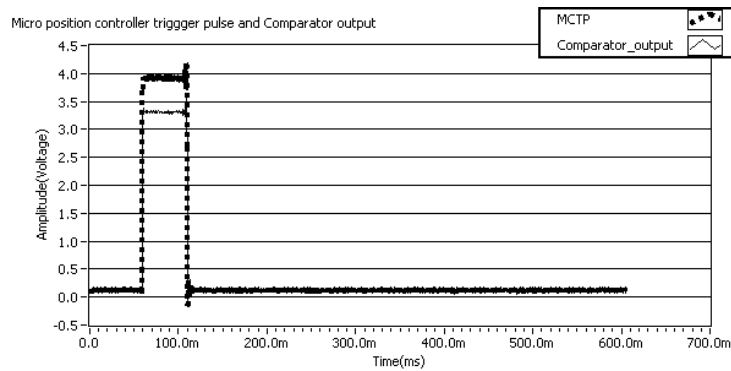


Figure 6.14: The temporal profile of the trigger pulse before and after the comparator

6.2.4 Signal conditioning

Signal conditioning is required when an output signal does not meet the criteria for an input port. Here we discuss two types of basic conditioning, namely, removal of noise and undetermined state of the trigger pulse, and amplification of the TFF output.

The noise in the trigger pulse is removed by using a comparator. A comparator is an OP-AMP (operational amplifier) that takes four inputs, namely, high and low voltages, a reference voltage and the input signal. Depending on whether the input voltage is higher or lower than the reference voltage, the OP-AMP generates the high or low voltage output, respectively. LM324N IC is used in this work as the comparator. The values of high, low and reference voltages are set at 5 V, 0 V and 2.5 V, respectively. Since the HIGH state of the trigger pulse has the voltage greater than 2.5 V, the noise gets filtered by the comparator, and a steady output voltage (about 3.3 V) is obtained from the comparator. Figure 6.14 shows the state of the trigger pulse directly from the micro-controller (large dots) and after the comparator (small dots). A stable trigger pulse is obtained from the comparator, that can be sent to the TFF.

The voltage output from the TFF (about 3.18 V) is amplified to 3.7 V, using a non-inverting amplifier. The gain of the amplifier, A , is defined as the ratio of the output to the

input voltages, and expressed mathematically as,

$$A = \frac{V_o}{V_i} = 1 + \frac{R_f}{R_i}. \quad (6.4)$$

Here, V_o and V_i are output and input voltages, and R_f and R_i are feedback and input resistances. LM324N IC is used as the non-inverting amplifier.

6.2.5 The leading edge triggered bistable multivibrator

The complete bistable multivibrator circuit is ready after incorporating the comparator, TFF and the non-inverting amplifier. The circuit diagram of the complete circuit is shown in Fig. 6.15. The output of the bistable multivibrator is fed to the external trigger socket of the excimer laser machine via a BNC cable, as mentioned earlier.

6.2.6 A working example of the automatic switching of the excimer laser machine

Mentioned below is the G-code to move the micro-positioning stage along two parallel lines, each 250 μm long, and 100 μm apart. While machining, this allows the fabrication of two straight and parallel channels, with the same dimensions.

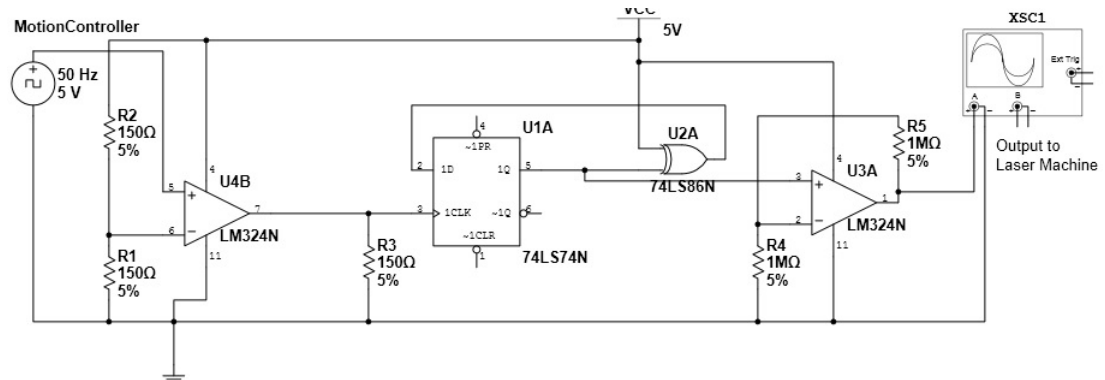


Figure 6.15: The circuit diagram of the complete edge triggered bistable multivibrator

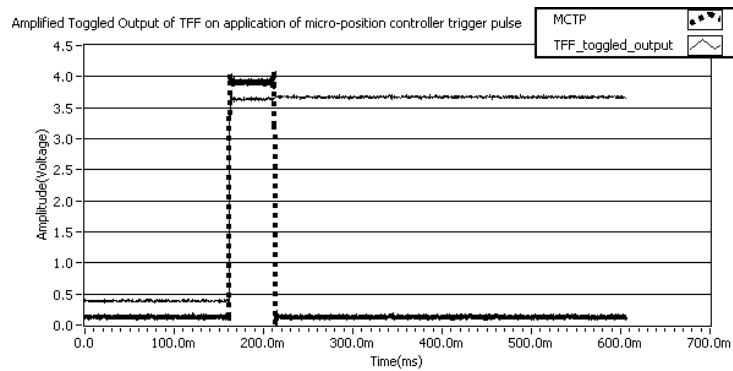


Figure 6.16: The toggling of the output from LOW to HIGH upon application of the trigger pulse. The HIGH voltage at the external trigger socket of the laser machine causes the firing of the laser pulses to stop.

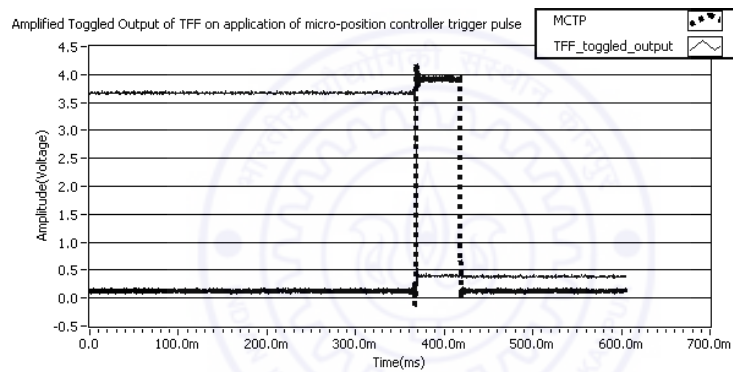


Figure 6.17: The toggling of the output from HIGH to LOW upon application of the trigger pulse. The LOW voltage at the external trigger socket of the laser machine causes the firing of the laser pulses to start.

N10 G90 (absolute distance mode)

N20 X0 Y0

N30 M666 (Switch ON the pulse)

N40 G1 X250 Y0 F50.0

N50 M666 (Switch OFF the pulse)

N60 G1 Y-100

N70 M666 (Switch ON the pulse)

N80 G1 X0

N90 M666 (Switch OFF the pulse)

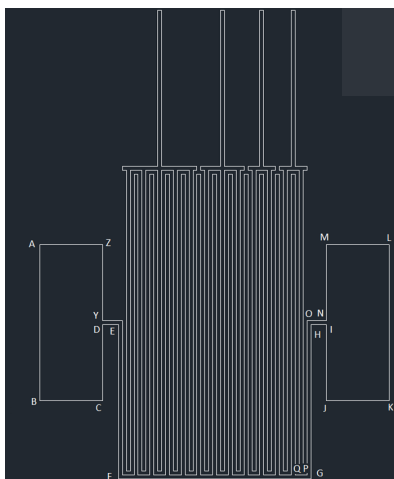
The execution of line N30 starts the firing of the pulses. After the stage has moved by the distance of $250 \mu\text{m}$ along the x axis, the stage stops. Subsequently, N50 causes the machine to stop firing the pulses. The stage then moves by $100 \mu\text{m}$ along the negative y axis, and the process is repeated. A comparative of the times required to fabricate the two channels, with and without automatic switching of the laser machine, is provided in Table 6.2. Using the automatic switching of the laser machine, about 12 seconds of operating time is saved while machining two $250 \mu\text{m}$ long channels, for example.

Table 6.2: Comparison of the times required to fabricate two $250 \mu\text{m}$ long channels, with and without automatic switching of the laser machine

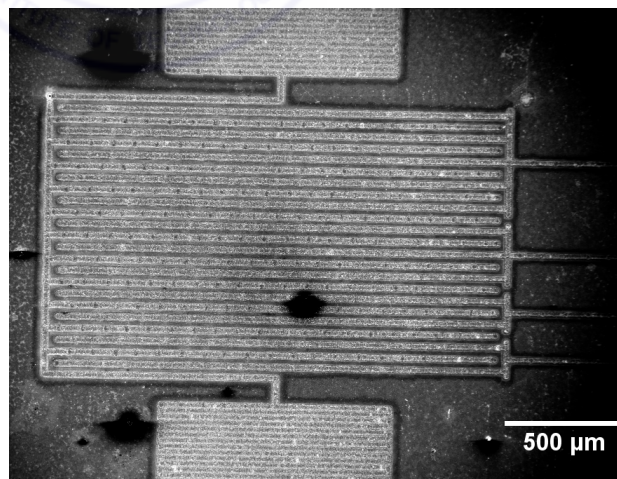
Time required (seconds)	Manual switching	Auto switching
Switch on the pulses	2	Auto
Run the G code	2	2
Time to machine the channel	5	5
Switch off the pulses	2	Auto
Run the G code	2	Auto
Switch on the pulses	2	Auto
Run the G code	2	Auto
Time to machine the channel	5	5
Switch off the pulses	2	Auto
Total	24	12

6.3 Fabrication of sample circuits for use as MHMICs

Microwave circuits and transmission lines have also followed the miniaturization route for enhancing performance at high frequencies with decreased power and space requirements. Miniaturized hybrid microwave integrated circuits (MHMIC) for space applications places extra-ordinary demands on the accuracy and reproducibility. Several processing techniques are presently used for MHMIC fabrication, such as, e-beam and photolithography techniques. These are expensive and time-consuming processes involving wet chemical etching. Excimer laser micro-machining is a dry fabrication process that represents an excellent alternative for the rapid-prototyping and production of microwave transmission lines, circuit elements and entire MHMIC with high accuracy. Using the parameters optimized for machining metal films, several test features were fabricated by excimer laser micromachining. Some of the fabricated features are discussed in the following subsections.



((a)) A drawing of a set of straight interdigitated electrodes. The individual electrodes are $25 \mu\text{m}$ wide. The inter-electrode gap is $25 \mu\text{m}$.



((b)) Scanning electron micrographs of straight interdigitated electrodes fabricated on gold coated alumina substrate. The black regions in the image show charring of the substrate by the electron beam.

Figure 6.18: Examples of interdigitated electrodes

6.3.1 Fabrication of interdigitated electrodes

Interdigitated electrodes were designed on a commercially available CAD (Computer aided designing) software. Figure 6.18(a) shows the drawing of a set of straight interdigitated electrodes, with each electrode (metal strip) having a width of $25\ \mu\text{m}$ and a similar inter-electrode gap. One such feature is shown in Fig. 6.18(b), which is a circuit with interdigitated electrodes. The individual metal strips have a thickness of $25\ \mu\text{m}$.

Micro-patterns of several shapes have been fabricated on aluminum and chromium films coated on glass substrates. The interdigitated electrodes are shown in Fig. 6.19. In each of the micrographs shown in Fig. 6.19, features as small as $25\ \mu\text{m}$ in characteristic dimensions

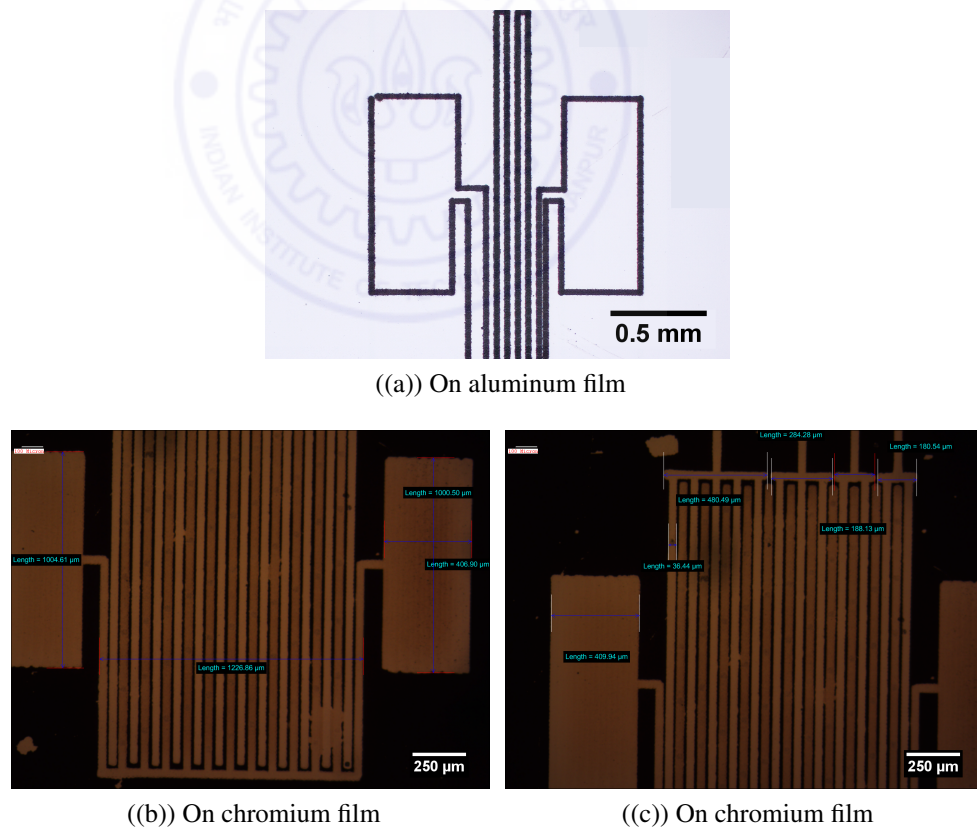


Figure 6.19: The optical micrographs of the interdigitated electrodes fabricated on aluminum and chromium films

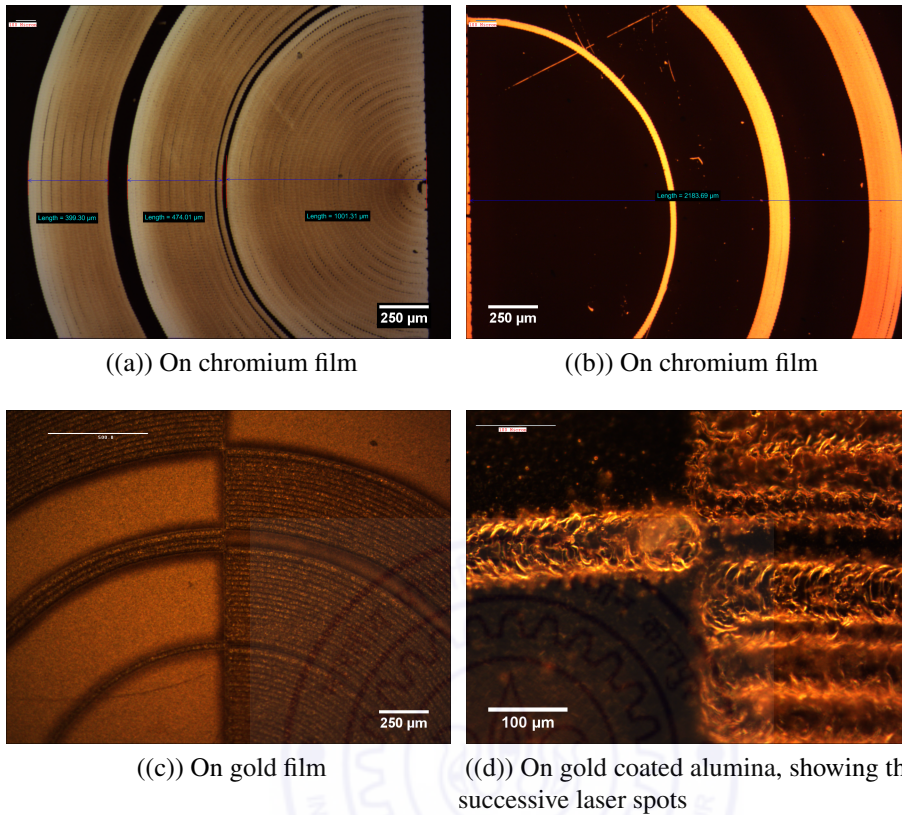


Figure 6.20: The optical micrographs of the circular test patterns fabricated on chromium and gold films, and on gold coated alumina

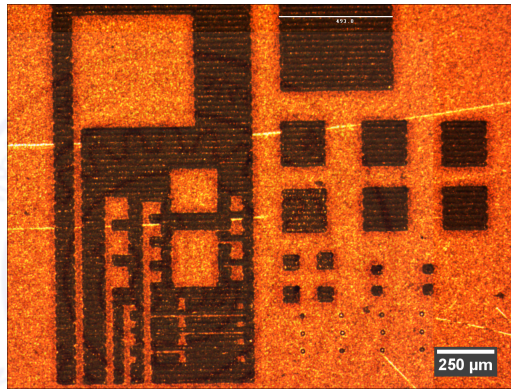
have been fabricated. The technique allows us to fabricate features of the characteristic dimensions down to a single micrometer, directly on metal films.

Circular test patterns were also fabricated on gold and chromium films. The diameter of the entire pattern is 4 mm. Some of the circular patterns are shown in Fig. 6.20. The minimum distance between two unmachined regions is about $22 \mu\text{m}$. Figure 6.20(d) is a dark field optical micrograph. The overlapping laser spots can be clearly observed in the figure. The surfaces generated, while machining gold coated alumina, were very rough, because of the $5 \mu\text{m}$ thick gold film. The excimer laser micromachining does not ablate such thick metal coatings cleanly.

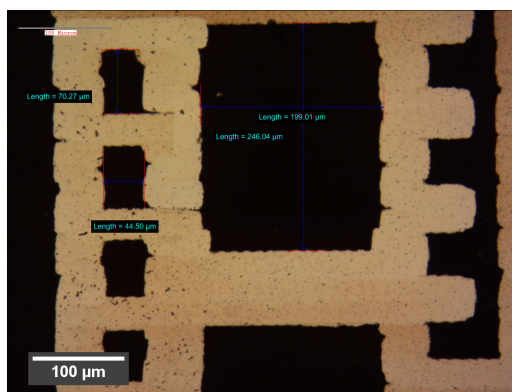
6.3.2 Fabrication of connecting pads

Connecting pads are fabricated in gold coated alumina and in chromium film, and are shown in Fig. 6.21. The sizes of the pads range from 25 μm to 500 μm .

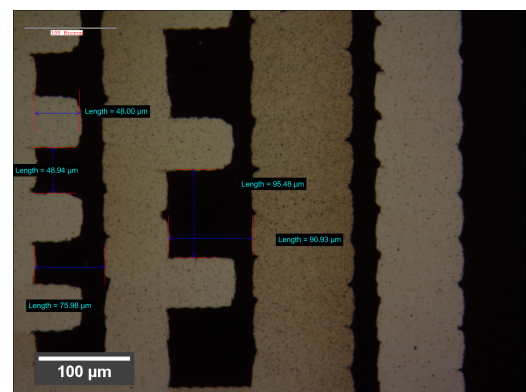
Thus, excimer laser micromachining of metal films, post polymer coating, is a better (simpler and quicker) alternative to various other techniques currently being used to fabricate the afore-mentioned devices.



((a)) The optical micrograph of the complete test pattern, machined in gold film, showing connecting pads of varying sizes, from 500 μm in size down to 25 μm .



((b)) Connecting pads machined in chromium film



((c)) Connecting pads machined in chromium film

Figure 6.21: The optical micrographs of the connecting pads fabricated on gold coated alumina and chromium film

Chapter 7

Conclusions and scope for future work

The work presented in this thesis helps in understanding the excimer laser ablation of polymers and metals, in terms of the ablation parameters to be used, the feature quality, and the ablation rates obtainable, under varying machining conditions. Limitations of excimer laser micromachining are highlighted for, for example, machining metals. With the development of the understanding of the metal and polymer ablation, studies are undertaken to machine metals and polymers, separately and together as bilayer structures. Patterning of metal films and polymer surfaces is demonstrated, with techniques to improve the quality of the patterns generated in these cases.

The dynamic photolytic ablation model, for polymers, may be extended to make the material parameters (for plasma shielding, defined as 'a' and 'b') dependent on the local temperature. This will reduce the ablation threshold with increase in temperature. A certain portion of the fluence may be used for generating thermal effects, depending on the ratio of the optical penetration depth and the thermal diffusion depth of the polymer.

The excimer laser ablation of metals is a process that involves extreme conditions of temperature and pressure in the irradiated region, leading to several processes, such as superheating, phase explosion, spallation and Coulomb explosion. Although these processes

have been studied by researchers using molecular dynamic simulations and atomistic modeling, the presence of these processes makes the numerical models of metal ablation highly unstable. Advanced stabilization techniques need to be used to successfully model the metal ablation process. Further, the numerical model may be extended to include plasma shielding, keyhole waveguiding and scattering losses in the material.

The micromachining of thin metal films, post polymer coating, is a promising technique, that allows direct and clean micropatterning. With the demonstration of the ability of this technique, it may be extended to micromachining multi-layered systems, with several alternating layers of metal and polymer (dielectric) coatings. The technique needs to be developed further to selectively machine individual metal or polymer layer, so that it may be deployed for fabrication of multi-layered miniaturized integrated circuits. The technique needs to be developed to use excimer lasers to cleanly ablate metal coatings upto $5\ \mu\text{m}$ thick.

Present day techniques rely on a set of experimental data, generated from experimental trials, to control the profile of the micro lenses. Excimer laser micromachining using mask projection, on the other hand, provides a positive method to design the profile of the micro lenses from the very beginning. With the demonstration of the capability of this technique to fabricate micro lenses, a comprehensive study may be carried out on the designing of the mask profile, that will in turn generate the desired (aspherical) lens profile. Since the rectangular arrays of micro lenses are fabricated by scanning the workpiece along two perpendicular axes, there will be regions on the workpiece which will be twice irradiated, once in each pass. Hence the total fluence at any spot needs to be considered while designing the mask, so that the net depth of ablation at any point corresponds to the desired profile. Additionally, the fill factor of the micro lens array can be increased by trimming the lenses, which requires the trimming of the transparent regions of the mask.

The surface roughness obtained for the microlenses, fabricated in this study, needs to be reduced before these microlenses can be used in micro-optics applications. The technique of

polymer reflow, similar to that of resist reflow, is suggested to smoothen the lens profile. It is important to perform the polymer reflow in a controlled manner, so that the desired profile is not lost, and only the surface irregularities are smoothened out.



References

- Agrawal, A., Cao, H., and Nahata, A., “Excitation and scattering of surface plasmon-polaritons on structured metal films and their application to pulse shaping and enhanced transmission,” *New Journal of Physics*, 2005, **vol. 7**, 1, pp. 249–261.
- Akhtar, S. N., Ramakrishna, S. A., and Ramkumar, J., “Excimer Laser Micromachining on Polymers Under Different Atmospheres and at Different Length Scales,” in *8th International Conference on Micromanufacturing, Victoria, Canada*.
- Akhtar, S. N., Ramakrishna, S. A., and Ramkumar, J., “Microfeature Edge Quality Optimization in Excimer Laser Ablation of Metallic Film,” in *Proceedings of the ASME 2013 International Mechanical Engineering Congress & Exposition, San Diego, California, USA*.
- Akhtar, S. N., Sharma, S., Dayal, G., Ramakrishna, S. A., and Ramkumar, J., “Microfeature edge quality enhancement in excimer laser micromachining of metal films by coating with a sacrificial polymer layer,” *IOP Journal of Micromechanics and Microengineering*, 2015, **vol. 25**, 6, pp. 065001–065012.
- Andrew, J. E., Dyer, P. E., Greenough, R. D., and Key, P., “Metal film removal and patterning using a XeCl laser,” *Applied Physics Letters*, 1983, **vol. 43**, 11, pp. 1076–1078.
- Anisimov, S. and Khokhlov, V., *Instabilities in laser-matter interaction*, CRC Press, Boca Raton, Florida, 1995.

Arnold, J., "Abtragen metallischer und keramischer Werkstoffe," *Laser in der Materialbearbeitung*, Teubner, Stuttgart, 1994.

Attia, G. and El-kader, M. A., "Structural, Optical and Thermal Characterization of PVA/2HEC Polyblend Films," *Int. J. Electrochem. Sci*, 2013, **vol. 8**, pp. 5672–5687.

Bailey, C., "Stainless Steel Thermal Properties," <http://www.mace.manchester.ac.uk/project/research/structures/stainless-steel/thermal-properties.htm>, 21 June 2012.

Bailey, C., "Photoablation in Polymers," <http://www.scribd.com/doc/51549898/25/Model-of-Photoablation>, 25 July 2012.

Basov, N. G., Danilychev, V. A., Popov, Y. M., and Khodkevich, D. D., *Zh. Eksp. Fiz. i Tekh. Pis'ma. Red.*, 1970, **vol. 12**, pp. 473–475.

Basting, D., Pippert, K., and Stamm, U., "History and future prospects of excimer laser technology," *Riken Review*, 2002, pp. 14–22.

Benjamin, P. and Weaver, C., "The adhesion of evaporated metal films on glass," *Proceedings of the Royal Society of London. Series A, Mathematical and Physical Sciences*, 1961, **vol. 261**, 1307, pp. 516–531.

Blum, S. E., Srinivasan, R., and Wynne, J. J., "Far ultraviolet surgical and dental procedures," *US Patent 4,784,135*, 1988.

Brannon, J. H., "Micropatterning of surfaces by excimer laser projection," *Journal of Vacuum Science & Technology B*, 1989, **vol. 7**, 5, pp. 1064–1071.

Brannon, J. H., "Excimer-laser ablation and etching," *Circuits and Devices Magazine, IEEE*, 1990, **vol. 6**, 5, pp. 18–24.

Brown, A. I. and Marco, S. M., *Introduction to Heat Transfer*, McGraw-Hill, New York, NY, 1958.

- Bulgakova, N. and Bulgakov, A., "Pulsed laser ablation of solids: transition from normal vaporization to phase explosion," *Applied Physics A: Materials Science & Processing*, 2001, **vol. 73**, 2, pp. 199–208.
- Byskov-Nielsen, B., "Short-pulse laser ablation of metals: Fundamentals and applications for micro-mechanical interlocking," Ph.D. thesis, University of Aarhus, Denmark, 2010.
- Chase Jr, M. W., *NIST Chemistry WebBook, NIST Standard Reference Database Number 69*, National Institute of Standards and Technology, Gaithersburg MD, 13 Jul 2014.
- Choudhary, H., "Numerical simulation and experiments of nano pulsed UV laser on metal and polymer," Master's thesis, Indian Institute of Technology Kanpur, Kanpur, India, 2012.
- Cohen, L. and Schneider, M., "Microlenses for coupling junction lasers to optical fibers," *Applied Optics*, 1974, **vol. 13**, 1, pp. 89–94.
- Cohen, M. I., Milkosky, J. F., and Unger, B. A., "Laser machining of thin films and integrated (Thermal machining of thin films and integrated circuits by yttrium-aluminum garnet laser)," *Bell System Technical Journal*, 1968, **vol. 47**, pp. 385–405.
- Coherent, *User Manual COMPex Pro (RoHS)*, Coherent GmbH, Germany, 2008.
- Coherent-GmbH, "Coherent Inc. VarioLas for UV microprocessing laser applications," <http://www.coherent.com/products/?1043/VarioLas-Family>, 2 March 2013.
- Conrad, H., Klose, T., Sandner, T., Jung, D., Schenk, H., and Lakner, H., "Modeling the Thermally Induced Curvature of Multilayer Coatings with COMSOL Multiphysics™," in *Proceedings of COMSOL Conference, Hannover*.
- Dan, L. and Duan-Ming, Z., "Vaporization and plasma shielding during high power nanosec-

- ond laser ablation of silicon and nickel,” *Chinese Physics Letters*, 2008, **vol. 25**, 4, pp. 1368–1371.
- Dayal, G., Akhtar, S. N., Ramakrishna, S. A., and Ramkumar, J., “Excimer laser micro-machining using binary mask projection for large area patterning with single micrometer features,” *ASME Journal of Micro and Nano Manufacturing*, 2013a, **vol. 1**, 3, pp. 031002–1–7.
- Dayal, G., Ramakrishna, S. A., and Ramkumar, J., “Dry processing method for the fabrication of binary masks with arbitrary shapes for ultra-violet laser micromachining,” , 2013b.
- Dhote, A. M., Shreekala, R., Patil, S. I., Ogale, S. B., Venkatesan, T., and Williams, C. M., “Pulsed excimer laser etching of La_{0.75}Ca_{0.25}MnO_x thin films,” *Applied Physics Letters*, 1995, **vol. 67**, 24, pp. 3644–3646.
- Dijkkamp, D., Gozdz, A., Venkatesan, T., and Wu, X., “Evidence for the thermal nature of laser-induced polymer ablation,” *Physical Review Letters*, 1987, **vol. 58**, 20, pp. 2142–2145.
- Dubey, A. K. and Yadava, V., “Laser beam machining A review,” *International Journal of Machine Tools and Manufacture*, 2008, **vol. 48**, 6, pp. 609–628.
- Dyer, P., “Excimer laser polymer ablation: twenty years on,” *Applied Physics A*, 2003, **vol. 77**, 2, pp. 167–173.
- Dyer, P. and Sidhu, J., “Excimer laser ablation and thermal coupling efficiency to polymer films,” *Journal of Applied Physics*, 1985, **vol. 57**, 4, pp. 1420–1422.
- Feng, Y., Liu, Z., and Yi, X., “Co-occurrence of photochemical and thermal effects during laser polymer ablation via a 248-nm excimer laser,” *Applied Surface Science*, 2000, **vol. 156**, 1, pp. 177–182.

- Garrison, B. and Srinivasan, R., "Laser ablation of organic polymers: microscopic models for photochemical and thermal processes," *Journal of Applied Physics*, 1985, **vol. 57**, 8, pp. 2909–2914.
- Geller, G. R., Suppelsa, A. B., and Martin, W. J., "Method of trimming thick film capacitor," *US Patent 4,338,506*, 1982.
- Ghoreishi, M., Low, D., and Li, L., "Comparative statistical analysis of hole taper and circularity in laser percussion drilling," *International Journal of Machine Tools and Manufacture*, 2002, **vol. 42**, 9, pp. 985–995.
- Guo, C. F., Cao, S., Jiang, P., Fang, Y., Zhang, J., Fan, Y., Wang, Y., Xu, W., Zhao, Z., and Liu, Q., "Grayscale photomask fabricated by laser direct writing in metallic nano-films," *Opt. Express*, 2009, **vol. 17**, 22, pp. 19981–19987.
- Han, W., "Theoretical and experimental investigation of laser drilling of small holes in metals," Master's thesis, Center for Holographic Studies and Laser Micro Mechatronics, Worcester Polytechnic Institute, Worcester, MA, 1999.
- Han, W., Yokum, J., and Pryputniewicz, R., "Parametric study of laser microdrilling process for MEMS fabrication," in *Poster Session II, Proc. 2004 SEM X International Congress & Exposition on Experimental & Applied Mechanics, Costa Mesa, California*.
- Herman, R. and Wiggins, T., "Rayleigh range and the M^2 factor for Bessel–Gauss beams," *Applied optics*, 1998, **vol. 37**, 16, pp. 3398–3400.
- Herzig, H. P., *Micro-optics: elements, systems and applications*, CRC Press, 1997.
- Hess, W., "Improved manufacture of stereoscopic pictures," *UK Patent 13034*, 1912.
- Heydel, R., Matz, R., and Göpel, W., "Maskless excimer laser induced projection patterning of InP in Cl_2 etch gas," *Applied Surface Science*, 1993, **vol. 69**, 1, pp. 38–45.

- Jain, K., Willson, C., and Lin, B., "Ultrafast deep UV lithography with excimer lasers," *Electron Device Letters, IEEE*, 1982, **vol. 3**, 3, pp. 53–55.
- Jensen, M., "Laser micromachining of polymers," Ph.D. thesis, Technical University of Denmark, Denmark, 2004.
- Jiang, C., Lau, W., Yue, T., and Chiang, L., "On the maximum depth and profile of cut in pulsed Nd: YAG laser machining," *CIRP Annals-Manufacturing Technology*, 1993, **vol. 42**, 1, pp. 223–226.
- Karbasi, H., "Computer Simulation of Laser Material Removal: Measuring the Depth of Penetration in Laser Engraving," in *Paper 1909, Proceedings of the 27th International Congress on Applications of Lasers and Electro-Optics (ICALEO'08), Temecula, California*.
- Karp, J. H., Tremblay, E. J., and Ford, J. E., "Planar micro-optic solar concentrator," *Optics Express*, 2010, **vol. 18**, 2, pp. 1122–1133.
- Kawamura, Y., Kai, A., and Yoshii, K., "Various Kinds of Pulsed Ultraviolet Laser Micromachinings Using a Five Axis Microstage," *JLMN-Journal of Laser Micro/Nanoengineering*, 2010, **vol. 5**, 2, pp. 163–168.
- Kelly, R. and Miotello, A., "Contribution of vaporization and boiling to thermal-spike sputtering by ions or laser pulses," *Physical Review E*, 1999, **vol. 60**, 3, p. 2616.
- Klotzbach, U., Lasagni, A. F., Panzner, M., and Franke, V., "Laser Micromachining," in Lasagni, F. A. and Lasagni, A. F. (eds.), *Fabrication and characterization in the micro-nano range*, Springer-Verlag, Berlin, 2011.
- Koo, J. C.-Y. and Zaleckas, V. J., "Removal of thin films from substrates by laser induced explosion," *US Patent 4,081,653*, 1978.

- Kuhnke, M., Dumitru, G., Lippert, T., Ortelli, E., Scherer, G. G., and Wokaun, A., "Micro-machining of Carbon Materials and Laser Micropatterning of Metal Films used as Masks for Reactive Ion Etching," *JLMN-Journal of Laser Micro/Nanoengineering*, 2006, **vol. 1**, 1, pp. 67–73.
- Kuhnke, M., Lippert, T., Scherer, G. G., and Wokaun, A., "MicroFabrication of flow field channels in glassy carbon by a combined laser and reactive ion etching process," *Surface and Coatings Technology*, 2005, **vol. 200**, 1, pp. 730–733.
- Küper, S., Brannon, J., and Brannon, K., "Threshold behavior in polyimide photoablation: single-shot rate measurements and surface-temperature modeling," *Applied Physics A*, 1993, **vol. 56**, 1, pp. 43–50.
- Kuphaldt, T. R., "TTL signal, Logic signal voltage levels," http://www.allaboutcircuits.com/vol_4/chpt_3/10.html, 09 March 2014.
- Landy, N., Bingham, C., Tyler, T., Jokerst, N., Smith, D., and Padilla, W., "Design, theory, and measurement of a polarization-insensitive absorber for terahertz imaging," *Physical Review B*, 2009, **vol. 79**, 12, p. 125104.
- Lazare, S., Lopez, J., and Weisbuch, F., "High-aspect-ratio microdrilling in polymeric materials with intense KrF laser radiation," *Applied Physics A: Materials Science & Processing*, 1999, **vol. 69**, pp. 1–6.
- Lazare, S. and Tokarev, V., "Recent experimental and theoretical advances in microdrilling of polymers with ultraviolet laser beams," in *Fifth International Symposium on Laser Precision Microfabrication*, International Society for Optics and Photonics, pp. 221–231.
- Lee, Y.-C., Chen, C.-M., and Wu, C.-Y., "A new excimer laser micromachining method for axially symmetric 3D microstructures with continuous surface profiles," *Sensors and Actuators A: Physical*, 2005, **vol. 117**, 2, pp. 349–355.

- Lee, Y.-C. and Wu, C.-Y., "Excimer laser micromachining of aspheric microlenses with precise surface profile control and optimal focusing capability," *Optics and Lasers in Engineering*, 2007, **vol. 45**, 1, pp. 116–125.
- Leong, C., "Micromachining using an excimer (248 nm) laser," Master's thesis, Graduate College of the Oklahoma State University, Stillwater, OK, 1999.
- Lide, D. R., *CRC Handbook of Chemistry and Physics*, CRC Press, Boca Raton, Florida, Internet Version 2005.
- Lim, H. and Yoo, J., "FEM based simulation of the pulsed laser ablation process in nanosecond fields," *Journal of Mechanical Science and Technology*, 2011, **vol. 25**, 7, pp. 1811–1816.
- Linsker, R., Srinivasan, R., Wynne, J. J., and Alonso, D. R., "Far-ultraviolet laser ablation of atherosclerotic lesions," *Lasers in surgery and medicine*, 1984, **vol. 4**, 2, pp. 201–206.
- Lippmann, G., "Épreuves réversibles. Photographies intégrales," in *Comptes Rendus de l'Académie des Sciences*, vol. 146, pp. 446–451.
- Lorazo, P., Lewis, L. J., and Meunier, M., "Short-pulse laser ablation of solids: from phase explosion to fragmentation," *Physical Review Letters*, 2003, **vol. 91**, 22, p. 225502.
- Low, D., Li, L., and Corfe, A., "Effects of assist gas on the physical characteristics of spatter during laser percussion drilling of Nimonic 263 alloy," *Applied Surface Science*, 2000, **vol. 154**, pp. 689–695.
- Low, D. K., Li, L., and Byrd, P. J., "Spatter removal characteristics and spatter prevention during laser percussion drilling of aerospace alloys," *Journal of Laser Applications*, 2001, **vol. 13**, 2, pp. 70–78.

- Lu, Q., Mao, S. S., Mao, X., and Russo, R. E., “Thermal model of phase explosion for high-power laser ablation,” in *International Symposium on High-Power Laser Ablation 2002*, International Society for Optics and Photonics, pp. 959–964.
- MacFarlane, D., Narayan, V., Tatum, J., Cox, W., Chen, T., and Hayes, D., “Microjet fabrication of microlens arrays,” *IEEE Photonics Technology Letters*, 1994, **vol. 6**, pp. 1112–1114.
- Maier, S. A., *Plasmonics: Fundamentals and Applications: Fundamentals and Applications*, Springer, New York, 2007.
- Manz, A., Graber, N., and Widmer, H., “Miniaturized total chemical analysis systems: a novel concept for chemical sensing,” *Sensors and Actuators B: Chemical*, 1990, **vol. 1**, 1, pp. 244–248.
- Matthias, E., Reichling, M., Siegel, J., Käding, O. W., Petzoldt, S., Skurk, H., Bizenberger, P., and Neske, E., “The influence of thermal diffusion on laser ablation of metal films,” *Applied Physics A*, 1994, **vol. 58**, 2, pp. 129–136.
- Matthias, E., Siegel, J., Petzoldt, S., Reichling, M., Skurk, H., Käding, O., and Neske, E., “In-situ investigation of laser ablation of thin films,” *Thin Solid Films*, 1995, **vol. 254**, 1, pp. 139–146.
- Mazumder, J. and Steen, W., “Heat transfer model for CW laser material processing,” *Journal of Applied Physics*, 1980, **vol. 51**, 2, pp. 941–947.
- McDonald, R. A., “Enthalpy, heat capacity, and heat of fusion of aluminum from 366 K to 1647 K,” *Journal of Chemical and Engineering Data*, 1967, **vol. 12**, 1, pp. 115–118.
- Meijer, J., “Laser beam machining (LBM), state of the art and new opportunities,” *Journal of Materials Processing Technology*, 2004, **vol. 149**, 1, pp. 2–17.

- Meijer, J., Du, K., Gillner, A., Hoffmann, D., Kovalenko, V., Masuzawa, T., Ostendorf, A., Poprawe, R., and Schulz, W., "Laser machining by short and ultrashort pulses, state of the art and new opportunities in the age of the photons," *CIRP Annals-Manufacturing Technology*, 2002, **vol. 51**, 2, pp. 531–550.
- Mendes, M. and Vilar, R., "Influence of the working atmosphere on the excimer laser ablation of Al₂O₃-TiC ceramics," *Applied Surface Science*, 2003, **vol. 206**, 1, pp. 196–208.
- Miotello, A. and Kelly, R., "Critical assessment of thermal models for laser sputtering at high fluences," *Applied Physics Letters*, 1995, **vol. 67**, 24, pp. 3535–3537.
- Miyamoto, K. and Hayashi, H., "Process of thin Cu film removal by KrF excimer laser," *The Review of Laser Engineering*, 1995, **vol. 23**, 12, pp. 1081–1089.
- Montgomery, D. C., *Design and analysis of experiments*, John Wiley & Sons, 2008.
- Morikawa, J. and Hashimoto, T., "Thermal diffusivity of aromatic polyimide thin films by temperature wave analysis," *Journal of Applied Physics*, 2009, **vol. 105**, 11, pp. 113506–113506.
- Mustafa, F. A., "Optical properties of NaI doped polyvinyl alcohol films," *Physical Sciences Research International*, 2013, **vol. 1**, 1, pp. 1–9.
- Naeem, M., Lane, C., and Valley, S., "Advancement in laser drilling for aerospace gas turbines," *Proceedings of PICALEO*, 2008, pp. 197–202.
- Nagpal, P., Lindquist, N. C., Oh, S.-H., and Norris, D. J., "Ultrasmooth patterned metals for plasmonics and metamaterials," *Science*, 2009, **vol. 325**, 5940, pp. 594–597.
- Nath, A. K., Hansdah, D., Roy, S., and Choudhury, A. R., "A study on laser drilling of thin steel sheet in air and underwater," *Journal of Applied Physics*, 2010, **vol. 107**, 12, p. 123103.

- Ng, G. and Li, L., "The effect of laser peak power and pulse width on the hole geometry repeatability in laser percussion drilling," *Optics & Laser Technology*, 2001, **vol. 33**, 6, pp. 393–402.
- Ng, G. K. L., Crouse, P. L., and Li, L., "An analytical model for laser drilling incorporating effects of exothermic reaction, pulse width and hole geometry," *International Journal of Heat and Mass Transfer*, 2006, **vol. 49**, 7, pp. 1358–1374.
- Okamoto, T., Mori, M., Karasawa, T., Hayakawa, S., Seo, I., and Sato, H., "Ultraviolet-cured polymer microlens arrays," *Applied Optics*, 1999, **vol. 38**, 14, pp. 2991–2996.
- Ong, N., Koh, Y., and Fu, Y. Q., "Microlens array produced using hot embossing process," *Microelectronic Engineering*, 2002, **vol. 60**, 3, pp. 365–379.
- Perez, D. and Lewis, L. J., "Ablation of solids under femtosecond laser pulses," *Physical Review Letters*, 2002, **vol. 89**, 25, p. 255504.
- Perez, D. and Lewis, L. J., "Molecular-dynamics study of ablation of solids under femtosecond laser pulses," *Physical Review B*, 2003, **vol. 67**, 18, p. 184102.
- Polasko, K., Ehrlich, D., Tsao, J., Pease, R., and Marinero, E., "Deep UV exposure of Ag₂Se/GeSe₂ utilizing an excimer laser," *Electron Device Letters, IEEE*, 1984, **vol. 5**, 1, pp. 24–26.
- Popovic, Z. D., Sprague, R. A., and Connell, G., "Technique for monolithic fabrication of microlens arrays," *Applied Optics*, 1988, **vol. 27**, 7, pp. 1281–1284.
- Povel, H., Gale, M. T., Gandorfer, A., Steiner, P., Schu, H., Bernasconi, P. N. et al., "Active alignment of replicated microlens arrays on a charge-coupled device imager," *Optical Engineering*, 1997, **vol. 36**, 5, pp. 1510–1517.

- Ramakrishna, S. A. and Grzegorzcyk, T. M., *Physics and applications of negative refractive index materials*, vol. 186, CRC Press, Boca Raton, Florida, 2009.
- Ratchanikorn, K., “Investigation of the argon shielding gas on the laser welding in titanium,” Master’s thesis, School of Laser Technology and Photonics, Institute of Science, Suranaree University of Technology, Thailand, 2011.
- Ravirajan, P., Haque, S. A., Durrant, J. R., Bradley, D. D., and Nelson, J., “The effect of polymer optoelectronic properties on the performance of multilayer hybrid polymer/TiO₂ solar cells,” *Advanced Functional Materials*, 2005, **vol. 15**, 4, pp. 609–618.
- Ready, J., “Effects due to absorption of laser radiation,” *Journal of Applied Physics*, 1965, **vol. 36**, 2, pp. 462–468.
- Ready, J., *Effects of high-power laser radiation*, Academic Press, New York, NY, 1971.
- Ricciardi, G., Cantello, M., Mariotti, F., Castelli, P., and Giacosa, P., “Micromachining with excimer laser,” *CIRP Annals-Manufacturing Technology*, 1998, **vol. 47**, 1, pp. 145–148.
- Rizvi, N., “Production of novel 3D microstructures using excimer laser mask projection techniques,” in *Design, Test, and Microfabrication of MEMS and MOEMS, Proc. SPIE*, vol. 3680, pp. 546–552.
- Robinson, G. and Jackson, M., “Femtosecond laser micromachining of aluminum surfaces under controlled gas atmospheres,” *Journal of Materials Engineering and Performance*, 2006, **vol. 15**, 2, pp. 155–160.
- Rodden, W., Kudesia, S., Hand, D., and Jones, J., “Use of assist gas in the laser drilling of titanium,” *Journal of Laser Applications*, 2001, **vol. 13**, 5, pp. 204–208.
- Sankur, H. O., Motamedi, M. E., Hall, R. L., Gunning III, W. J., and Khoshnevisan, M.,

- “Fabrication of refractive microlens arrays,” in *Photonics West’95*, International Society for Optics and Photonics, pp. 179–183.
- Saxena, I., Agrawal, A., and Joshi, S. S., “Fabrication of microfilters using excimer laser micromachining and testing of pressure drop,” *Journal of Micromechanics and Micro-engineering*, 2009, **vol. 19**, 2, p. 025025.
- Semak, V., Chen, X., Mundra, K., and Zhao, J., “Numerical simulation of hole profile in high beam intensity laser drilling,” in *Proceedings of the International Congress on Applications of Lasers and Electro–Optics (ICALEO’97)*, San Diego, California, pp. 81–89.
- Semerok, A., Chaléard, C., Detalle, V., Lacour, J., Mauchien, P., Meynadier, P., Nouvellon, C., Sallé, B., Palianov, P., Perdrix, M. et al., “Experimental investigations of laser ablation efficiency of pure metals with femto, pico and nanosecond pulses,” *Applied Surface Science*, 1999, **vol. 138**, 1, pp. 311–314.
- Shehap, A. M., “Thermal and spectroscopic studies of polyvinyl alcohol/sodium carboxy methyl cellulose blends,” *Egypt. J. Solids*, 2008, **vol. 31**, 1, pp. 75–91.
- Shelby, R. A., Smith, D. R., and Schultz, S., “Experimental verification of a negative index of refraction,” *Science*, 2001, **vol. 292**, 5514, pp. 77–79.
- Shen, Z., Zhang, S., Lu, J., and Ni, X., “Mathematical modeling of laser induced heating and melting in solids,” *Optics & Laser Technology*, 2001, **vol. 33**, 8, pp. 533–537.
- Shibasaki, I., Ohmura, K., Kimura, T., and Kobayashi, H., “Thin-film microcircuit board,” *US Patent 4,227,039*, 1980.
- Smith, D. R., Pendry, J. B., and Wiltshire, M. C. K., “Metamaterials and negative refractive index,” *Science*, 2004, **vol. 305**, 5685, pp. 788–792.

- Song, K. H. and Xu, X., “Explosive phase transformation in excimer laser ablation,” *Applied Surface Science*, 1998, **vol. 127**, pp. 111–116.
- Srinivasan, R., Braren, B., Dreyfus, R., Hadel, L., and Seeger, D., “Mechanism of the ultraviolet laser ablation of polymethyl methacrylate at 193 and 248 nm: laser-induced fluorescence analysis, chemical analysis, and doping studies,” *Optical Society of America B*, 1986, **vol. 3**, 5, pp. 785–791.
- Srinivasan, R., Hall, R., Loehle, W., Wilson, W., and Allbee, D., “Chemical transformations of the polyimide Kapton brought about by ultraviolet laser radiation,” *Journal of Applied Physics*, 1995, **vol. 78**, 8, pp. 4881–4887.
- Srinivasan, R. and Mayne-Banton, V., “Self-developing photoetching of poly (ethylene terephthalate) films by far-ultraviolet excimer laser radiation,” *Applied Physics Letters*, 1982, **vol. 41**, 6, pp. 576–578.
- Sutcliffe, E. and Srinivasan, R., “Dynamics of UV laser ablation of organic polymer surfaces,” *Journal of Applied Physics*, 1986, **vol. 60**, 9, pp. 3315–3322.
- Tien, C.-H., Chien, Y.-E., Chiu, Y., and Shieh, H.-P. D., “Microlens array fabricated by excimer laser micromachining with gray-tone photolithography,” *Japanese Journal of Applied Physics*, 2003, **vol. 42**, 3R, p. 1280.
- Tokarev, V., Lopez, J., and Lazare, S., “Modelling of high-aspect ratio microdrilling of polymers with UV laser ablation,” *Applied Surface Science*, 2000, **vol. 168**, 1, pp. 75–78.
- Tokunaga, Y., Kobayashi, H., Ishimaru, Y., Aizawa, K., and Hirama, J., “Thermal diffusivities of commercial transparent polymer films measured using laser induced thermal wave,” *Acoust. Sci. & Tech*, 2010, **vol. 31**, pp. 288–292.
- Toth, Z., Hopp, B., Kantor, Z., Ignacz, F., Szörényi, T., and Bor, Z., “Dynamics of excimer

- laser ablation of thin tungsten films monitored by ultrafast photography,” *Applied Physics A*, 1995, **vol. 60**, 5, pp. 431–436.
- Tsutsumi, N. and Kiyotsukuri, T., “Measurement of thermal diffusivity for polymer film by flash radiometry,” *Applied Physics Letters*, 1988, **vol. 52**, 6, pp. 442–444.
- Veiko, V. P., Kaidanov, A. I., Kovachki, H. A., and Shakhno, E. A., “Local laser-induced deposition of thin films,” *Proc. SPIE 1723, LAMILADIS '91 Intl Workshop: Laser Microtechnology and Laser Diagnostics of Surfaces*, 1992, **vol. 1723**, pp. 63–69.
- Voisey, K., Kudesia, S., Rodden, W., Hand, D., Jones, J., and Clyne, T., “Melt ejection during laser drilling of metals,” *Materials Science and Engineering: A*, 2003, **vol. 356**, 1, pp. 414–424.
- Von Allmen, M., “Laser drilling velocity in metals,” *Journal of Applied Physics*, 1976, **vol. 47**, 12, pp. 5460–5463.
- Von Allmen, M. and Blatter, A., “Laser-beam interactions with solid materials: Physical principles and applications, 2nd updated ed,” , 1995.
- Watts, C. M., Liu, X., and Padilla, W. J., “Metamaterial electromagnetic wave absorbers,” *Advanced Materials*, 2012, **vol. 24**, 23, pp. OP98–OP120.
- Weiner, J., “The physics of light transmission through subwavelength apertures and aperture arrays,” *Reports on Progress in Physics*, 2009, **vol. 72**, 6, p. 064401.
- Xu, X., “Phase explosion and its time lag in nanosecond laser ablation,” *Applied Surface Science*, 2002, **vol. 197**, pp. 61–66.
- Yao, Y., Chen, H., and Zhang, W., “Time scale effects in laser material removal: a review,” *The International Journal of Advanced Manufacturing Technology*, 2005, **vol. 26**, 5, pp. 598–608.

- Yeo, C., Tam, S., Jana, S., and Lau, M. W., "A technical review of the laser drilling of aerospace materials," *Journal of Materials Processing Technology*, 1994, **vol. 42**, 1, pp. 15–49.
- Yilbas, B., "Study of affecting parameters in laser hole drilling of sheet metals," *Journal of Engineering Materials and Technology*, 1987, **vol. 109**, pp. 282–287.
- Yilbas, B. and Yilbas, Z., "Parameters affecting hole geometry in laser drilling of Nimonic 75," in *SPIE*, vol. 744, pp. 87–91.
- Zaleckas, V. J. and Koo, J. C., "Thin film machining by laser induced explosion," *Applied Physics Letters*, 1977, **vol. 31**, pp. 615–617.
- Zhang, W., Yao, Y. L., and Chen, K., "Modelling and analysis of UV laser micromachining of copper," *The International Journal of Advanced Manufacturing Technology*, 2001, **vol. 18**, 5, pp. 323–331.
- Zhigilei, L. V., Lin, Z., and Ivanov, D. S., "Atomistic modeling of short pulse laser ablation of metals: connections between melting, spallation, and phase explosion," *The Journal of Physical Chemistry C*, 2009, **vol. 113**, 27, pp. 11892–11906.
- Zimmer, K., Braun, A., and Bigl, F., "Combination of different processing methods for the fabrication of 3D polymer structures by excimer laser machining," *Applied Surface Science*, 2000, **vol. 154**, pp. 601–604.

Appendices

Appendix I Heat capacities of aluminum and chromium

The heat capacity of aluminum [Chase Jr (13 Jul 2014)] is taken as

$$f(T) = \left[28.0892 - 5.414849 \left(\frac{T}{1000} \right) + 8.560423 \left(\frac{T}{1000} \right)^2 + 3.42737 \left(\frac{T}{1000} \right)^3 - \frac{0.277375}{(T/1000)^2} \right] \cdot \frac{1000}{26.9815} J/(kgK)$$

for $298.15K \leq T \leq 933.5K$, and

$$f(T) = 1086 J/(kgK)$$

for $933.5K < T < 2792K$

The heat capacity of chromium [Chase Jr (13 Jul 2014)] is taken as

$$g(T) = \left[7.489737 + 71.50498 \left(\frac{T}{1000} \right) - 91.67562 \left(\frac{T}{1000} \right)^2 + 46.0445 \left(\frac{T}{1000} \right)^3 + \frac{0.138157}{(T/1000)^2} \right] \cdot \frac{1000}{51.9961} J/(kgK)$$

for $298.15K \leq T \leq 600K$, and

$$g(T) = \left[18.46508 + 5.477986 \left(\frac{T}{1000} \right) + 7.904329 \left(\frac{T}{1000} \right)^2 - 1.147848 \left(\frac{T}{1000} \right)^3 + \frac{1.265791}{(T/1000)^2} \right] \cdot \frac{1000}{51.9961} J/(kgK)$$

for $600K < T \leq 2130K$, and

$$g(T) = 756.4 J/(kgK)$$

for $2130K < T < 2952K$

Appendix II Details of fitted models

The equations fitted to model the edge roughness and channel widths of channels are mentioned below. The equations are presented in the coded form, where A , B and C denote the input parameters *fluence*, *spot overlap* and *pitch*, respectively.

Aluminum

Roughness :

$$5.1 + 18.6A - 1.7B + 3.6AB + 9.7A^2 + 4.7B^2 + 1.5C^2 + 6.5AB^2 + 9.7A^2B^2 + 2.7B^3$$

Model p value = 1.8E-9; $R^2 = 0.99$; Adjusted $R^2 = 0.99$

$$\text{Width : } 108 + 78.9A + 20.6B - 32.8C + 23.9AB - 32AC - 13BC + 46.4A^2 + 11B^2 + 232.2C^2 - 10.3ABC$$

Model p value = 4.5E-11; $R^2 = 0.99$; Adjusted $R^2 = 0.99$

Aluminum with PVA coating

$$\text{Roughness : } 1.5 + 0.5A + 0.1B + 0.1AB - 0.1BC + 0.3A^2 + 0.2B^2 - 0.1A^2C - 0.1AB^2$$

Model p value = 6.2E-9; $R^2 = 0.99$; Adjusted $R^2 = 0.98$

$$\text{Width : } 123.8 + 3.8A + 0.4C - 0.6AB + 0.9BC + 0.5B^2 - 2.8A^2B + 0.7ABC$$

Model p value = 7.2E-8; $R^2 = 0.98$; Adjusted $R^2 = 0.97$

Chromium

$$\text{Roughness : } 2.5 + 0.6A + 0.1B - 0.94B^2 + 0.1C^2 + 0.4AB^2$$

Model p value = 5.9E-9; $R^2 = 0.97$; Adjusted $R^2 = 0.96$

$$\text{Width : } 131.2 + 11A - 1.6C - 0.9BC - 6B^2 + 8.1C^2 - 1A^2B + 7.1AB^2$$

Model p value = 3.0E-13 ; $R^2 = 0.99$; Adjusted $R^2 = 0.99$

Chromium with PVA coating

Roughness : $1.7 + 0.2A - 0.1AB - 0.1A^2 - 0.2A^2B$

Model p value = $7.1E-4$; $R^2 = 0.8$; Adjusted $R^2 = 0.73$

Width : $116.3 + 3A + 1.7B^2$

Model p value = $1.9E-2$; $R^2 = 0.45$; Adjusted $R^2 = 0.37$



Appendix III : Roughness and width measurements of a channel

Before analyzing an image for measurement of edge roughness and channel width, manually crop the image so that an image contains only one channel. The values of roughness and width obtained from the code are in pixels. To convert the pixels to micrometers, use the scale as per the image acquisition software. For images taken at 10 \times and 50 \times , we multiply the values in pixels with 2 and 0.4, respectively, to get the values in micrometers.

`clear all; clc;` *Clear previous results and close all previously opened files*

`I = imread('filename.jpg');` *Import image*

`J = rgb2gray(I);` *Convert RGB image or colormap to grayscale*

Decide pixel intensity thresholds for the left and the right edges

`level_a=0.7;` *left edge threshold*

`level_b=0.6;` *right edge threshold*

Decide upper and lower limits of rows and columns

`startrow=30;` *row lower limit*

`z=600;` *row upper limit*

`x1=1;` *column left limit*

`y1=80;` *column top limit*

`x2=80;` *column right limit*

`y2=160;` *column bottom limit*

For the left edge

`level=graythresh(I);`

`BWa = im2bw(I,level_a);` *Convert grayscale image to binary for the left edge*

Detect the entire channel

```
[BWa2 threshold] = edge(BWa,'canny');
```

```
[BWa3 threshold] = edge(BWa,'canny',threshold*0.25);
```

Dilate the Image

```
se90 = strel('line',5,90);
```

```
se0 = strel('line', 4, 0);
```

```
BWasdil = imdilate(BWa3,[se90 se0]);
```

```
BWadfill = imfill(BWasdil, 'holes'); Fill interior gaps
```

```
BWanobord = imclearborder(BWadfill, 4); Remove connected objects on the border
```

Smoothen the object

```
seD = strel('diamond',1);
```

```
BWafinal = imerode(BWanobord,seD);
```

```
BWafinal = imerode(BWafinal,seD);
```

Create a boundary around the channel

```
BWaoutline = bwperim(BWafinal);
```

```
Segout1 = I;
```

```
Segout1(BWaoutline) = 255;
```

```
figure, imshow(Segout1),
```

```
title('outlined original image a');
```

For the right edge

```
level=graythresh(I); Convert grayscale image to binary for the right edge
```

```
BWb = im2bw(I,level_b);
```

```

[BWb2 threshold] = edge(BWb,'canny');    Detect the entire channel

[BWb3 threshold] = edge(BWb,'canny',threshold*0.25);

se90 = strel('line',5,90);    Dilate the Image

se0 = strel('line', 4, 0);

BWbsdil = imdilate(BWb3,[se90 se0]);

BWbdfill = imfill(BWbsdil, 'holes');    Fill interior gaps

BWbnobord = imclearborder(BWbdfill, 4);    Remove connected objects on the border

seD = strel('diamond',1);    Smoothen the object

BWbfinal = imerode(BWbnobord,seD);

BWbfinal = imerode(BWbfinal,seD);

BWboutline = bwperim(BWbfinal);    Create a boundary around the channel

Segout2 = I;

Segout2(BWboutline) = 255;

figure, imshow(Segout2),

title('outlined original image b');

```

Store the edge data for which roughness has to be calculated

Store the left edge data

```

for row=startrow:z

for col=x1:y1

if(BWaoutline(row,col)==1)

store1(row-startrow+1)=col;

end

```

```
end
```

```
end
```

Fit a line to the left edge

```
X1=[1:1:row-startrow+1];
```

```
Y1=store1(X1);
```

```
p1=polyfit(X1,Y1,1);
```

Store the right edge data

```
for row=startrow:z
```

```
for col=x2:y2
```

```
if(BWboutline(row,col)==1)
```

```
store2(row-startrow+1)=col;
```

```
end
```

```
end
```

```
end
```

Fit a line to the right edge

```
X2=[1:1:row-startrow+1];
```

```
Y2=store2(X2);
```

```
p2=polyfit(X2,Y2,1);
```

Calculation of RMS roughness

Calculating distance of each data from the fitted line for left edge

```
for r=1:row-startrow+1
```

$$d1 = (p1(1) * r - store1(r) + p1(2)) / \text{sqrt}((p1(1))^2 + (1)^2);$$

$dsq1(r)=d1*d1;$ *square of distance*

end

$meansq1=mean(dsq1);$ *mean of square of distance for left edge*

$Roughness_left=sqrt(meansq1);$

Calculating distance of each data from the fitted line for right edge

for $r=1:row-startrow+1$

$d2 = (p2(1) * r - store2(r) + p2(2))/sqrt((p2(1))^2 + (1)^2);$

$dsq2(r)=d2*d2;$ *square of distance*

end

$meansq2=mean(dsq2);$ *mean of square of distance for right edge*

$Roughness_Right=sqrt(meansq2);$

Mean of RMS roughnesses of left and right edges

$Roughness = (Roughness_left+Roughness_Right)/2$ *Roughness in pixels*

Calculation of channel width

for $c1=x1:y2$

for $row=startrow:z$

$d = sqrt((store2(row - startrow + 1) - store1(row - startrow + 1))^2);$

end

end

$Width = mean(d);$ *Channel width in pixels*

Appendix IV : Drawings of the components of the mask indexer

Mask holder

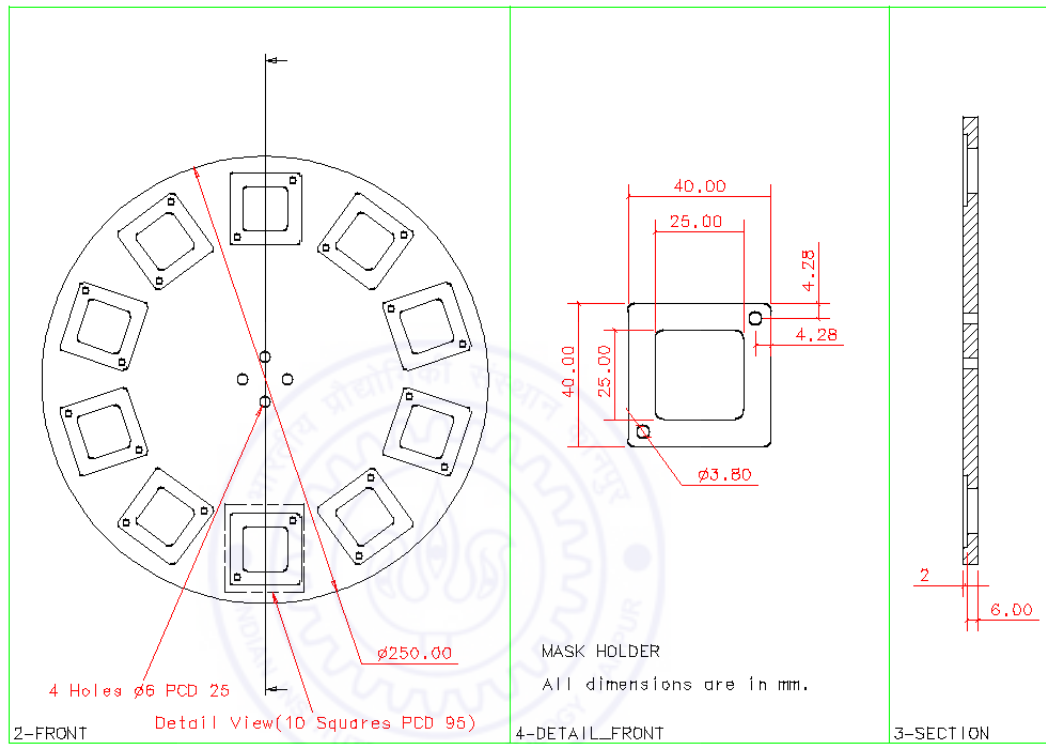


Figure 7.1: The mask holder with slots to mount upto 10 masks

Mask plates

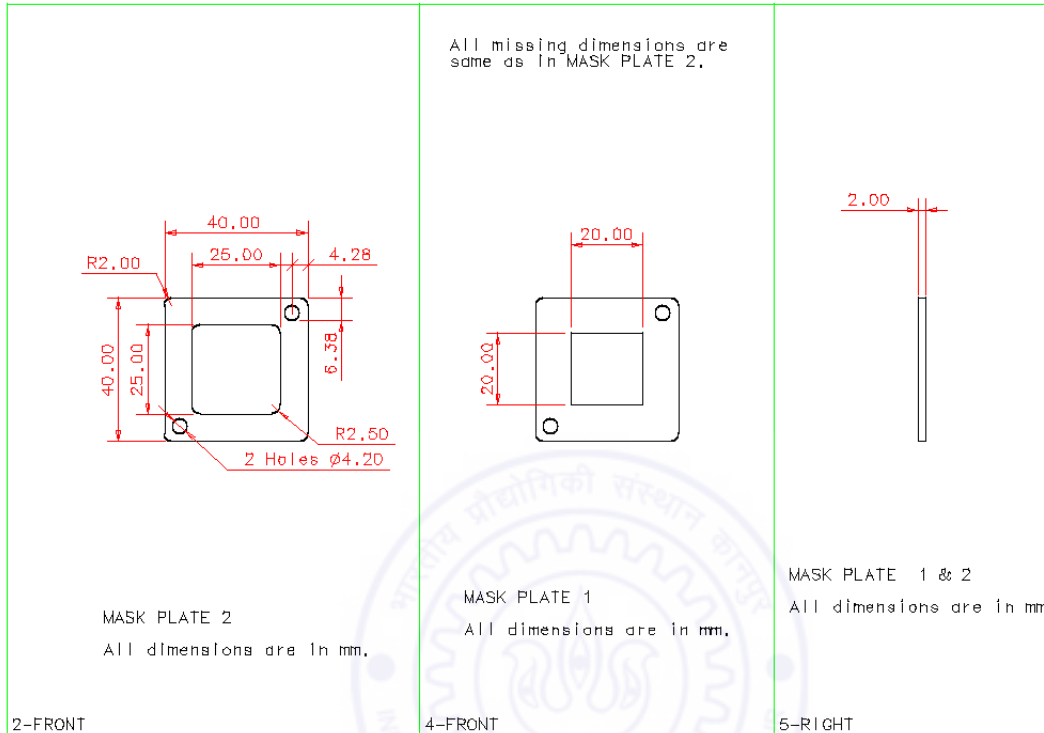


Figure 7.2: The mask plates, ten in number, that hold the masks in the slots.

Supports for the driving motor

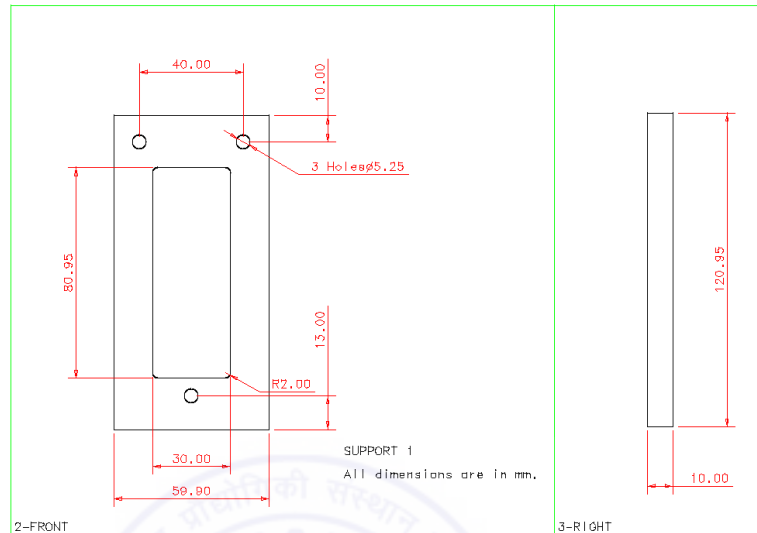


Figure 7.3: The bottom support on which the motor rests

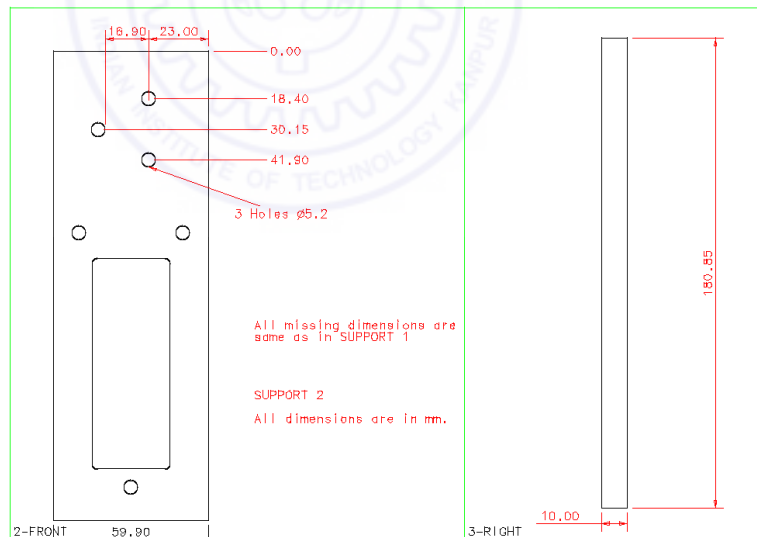


Figure 7.4: The back support for the motor

Base plate

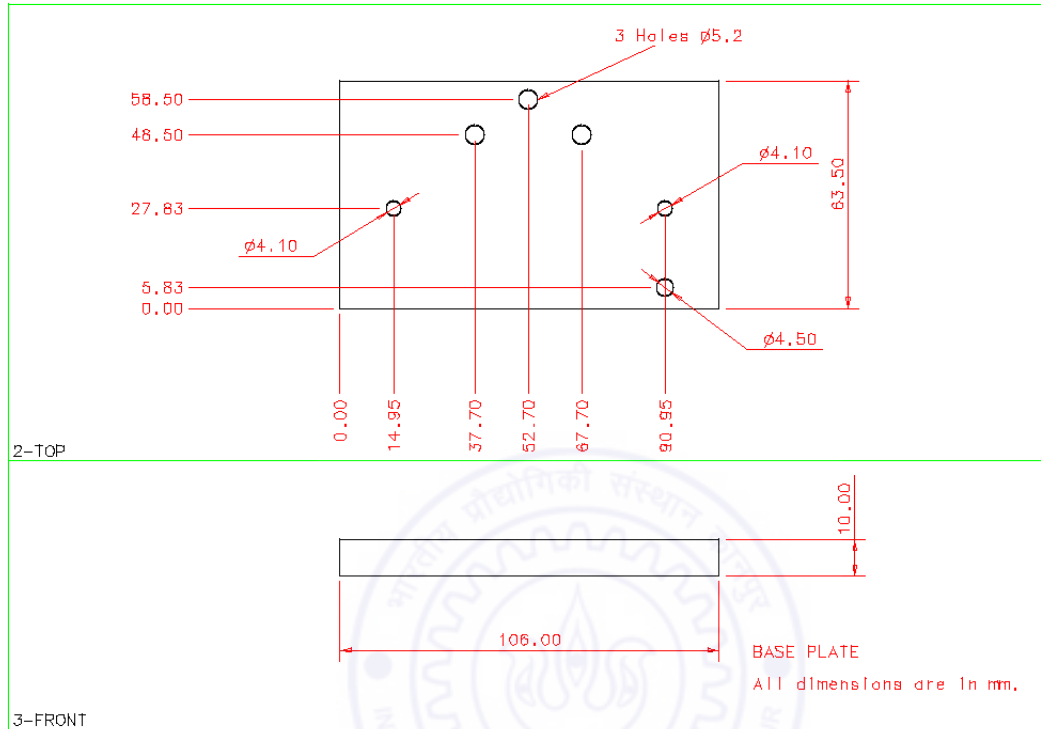


Figure 7.5: The base plate, on which the two supports are mounted. The base plate has holes that align with the locator pins on the laser machine.

Journal publications

- Akhtar, S.N., Sharma, S., Dayal, G., Ramakrishna, S. A., and Ramkumar, J., “Micro-feature edge quality enhancement in excimer laser micromachining of metal films by coating with a sacrificial polymer layer,” *IOP Journal of Micromechanics and Micro-engineering*, 2015, **vol. 25**, 6, pp. 065001-065012.
- Balani, K., Kumar, D., Akhtar, S. N., Patel, A. K., and Ramkumar, J., “Tribological performance of laser peened Ti-6Al-4V,” *Wear*, 2015, in press.
- Akhtar, S. N., Choudhary, H., Ramakrishna, S. A., and Ramkumar, J., “Simulation and Experiments on Excimer Laser Micromachining of Metal and Polymer,” *SPIE Journal of Micro/Nanolithography, MEMS, and MOEMS (JM3)*, 2014, **vol. 13**, 1.
- Singh, G. D., Akhtar, S. N., Ramakrishna, S. A., and Ramkumar, J., “Excimer Laser Micro-machining Using Binary Mask Projection for Large Area Patterning With Single Micrometer Features,” *ASME Journal of Micro and Nano-Manufacturing*, 2013, **vol. 1**,
- Kumar, A., Gupta, A., Kant, R., Akhtar, S. N., Tiwari, N., Ramkumar, J., and Bhattacharya, S., “Optimization of laser machining process for the preparation of photo masks and its application to micro-systems fabrication,” *SPIE Journal of Micro Nanolithography, MEMS, and MOEMS (JM3)*, 2013, **vol. 12**, 4.

Conference publications

- Akhtar, S. N., Sharma, S., and Ramkumar, J., “Fabrication of micro lens array by excimer laser micromachining,” *Proceedings of the 5th International and 26th National All India Manufacturing, Technology, Design and Research Conference (AIMTDR)*, 2014, Guwahati, India.
- Akhtar, S. N., Ramakrishna, S. A., and Ramkumar, J., “Microfeature Edge Quality Optimization in Excimer Laser Ablation of Metallic Film,” *2013 ASME International Mechanical Engineering Congress and Exposition (IMECE)*, 2013, San Diego, California.
- Akhtar, S. N., Ramakrishna, S. A., and Ramkumar, J., “Excimer Laser Micromachining on Polymers under Different Atmospheres and at Different Length Scales,” *8th International Conference on MicroManufacturing (ICOMM)*, 2013, Victoria, Canada.
- Akhtar, S. N., Ramakrishna, S. A., and Ramkumar, J., 2012, “Excimer Laser Experiments and Simulation on Various Materials,” poster presented in the *Asian Academic Seminar*, jointly organized by Department of Science and Technology, Government of India and Japanese Society for Promotion of Science, at Indian Institute of Technology Bombay, India.
- Mahanty, S., Gouthama, and Akhtar, S. N., “Surface modification of Titanium alloy upon irradiation with UV laser”, poster presented in the *49th National Metallurgists Day, Annual Technical Meeting of The Indian Institute of Metals*, 2011, Hyderabad, India.

Book chapters

- Akhtar, S. N., Sharma, S., and Ramkumar, J., Ch. “Fabrication of micro lens array by excimer laser micromachining,” in ‘Selected papers of 5th International and 26th National All India Manufacturing, Technology, Design and Research Conference’ in ‘*Laser Based Manufacturing,*’ Eds. S. N. Joshi, U. S. Dixit, 2015, Springer (in press).



